

通気率における測定条件の影響および通気率試験方法の耐火物評価への応用

朝倉秀夫, 馬場直樹, 前田朋之, 山口明良

岡山セラミックス技術振興財団 〒705-0021 岡山県備前市西片上1406-18

Influence of Measurement Conditions in Gas Permeability and Application of This Test Method to Refractory Evaluation

Hideo Asakura, Naoki Baba, Tomoyuki Maeda and Akira Yamaguchi

Okayama Ceramics Research Foundation

1406-18 Nishikatakami, Bizen-shi, Okayama 705-0021, Japan

Abstract : We have been carrying out investigation for some problems concerning gas permeability and application of their clarification technologies to refractories by a new gas permeability measuring apparatus. 1) It is thought that the gas stream in refractories flows not as a laminar flow but as a calm turbulent flow, and gas density is thought to influence the permeability measurements under high pressure conditions. 2) Two types of samples were taken from the MgO-C brick. One type was taken from the side to which pressure was applied during manufacturing and other type was taken from the side perpendicular to the direction to which pressure was applied. There was a clear difference in the permeability which was caused by orientation of the graphite between the two types of samples used. 3) Permeability of refractories was found to increase with pore diameter. However, pores generated by the heating and dehydrating of castable are small with diameters of 10nm - 100nm.

Key words : Permeability, Castable, MgO-C brick, Turbulent flow, Laminar flow

要 旨 : 新しい通気率試験装置を用いて通気率に関する幾つかの課題の探求とそれら解明技術を耐火物の解析に適用した。1) 耐火物中のガス流は、層流でなく穏やかな乱流として流れており、また、高圧条件での通気率測定値はガス密度の影響を受けていると考えられる。2) MgO-Cれんがから2つのタイプの試料を採取した。ひとつは製造時のプレス成形方向側から、他方はプレス成形方向と垂直側からである。その二つ方向から採取された試料間には、黒鉛の配向性に起因する明らかな差があった。3) 耐火物の通気率は、気孔の大きいものほど高い。しかし、キャストブルの加熱・脱水によって生成される気孔は、10nm~100nmと小さい。

キーワード : 通気率, キャスタブル, MgO-Cれんが, 乱流, 層流

1 緒言

本誌における通気率に関する報告は、本誌が“耐火物工業”として刊行されていた約60年前¹⁾に遡ることができるが、その後のこれら報告の多くは、“例えば、キャストブルの耐爆裂性”を通気率値から評価するといった通気率の物性値としての利用に関するものであった。したがって、この機会に今まで余り実施されていなかった通気率測定値の変動要因の検証、通気率の耐火物評価への適用可能性の追及など測定技術サイドから見た通気率の本質・意義などを検討することも大切と考えられる。

著者らはこのような観点に立ち通気率を迅速・簡易に測れる装置を開発し^{2,3)}、今回それら装置を用いて通気率測定値の変動要因検証のために測定精度、測定圧、試験片厚さを取り上げ、通気率測定値の統計的評価、試験片中を流れる流体の挙動と適正通気率測定条件を検討した。また、

これら通気率測定技術を実際の耐火物に適用することによって、焼成れんがおよびマグネシア・カーボン（以降MgO-C）れんがの試料間差と配向性の問題、キャストブルの混練品の再現性、水分量と通気率、加熱と気孔変化の解析を試みた。

2 実験方法

2・1 装置および操作方法

窒素ガス流量 $0.1 \sim 5000 \text{ ml} \cdot \text{min}^{-1}$ 、差圧 $1 \sim 100 \text{ kPa}$ に対応できるコンピュータ制御による自動通気率測定装置^{2,3)}を用いた。操作は、次のように行った。図1の試験片ホルダ①内に試験片②を挿入し、入口側ジグ③および出口側ジグ④によって試験片を挟んだ。通気率測定系とは別に設けたガス流路のガスコック⑤を開け、 200 kPa の窒素ガス⑥

平成23年5月11日受付, 平成23年9月26日受理

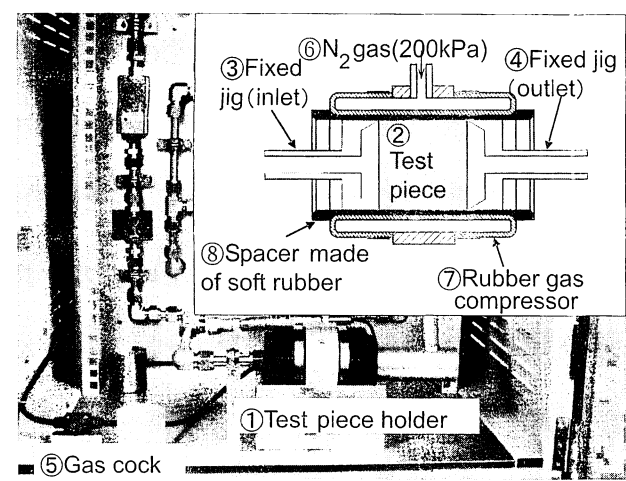


Fig. 1 Structure of test piece holder.

を流して試験片ホルダ内の加圧用ゴム⑦を膨らませ、そのガス圧力によって軟質ゴム製スペーサ⑧を強く加圧して試験片側面を拘束した。以下コンピュータ制御の下に試験片に窒素ガスを流してガス流量と差圧を自動的に読取り、通気率を算出した後、プリンタに出力した。試験片は、ガスコックを閉じ、入口側および出口側両ジグを取外して脱着した。

2・2 試料および試験片の作成方法

表1に本稿で用いた実験試料を示す。れんがが試料の場合、内寸法φ50mmのダイヤモンドビットで切り抜き、円柱の上下面を平面研削盤で研削・研磨してφ50×^H50mmに仕上げた後、乾燥・冷却して試験片とした。キャストブルの場合、φ50×^H50mmの鋳型で振動鋳込みし、20℃で24h養生後、110℃で24h乾燥して試験片とした。試験片寸法は、ノギスを用いて0.1mmの桁まで正確に測った。3・2節および3・3節に用いる高アルミナれんがA、MgO-CれんがBおよびキャストブルDは、上述の基本作法の下で次のように作製した。

- (1) 高アルミナれんがAおよびMgO-CれんがB：各々無作為に5試料を採取し、れんがに1～5の番号を付し、れんが毎に^L230mm×^d114mmの面の長さ方向を3分割し、幅方向を2分割し、各2分割片の一方を軸方向

測定グループ、他方を直角方向測定グループとした（各グループ共に、5試料×3分割片/試料=15分割片）。軸方向測定グループからは、れんが成形時の加圧軸と同一方向の通気率を測定するための試験片（φ50mm面が成形時の成型圧面に相当）を採取した。同様に、直角方向測定グループからは、成形時の加圧軸と直角の方向の通気率を測定するための試験片を採取した。両グループ共に個々の試験片には符号を付け、個体が識別できるようにした。MgO-CれんがB（ベークینگ品）については、3・1・3項の検討結果を基に試験片厚みを20mmとし、室温の通気率測定後の試験片は、更に黒鉛を詰めたアルミナ製さやに入れ1000℃で3h焼成して焼成後試験片とした。

- (2) キャスタブルD：次の3種のグループの試験片を作製した。

- 1) キャスタブルD配合品（1kg）を5個準備し、各配合品に6.75%の水分を加えて万能混合器で3分間混練し、各々3個の試験片（φ50×^H50mm）を作成し、試験片に識別番号を付した。
- 2) キャスタブルD配合品への水添加量を6.75%を中心に0.25%刻みで増減させた各3個の試験片を作り、20℃で24h養生後、一つを20℃-24h養生品とし、更に110℃-24h乾燥品および1000℃-3h焼成品を作った。
- 3) 上述1)に準じて鋳込み、2)に準じて20℃、110℃、300℃、500℃、800℃、1000℃および1500℃で熱処理した。

2・3 通気率測定値の表し方

通気率は、特別に述べない限り、3種の異なる圧力で測定して得た3つの測定値の平均値によって表した。通気率計算式を式(1)⁴⁾に示す。

$$\mu = c \times \eta \times \frac{h}{3.14 \left(\frac{d}{2}\right)^2} \times \frac{1}{p_1} \times \frac{2(p_0 + p_1)}{2p_0 + p_1} \times q_v \tag{1}$$

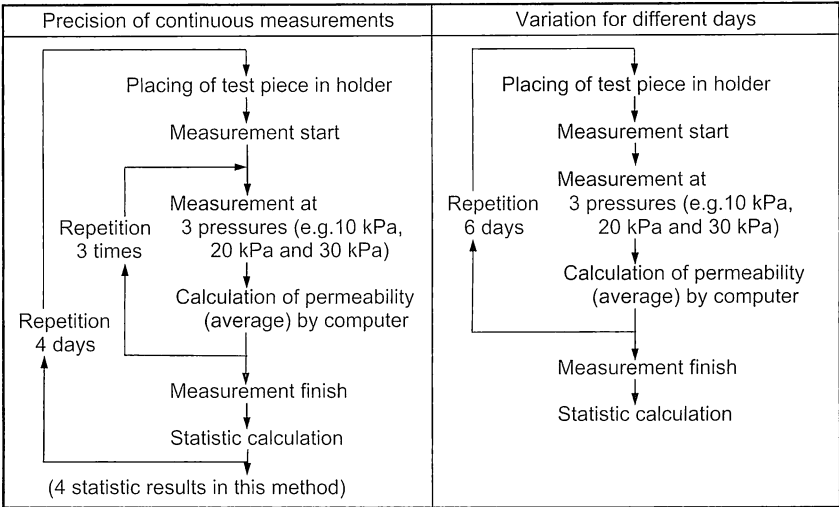
ここに、μ：測定試料の通気率（m²）
c：試験片寸法、圧力、ガス流量の計算単位へ

Table 1 Test samples used in this report

		F-C brick	M-Spi brick	C brick	MgO brick	Al ₂ O ₃ brick		MgO-C brick		Castable			
						A	B	A	B	A	B	C	D
Chemical composition /mass%	LOI	—	—	—	—	—	—	8.30	12.8	1.11	1.56	1.70	1.28
	SiO ₂	46.6	—	—	2.30	18.3	0.13	1.01	4.28	30.1	0.28	4.89	0.85
	Al ₂ O ₃	46.5	70.2	—	—	76.3	99.5	4.10	5.42	64.7	96.2	91.2	89.2
	CaO	—	—	—	—	—	—	—	—	1.11	1.32	0.91	1.39
	MgO	—	28.8	—	95.8	—	—	84.7	77.4	—	—	—	6.91
	T.C	—	—	99.9	—	—	—	9.64	14.5	—	—	—	—

F-C brick: Fireclay brick, M-Spi brick: Magnesia-Spinel brick, C brick: Carbon brick, MgO brick: Magnesia brick, Al₂O₃ brick: High alumina brick, MgO-C brick: Magnesia-carbon brick

Table 2 Measurement schemes of repeatability



の補正係数 (mm/m·kPa/Pa·min/s·m³/cm³)
c=1/60×10⁻⁶を用いる。

- η : 測定ガスの粘度 (Pa·s)
- h : 試験片の高さ (mm)
- d : 試験片の直径 (mm)
- p_0 : 大気圧 (kPa)
- p_1 : ガス圧力差計の読み (kPa)
- q_V : ガス流量 (cm³·min⁻¹)

ところで、式(1)で得られる通気率の単位平方メートル (m²) は、感覚的に少し判り難い。そこで本報では、一つの指標として“差圧10kPaの窒素ガス (25℃) が^φ50.0mm×^H50.0mmの試験片中を流れる時の流量 (ml·min⁻¹)”を“通気指数 (q_{index})”として提唱し、図の副尺などで示した。通気指数 1 ml·min⁻¹は、通気率 0.79×10^{-15} m²に相当する。

2・4 測定値の変動要因の検証実験方法

2・4・1 測定精度調査実験方法

高アルミナれんがA、スピネルれんがおよびキャストブルAを表2に示す方法で測定した。

2・4・2 差圧による通気率変化の調査実験方法

高アルミナれんがB、キャストブルB乾燥品、キャストブルB焼成品および黒鉛れんがの各試験片を試験片ホルダに入れ測定ガス圧 (差圧) を1～100kPaの範囲で段階的に変動させながら各差圧での通気率値を測定した。各差圧での繰返数は1回とした。黒鉛れんがは、既報⁵⁾と同じものを用いた。キャストブルB焼成品は、2・2節で作製した試験片を1500℃で2時間焼成して用いた。

2・4・3 試験片厚みの影響調査実験方法

粘土質れんが、マグネシアれんがおよびキャストブルCについて、先ず、標準形状^φ50×^H50mmの試験片の通気率

を測定した後、その試験片を3分割して25mm、12.5mm、8.5mmの厚みの試験片に加工して通気率を測定した。また、MgO-CれんがAでは、標準形状の試験片を測定後、研削して43mmの厚さで測定し、更に3分割して厚み18mm、12.5mm、8.5mmの試験片にして測定した。

3 結果と考察

3・1 通気率測定値の変動要因の検証

3・1・1 測定精度の検討

表3に2・4・1項によって得られた単純繰返精度の測定結果を示す。表3のRSD (相対標準偏差) は、通気率の高い高アルミナれんがAおよびスピネルれんがで各々0.3%および0.2%と低い。一方、通気率の低いキャストブルAでは1.8%と高い。この両れんがのRSD 0.3%および0.2%は、化学分析における主成分の分析精度にも匹敵する高精度である。一方、キャストブルAは、RSDが1.8%と大きいものの、 σ (標準偏差) で見ると 0.017×10^{-15} m²と小さく精密な精度を示しており、化学分析に見られる微量成分の分析精度に類似している。高アルミナれんがAの通気率 311.7×10^{-15} m²とキャストブルAの通気率 0.905×10^{-15} m²を通気指数で比較すると、前者が約392ml·min⁻¹であるのに対して後者は、約1.13ml·min⁻¹である。すなわち、キャ

Table 3 Test results for assessing of continuous measurements

	Al ₂ O ₃ A (S1-1)	Spinel	Castable A
Data collection days/d	4		
Average of permeability/×10 ⁻¹⁵ m ²	311.7	173.3	0.905
Average of σ of 4 d/×10 ⁻¹⁵ m ²	0.9	0.3	0.017
Average of RSD of 4 d/%	0.3	0.2	1.8

σ and RSD represent standard deviation and relative standard deviation respectively.

スタブルAは、流量計の計測精度が得難い微小流量域で測られているのに対して、高アルミナれんがAは、計測精度が得易い流量域で測られており、その差が表3のRSDに反映されたものと推察される。

一方、日々の測定では、測定毎に試験片が挿脱着され、また装置を構成する計器類も変動を起こしている。これらは表2の右欄に示す日間繰返精度で表される。表4にその実験結果を示す。表から日間繰返精度は、各試料共に表3の単純繰返精度の約4倍と大きい。すなわち、高アルミナれんがAの場合、RSD 1.4%、キャストブルAの場合、RSD 8.1%である。これを、統計上の95%信頼区間(平均値±1.96σ)で見ると、日を変えて通気率を測定した場合、高アルミナれんがAでは、95%の確率で $310.4 \pm 8.4 \times 10^{-15} \text{m}^2$ ($302.0 \sim 318.8 \times 10^{-15} \text{m}^2$)の間の結果が得られるのに対して、キャストブルAでは、 $0.957 \pm 0.153 \times 10^{-15} \text{m}^2$ ($0.804 \sim 1.110 \times 10^{-15} \text{m}^2$)の間の値となる。各々の測定値には一定の広がりを持った信頼区間が存在しており、測定結果を用いた解析では、この日間繰返精度を考慮した議論が必要と考えられる。

Table 4 Test results of variation for different days

	Al ₂ O ₃ A (A-1-1)	Spinel	Castable A
Data collection days/d	6		
Average of permeability /×10 ⁻¹⁵ m ²	310.4	174.1	0.957
σ/×10 ⁻¹⁵ m ²	4.2	1.5	0.078
RSD/%	1.4	0.8	8.1

3・1・2 差圧と流体の挙動の検討

既報⁵⁾で測定ガス圧(差圧)を2~100kPaの範囲で変動させると通気率値が測定ガス圧と共に高まる現象が見られた。しかし、本来通気率は、ダルシーの法則による層流の流れであり、式(1)で示されるように測定ガス圧に依存しない物理量と考えられる。何故このような現象が起こるかを究明するために、装置に低压側の測定精度を高める改造を行い、2・4・2項の実験をして得られた結果を図2に示す。但し、キャストブルB 110℃-24h乾燥品は、差圧10kPa未満で測定流量が装置の測定限界の0.1ml・min⁻¹以下と低かったため10kPa以上で得られた結果を示した。図中で横軸が差圧、縦軸左目盛が通気率、右目盛が通気指数である。4試料の通気率は、10⁻¹⁶~10⁻¹³m²に亘るもので、これを図2の縦軸右目盛りの通気指数でみると0.1~400 ml・min⁻¹となる。図を見て先ず気付くことは、キャストブルB乾燥品と高アルミナれんがBの間での通気率の差は、約4000倍もあり、いわゆる試験法としての分解能は非常に高いことが判る。しかし、個々の試料の通気率を差圧とからめて見ると幾つかの傾向が認められる。先ず、全試料を通じて差圧5~30kPaでは、差圧の影響が少なく、安定した値が得られている。一方、この安定区間を挟んで低压の1~4kPa域では、低压になる程高めの値となり、1kPaで差圧5~30kPaの最大20%程高い値を与えている。また、差圧40~100kPaになると、興味深いことに黒鉛れんがでは、5~30kPaの延長線のように差圧の影響を殆ど受けることなく一定の値を示しているのに対して、他の試料では、差圧値が高くなるにつれ測定値が高くなっている。

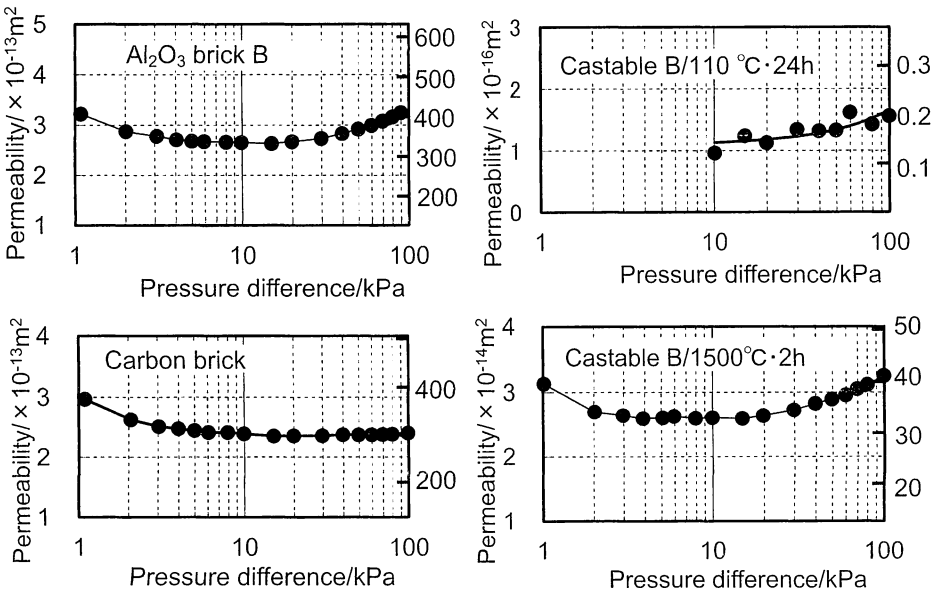


Fig. 2 Relation between measurement pressure and permeability for test samples. Right scale of vertical axis shows permeance index (ml・min⁻¹).

Table 5 Physical property value of test samples concerning pores including permeability values

Test item \ Test sample	Burned brick		Castable B	
	Al ₂ O ₃ B	Carbon	110°C/24h	1500°C/2h
Permeability/×10 ⁻¹⁵ m ²	265	244	0.1	26
Permeance index/ml・min ⁻¹	334	307	0.1	33
Apparent Porosity/%	16.8	18.7	14.0	18.1
(4V/A)/μm	5.9	0.037	0.041	1.7

(4V/a) represents average pore diameter.
Permeability figures in table are test sample values at 10 kPa.

そこで、差圧による通気率値の変動についての知見を見出すために試料中の気孔について調査した。表5に通気率も含めた試料相互の気孔に関する物理特性値を、また、図3に各々の試料の気孔径分布を示す。表5および図3から、通気率は、高アルミナれんがB>黒鉛れんが>キャストابلB焼成品>キャストابلB乾燥品の順に小さくなり、見掛気孔率は、黒鉛れんが>キャストابلB焼成品>高アルミナれんがB>キャストابلB乾燥品の順に小さくなり、平均気孔径は、高アルミナれんがB>キャストابلB焼成品>キャストابلB乾燥品>黒鉛れんがの順に小さくなっている。これら結果から、通気率は、気孔の量と言うよりも、気孔の径と深く関わっているように見受けられる。例えば、キャストابلB焼成品に比べて高アルミナれんがBは、見掛気孔率が1%低いにも関わらず、平均気孔径が3.5倍も大きい。すなわち、このことが高アルミナれんがBの通気率がキャストابلB焼成品に比べて約10倍も高くなっ

た理由と推察される。一方、黒鉛れんがは、キャストابلB乾燥品に比べ、見掛気孔率で4.7%高いとは言え、平均気孔径は寧ろ低い。この両者間には通気指数で300ml・min⁻¹と0.1ml・min⁻¹という非常に大きく差が見られる。そこで、黒鉛れんがとキャストابلB乾燥品の気孔の特徴を比較した。まず、黒鉛れんがでは、図3からその気孔径がφ10nm以下の微細気孔とφ10μm以上の大気孔に2分極する形で存在しており、その微細気孔は、図4のように多孔質の無数の孔として存在している。一方、キャストابلB乾燥品のプロファイルからは、比較的小さいφ20nm、φ300nmおよびφ2μmあたりにピークが存在するものの、黒鉛れんがのような大きな気孔が認められない。すなわち、黒鉛れんがは、キャストابلB乾燥品よりも平均気孔径が小さいにも関わらず、φ10μm以上の大きな気孔が存在することから、これら大気孔がガスの流れを担い通気率を高めていると結論される。なお、この黒鉛れんが中の多量の微細気孔は、他の試料に認められないものであり、黒鉛れんがの差圧40～100kPaにおける流体挙動に何らかの関わりがあるように推察される。

式(2)⁶⁾は、水収支研究に用いられるダルシーの法則の一般式である〔記号は式(1)に整合化させた。μは定数で通気率に相当する〕。

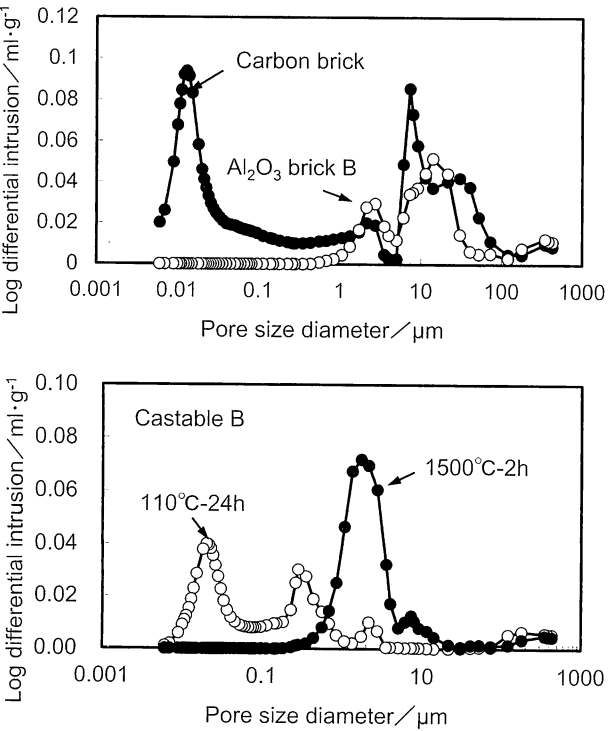


Fig. 3 Pore size distribution results of test samples.

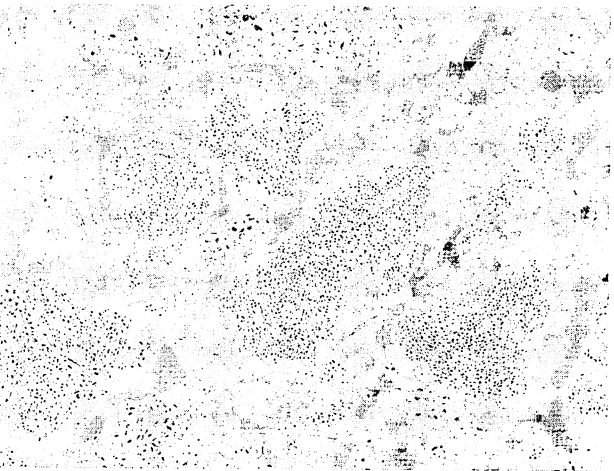


Fig. 4 Microstructure of carbon brick.

$$v = \frac{\mu D^2 \rho g \cdot I}{\eta} \tag{2}$$

ここに、 v ：流速 [式(1)の $V \cdot t^{-1}$ に相当)]

D ：帯水層骨格の粒径

ρ ：流体の密度

g ：重力加速度

η ：流体の粘性係数

I ：動水勾配

この式で注目されるのは、流体の粘性係数（粘度）と流体の密度に関わる項が含まれていることである。式(1)では、この内流体の粘度 η については与えられているが、圧力による粘度変化が考慮されていない。そこで、文献⁷⁾によって300K (=27℃)における窒素ガスの粘度を調べたところ、絶対圧100kPaで17.91μPa・s、200kPaで17.92μPa・sであり、窒素ガスの粘度は、圧力によって殆ど変化しないことが判った。気体の粘性は、圧力によって殆ど変化しないため、耐火物の通気率測定では考慮しなくても良いといえる。一方、流体の密度は、明らかに圧力によって左右される。例えば、圧力が2倍になれば密度も2倍になるはずである。試験片を通過する入側圧が測定圧であり、出側圧が大気圧となるので試験片内に圧力勾配およびそれに伴う密度勾配が生じるはずである。密度勾配は、ガスの流れが定常状態にあれば一次関数で表されると想定される。ここで、密度勾配に関する理論は別として、流体の密度が通気率測定値に影響するのであれば、多くの試料において高圧になるほど通気率が高くなる理由の説明にはなる。しかし、図2に見られる測定値が1～4kPaで高めの値を示した後、5～30kPaに安定区間となり、続く40～100kPaにおいて黒鉛れんがを除く試料において急激な増加が起こる変化は、このガス密度の問題だけでは説明がつかない。もし、試験片内でガスの密度が圧力の一次関数として変化するのであれば、5～30kPaの安定区間があることも、100kPaで通気率が1.5倍になっていないことも説明できない。何よりも、黒鉛れんがが100kPaまで安定した値を示すことが説明できない。

図5に施条を施した塗装ガンノズルを試験片形状のステンレス中に埋め込んで差圧と通気率の関係を測定した結果を示す。図5から強力な乱流では、差圧と共に急激に通気率測定値が低下し、差圧2kPaから70kPa間で実に10分の1にまで低下している。今まで、我々^{8,9)}は、粒や粉で構成される耐火物中の気体の流れを、ダルシーの法則の前提となる低レーノルズ数領域¹⁰⁾ (=層流)の流れと仮定して考えてきた。しかし、耐火物内の大きな気孔や小さな気孔が入り混じったガス流路を流れる気体の流れが、理論通りの層流と考えること自体に問題があったのではないか。

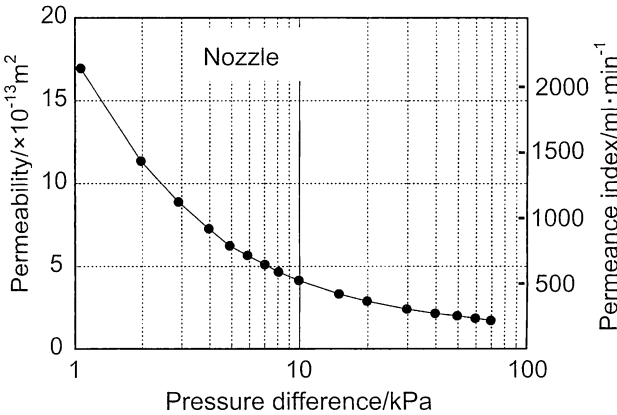


Fig. 5 Relation between measurement pressure and permeability of gun-nozzle.

例えば、試験片中を流れるガスの流れは、層流と乱流の混成流れ、または、弱い乱流との考え方を追加するとどうであろうか。図2の差圧1～4kPa域の差圧－通気率曲線は、図5の乱流の流れに符号しているように見受けられる。

以上を整理すると図2の差圧－通気率曲線は、差圧1～4kPa域では、ガス圧が低いためガス密度の影響が殆どなく、乱流の影響によって1kPaから4kPaに向けて測定値が低下し、差圧5～30kPa域では、ガス圧が高まり密度上昇が測定値の高値化を起こす力として働く一方で乱流による測定値の低下要因もあって、相互の要因が均衡して安定した測定値を示し、最後の差圧40～100kPa域では、乱流の影響による測定値の低下要因よりもガス密度上昇による高値化要因が勝り、ガス圧上昇と共に測定値が上昇したと考えられる。ただ、黒鉛れんがでは、差圧40～100kPa域においても試料中を流れるガスが多量の微細気孔によって流れを乱され、ガス密度上昇による測定値上昇と乱流による測定値低下の均衡が続いているのではないかと推察される。

以上の結果から、ダルシーの法則が地下水の層流の流れを前提に導き出した透水係数であるのに対し、耐火物の通気率は、気体である流体がダルシーの法則による理論通りの挙動を示さず、差圧－通気率曲線上において通気率測定値が、乱流、流体の密度および試験片中の気孔状態などの影響を受け微妙な変化を示したと結論される。なお、この節での課題は、差圧による微妙な通気率の変化を流体の挙動から解明することが目的であった。実用上の耐火物の通気率は、1～100kPa間の何れで測定したとしても、その変動幅は最大でも20%程度であり、試料間でオーダの差さえ生じる通気率の特性を考慮すれば、余り意識過剰になる必要はないように思われる。また、実際の通気率測定では、図2に示されるように安定した通気率値が得られる差圧5～30kPa域の、例えば、10kPa、20kPaおよび30kPaの

朝倉秀夫 他 通気率における測定条件の影響および通気率試験方法の耐火物評価への応用

3 点の差圧で得られた通気率の平均値を用いるようにすれば測定値の信頼性と研究課題の解析精度も高まるものと考えられる。

3・1・3 試験片厚みの検討

式(1)は、 $\phi 50 \times H 50\text{mm}$ の標準形状の試験片を前提に設定された規格としてのものである。しかし、実際の測定では、規定の試験片を得難いことも多い。そこで、通気率と試験片厚みの関係を検証するために、2・4・3項の実験を行った。図6にこのようにして得られた測定結果を示す。図から各厚みの測定値を見ると、試験片の厚みが50mm~20mm位までは略安定した値を示し、各測定値を結んだ線が略一直線となっている。しかし、厚みが12.5mmおよび8.5mmと更に薄くなると、各測定値を結んだ線が上下に分散するようになっている。しかし、この分散は、“分散”と表現したように試験片の厚みとの間に一定の相関が認められない。すなわち、試験片が標準形状の4分の1(12.5mm)、6分の1(8.5mm)と薄くなれば、耐火物が不均質体であるが故に、それら試験片も元の標準形状の試験片を代表する確率も4分の1、6分の1と厚みと共に低下して分散として現れたものと推察される。一方、MgO-CれんがAおよびキャストブルCの通気率は、表4のキャストブルAと略同程度の $1 \times 10^{-15}\text{m}^2$ (通気指数で $1\text{ml} \cdot \text{min}^{-1}$)であるので、繰返精度もRSD 8%前後と高く、測定値に5%有意水準で $\pm 15 \sim 20\%$ ($\pm 0.15 \sim 0.20 \times 10^{-15}\text{m}^2$)の測定誤差が含まれているといえる。言い換えれば、図6においてMgO-CれんがAおよびキャストブルCの通気率の分散は、単に耐火物の不均質性によるだけでなく測定精度も関与していると見るべきであろう。低通気率試料においては、例えば、試験片の厚みを20mmにすれば、同一差圧でも標準形状よりもガス流量を2.5倍に高めることができ、標準形状で差圧を2.5倍にしたと同等の効果が期待できる。前節で見られた高差圧での問題点を考慮すれば、低通気率試料

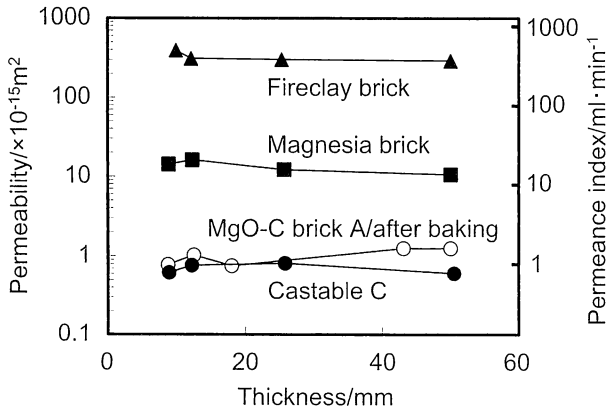


Fig. 6 Relation between test piece thickness and permeability.

での薄肉化は、かえって良い効果を示すのものとも考えられる。そればかりでなく、薄肉化は、超低通気率試料や試験片厚みが得難い試料など通気率の測定が困難だった試料の通気率測定を可能とする効果も期待できる。以上の結果から、試験片厚みを極端に薄くしない限り、式(1)の関係式は満足され、その厚みも耐火物の不均質性が問題とならない範囲内で薄肉化(例えば、15mm程度)が可能と結論される。

3・2 通気率の耐火物解析への適用

3・2・1 焼成れんがの試料間差と配向性の検討

同じ試料間の個体差の識別および成形時の加圧による粒の配向性の残留の有無の解析に通気率の持つ高い分解能が利用できないかを検討した。図7に高アルミナれんがAの軸方向測定グループおよび直角方向測定グループ各15試験片[2・2節の(1)]の通気率測定結果(差圧10kPa、20kPaおよび30kPaの平均値)を図示する。図中、縦軸は通気率および通気指数、横軸はれんが番号、また、符号“—”、“●”および図中に長く引かれた“—”は、各々、各試験片の測定値、同一れんがの3試験片測定値の平均値および15試験片測定値の平均値を表す。図から同一れんがの3試験片間に、大きな差があるもの、れんが2のように殆ど差がないものなど、個々の測定値を容易に見分けることができ、図からだけでも同一れんがの採取位置によって通気率に大きな差があるもの差の少ないものがあることが判る。なお、これら通気率の差は、れんが組織の不均質性を反映したものと推察される。表6にこれら測定結果を統計処理して求めた同一れんが内(群内)と異種れんが間(群間)の統計値を示す。ここで表4の高アルミナれんがAは、軸

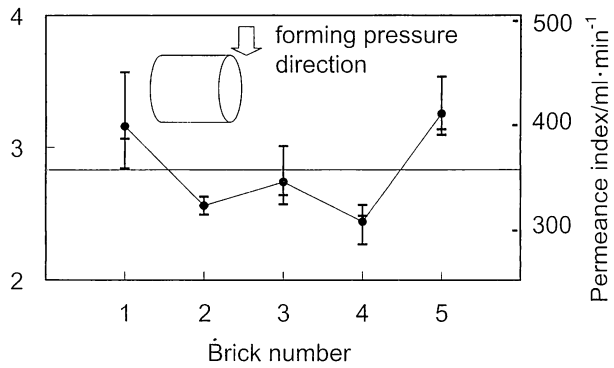


Fig. 7 Comparison between permeability results of two sampling directions for alumina brick A test pieces - represents the 3 measured values of each test piece. ● represents the average of the 3 values of each test piece. — represents the average value of all test piece measurements.

方向測定グループの中の一つの試験片（ここでは、この試験片をA-1-1と言う）であるので、表4と表6は容易に対比できる。先ず気付くことは、表6の軸方向測定グループの平均値 $269.3 \times 10^{-15} \text{m}^2$ に対して、表4のA-1-1の平均値 $310.4 \times 10^{-15} \text{m}^2$ が表6の軸方向測定グループの平均値よりも $+41.1 \times 10^{-15} \text{m}^2$ も高い値を与えていることである。このような差が生じた要因を表4と表6の標準偏差（ σ ）を対比して考えて見たい。先ず、 $3 \cdot 1 \cdot 1$ 項でも述べたように表4の日間繰返精度 $\sigma = 4.2 \times 10^{-15} \text{m}^2$ は、個々の試験片の通気率を高い精度で測定していることを示すもので、図7でA-1-1の通気率が表4の平均値より僅か $3.9 \times 10^{-15} \text{m}^2$ 低い $307.5 \times 10^{-15} \text{m}^2$ であったことから判る。ここで表4の平均通気率が同一試料の日間繰返し結果の平均値であるのに対して、表6の平均通気率は多数の異なる試験片の平均値であることに注目しなければならない。表6の軸方向測定グループの群内差（同一れんがの試験片間差） σ を見ると $28.4 \times 10^{-15} \text{m}^2$ と表4の繰返測定誤差の7倍も大きい。このことは、試験片間の通気率値の差が日間繰返精度（誤差）と比較にならない程大きいことを示している。一般に、5%有意水準での母集団の分散は、 $\pm 1.96 \sigma$ （以下 $\pm 2 \sigma$ に丸めて示す）であるので、れんが1の平均通気率 $254.2 \times 10^{-15} \text{m}^2$ [図7a) 1番目のれんがのA-1-1および他の2試験片の測定値（●）の平均値] に対して 2σ に相当する $\pm 56.8 \times 10^{-15} \text{m}^2$ を加えると $197.4 \sim 312.0 \times 10^{-15} \text{m}^2$ となり、試験片A-1-1の通気率 $307.5 \times 10^{-15} \text{m}^2$ （図7作成時測定値、表4の平均値は $310.4 \times 10^{-15} \text{m}^2$ ）は、この範囲内に入っており、試験片間の通気率測定値の分散の大きいこの母集団における統計値としては異常値と言えない。すなわち、表4の検討に用いたA-1-1が、軸方向測定グループの中でも比較的通気率が高い試験片だったわけである。れんが内の試験片間には、これほどまでに通気率の差があり、れんが組織もまた、通気率値から見る限り非常に不均質であるといえる。このことから、通気率によって同一れんが内の組織の不均質性を容易に評価できると結論される。

Table 6 Test results for reproducibility within the same and different alumina brick A

Permeance direction	Forming pressure direction		Direction perpendicular to forming pressure	
Kind of test pieces	within brick	Different bricks	within brick	Different bricks
AoP/ $\times 10^{-15} \text{m}^2$	269.3		283.1	
$\sigma / \times 10^{-15} \text{m}^2$	28.4	16.8	23.7	36.0
RSD/%	10.5	6.2	8.4	12.7

AoP : Average of permeability
within brick : difference between 3 values from one brick
Different bricks : difference between 5 brick

表6のれんが間差（群間差） σ は、同一れんがの3試験片の平均値（図7の●）を代表値とした5点の通気率値間の標準偏差であり、成型圧軸と同一方向の場合の $16.8 \times 10^{-15} \text{m}^2$ も直角方向の場合の $36.0 \times 10^{-15} \text{m}^2$ も、表4の日間変動誤差 $4.2 \times 10^{-15} \text{m}^2$ を大きく上回っている。最初に提示した仮定である“通気率によって試料間の個体差の識別が可能性であるか”については、少なくとも、このれんがについては、確実に識別できると言える。

一方、れんが成形時の成型圧方向（軸方向測定グループ）とその直角方向（直角方向測定グループ）各15試料の通気率平均値を比較すると、直角方向が $13.8 \times 10^{-15} \text{m}^2$ だけ高い値を示している。そこで、成型圧方向と直角方向の値に有意な差（すなわち、成型時の圧力の影響）があるか否かを次式(3)¹¹⁾によって検定した。

$$t_0 = \frac{|\bar{x}_2 - \mu| \sqrt{lm_2}}{\sqrt{V_{R2}}}$$

(3)

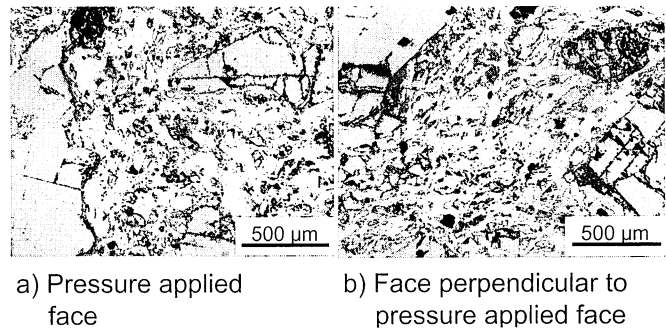
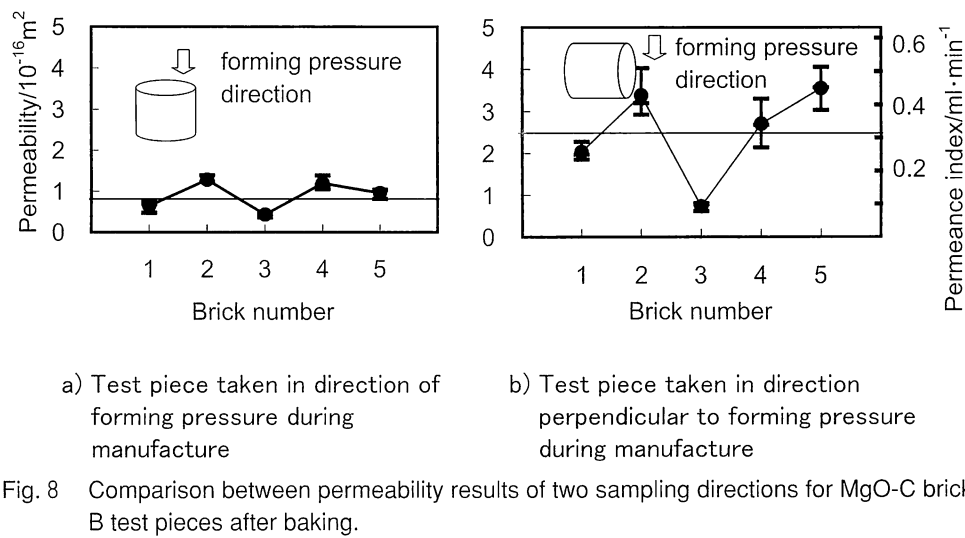
ここに、 \bar{x}_2 : 直角方向の通気率の平均値 ($2.831 \times 10^{-15} \text{m}^2$)
 μ : 成型圧方向の通気率の平均値 ($2.693 \times 10^{-15} \text{m}^2$)
 l : 試料数 (れんがの数) (5 個)
 m_2 : 繰返数 (3 回)
 V_{R2} : 直角方向の試料間分散 (0.3893)

計算値 $t_0=0.86$ は、スチューデントの $t(4,0.05) = 2.776$ よりも小さいので、危険率0.05の確率で両者の間に偏りが有るとは言えないことを示している。このことは、この焼成れんがは、試験片を成型圧方向に採ろうと直角方向に採ろうと通気率に有意な差があるとはいえず、成型時の加圧によって生じるかもしれない粒などの配向性も、通気率の面からは確認できないといえる。

3・2・2 MgO-Cれんがの試料間差と配向性の検討

同様に、2・2節の(1)のMgO-CれんがBの通気率測定結果を図8に示す。図から高アルミナれんがAと同様に、同一れんが内の3試験片間、および、れんが間に通気率の差が認められことから、通気率によって“れんが内の試験片間差”および“れんが間の個体差”の識別が可能性であると言える。なお、れんが1とれんが3は、3試験片間の通気率の差が小さく、通気率自体も低い傾向にある。図8の成型圧方向とその直角方向の通気率（平均値）は、各々 $0.813 \times 10^{-16} \text{m}^2$ および $2.484 \times 10^{-16} \text{m}^2$ であり、両者に差があるように見える。そこで両者の間に有意な差があるか否か式(3)を用いて解いた。その解は $t_0=3.25$ となり、 t 分布の $t(4,0.05) = 2.776$ よりも大幅に大きな結果となった。このことから、統計的にも成型圧方向と直角方向の通気率の間に偏りがあると結論される。図9に示すMgO-CれんがBの成型圧面とその直角面の顕微鏡写真からこのような結果

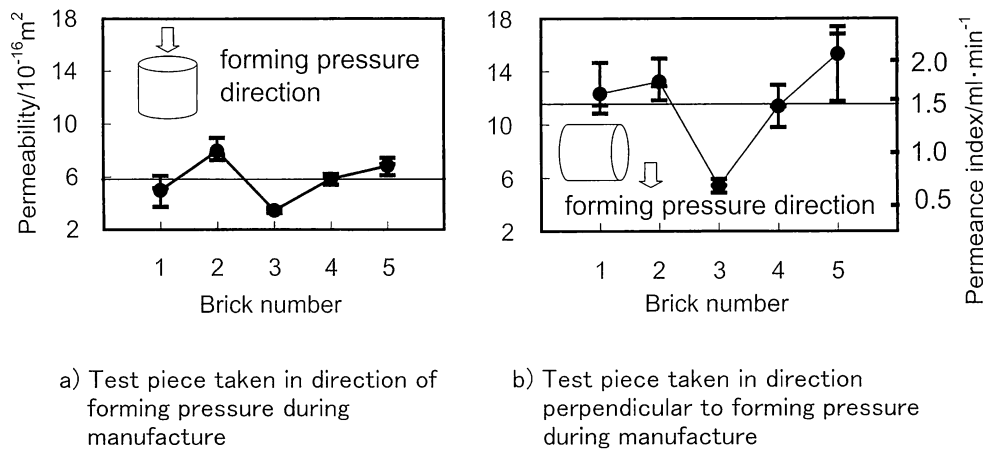
朝倉秀夫 他 通気率における測定条件の影響および通気率試験方法の耐火物評価への応用



を与えた要因を探った。顕微鏡写真から成形圧面には板状に圧縮されたような黒鉛が見られるのに対して、その直角面には、断面状の黒鉛が認められる。すなわち、成形圧方向では、板状になった黒鉛面が抵抗となりガスが流れ難いに対して、成形圧に直角方向では、黒鉛断面の隙間を通してガスが流れ通気率も高い数値を示したものと推察される。以上のことから、MgO-Cレンがは、成形時に黒鉛の

配向が起こり、ベーキング品では、直角方向の通気率の方が成形圧方向の通気率よりも約3倍も高くなることが確認された。

図10に、図8で測定した同じ試験片の1000℃焼成後品の通気率測定結果を示す。図から1000℃焼成後品においても、レンが1とレンが3は、ベーキング品と同様に3試験片間の差が小さく、通気率自体も低かった。このことから、こ



の2個のれんがは、相対的に他のれんがよりも均質で緻密な組織を持っているものと考えられる。また、焼成によって通気率は上昇し、ベーキング品に比し、成形圧方向で7.2倍、その直角方向で4.6倍となっている。直角方向/成形圧方向の通気率の比は、ベーキング品で3.1倍だったものが、1000℃焼成品では2.0倍と相対的に縮まっている。この通気率の直角方向/成形圧方向比の縮小は、試験片中でのガスの流れが単純な直線的なものでなく、蛇行して流れているため焼成によって通気率が高くなっただけ相対的に平板状黒鉛の影響も小さくなったものと考えられる。また、成形圧方向と直角方向の有意差は、ベーキング後品とほぼ同じ $t_0=3.44$ であることから焼成後も成形圧方向と直角方向の通気率の間に顕著な差が残存しているといえる。MgO-Cれんがでは、添加された黒鉛の配向性によってベーキング品も1000℃焼成品も成形圧方向よりもその直角方向の通気率が高い値を示すことが確認された。

3・3 通気率のキャストブル解析への適用

キャストブル内部で発生した水蒸気の外部への放出の評価に通気率が有効とされていることから、本節では、通気率を一つのツールとしてキャストブル混練品の再現性、添加水分量と通気率の関係、加熱による気孔変化の解明に適用した。

3・3・1 混練品の再現性

2・2節の(2)1)で調製した15個の試験片の通気率を差圧30kPa、60kPaおよび90kPaで測定した。図11に測定結果を示す。図を見るとバッチ3の3試験片のバラツキが非常に大きく、バッチ2とバッチ4は、各3試験片間に殆どバラツキが認められない。これら測定結果を統計処理すると、平均通気率 $4.71 \times 10^{-15} \text{m}^2$ 、バッチ内標準偏差 $0.70 \times 10^{-15} \text{m}^2$ 、バッチ間標準偏差 $0.75 \times 10^{-15} \text{m}^2$ であり、F検定の F_0 は、3.40となり、 $F_0 < F(4,10;0.05)=3.48$ から危険率0.05でバッチ間に偏りがあるとは言えないと解析された。なお、バッチ内およびバッチ間の相対標準偏差(RSD)は、各々15%、16%と計算され、表4のキャストブルDの

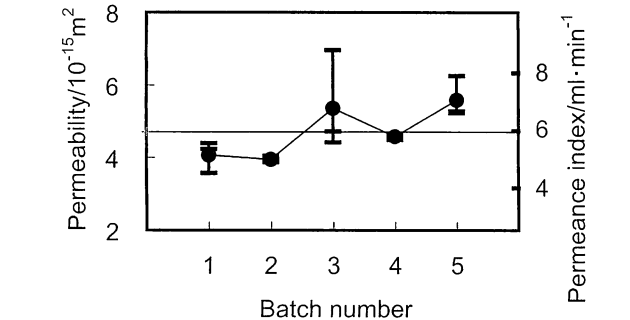


Fig. 11 Permeability results of castable D test pieces after drying at 110℃.

同一試験片の日間繰返精度RSD 8.1%よりもかなり大きいことから、図11のデータの分散は、試験片間の差を反映したものであり、通気率によってバッチ内およびバッチ間の差を評価すること自体は可能といえる。なお、F検定によって、5バッチ間に差があると言えないと結論付けられたこと、ならびに、バッチ内およびバッチ間にRSDとして各々15%、16%の分散があることを念頭に入れ、以降の実験を進めることにした。

3・3・2 添加水分量と通気率の関係

2・2節の(2)2)で調製した添加水分量の異なるキャストブルDの通気率測定結果を図12に示す。上述した試験片間の分散も考慮に入れて全体を見ると、養生後品、乾燥後品、焼成品共に添加水分量が増加するに伴い、大きく通気率が高くなる傾向が認められる。特に、添加水分量7.25% (+0.50%)の通気率は、添加水分量6.25% (-0.50%)の通気率に比し養生後品、乾燥後品、焼成品共に約3倍になっており、キャストブルの通気率に添加水分量が大きく関わっていることが判る。

3・3・3 加熱温度による気孔変化の解析

図13に2・2節の(2)3)で調製したキャストブルDの通

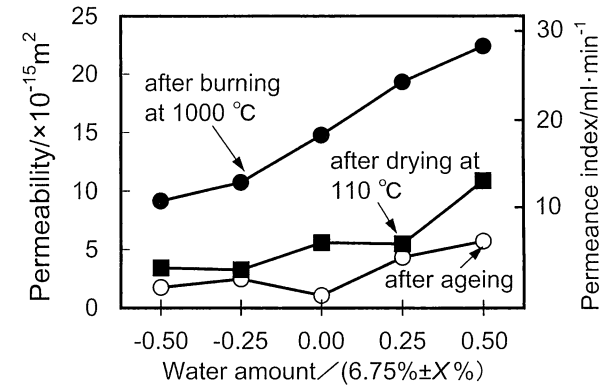


Fig. 12 Relation between water amount and permeability for castable D.

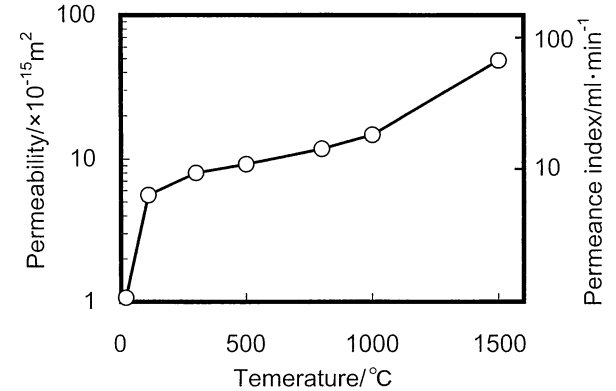


Fig. 13 Change in permeability by heating of castable D.

朝倉秀夫 他 通気率における測定条件の影響および通気率試験方法の耐火物評価への応用

気率測定結果を示す。加熱によって通気率は、20℃養生時に対して、110℃で約5倍、500℃で約10倍、1000℃で約15倍、1500℃で約50倍と漸次増加している。この加熱による通気率の増加は、加熱による試験片中の水分の蒸発などに伴い、ガス通路となる気孔が生成・成長していることを示唆している。そこで通気率と関りの深い見掛気孔率（通気率測定後試験片使用、媒液：20℃は白灯油、その他は水）と水銀ポロシメータによる気孔径分布（見掛気孔率測定後試料を110℃で16h乾燥、20℃試料は測定せず）を測定した。図14に加熱による見掛気孔率および平均気孔径の変化を示す。図14(a)の結果を見ると、20℃で15.0%だった見掛気孔率が、加熱温度と共に110℃で18.8%、500℃で21.1%、1000℃で22.9%、1500℃で25.7%と漸次増加している。ここで、20℃と1000℃および20℃と1500℃の見掛気孔率の差は、各々7.9%および10.7%であり、添加水分量6.75%の揮散だけでは説明できない。800℃（気孔率22.1%）回りから焼結などによる気孔拡大が起こったと考えられる。一方、図14(b)を見ると、温度と平均気孔径曲線の間に、通気率とも見掛気孔率とも異なる傾向が窺われる。110℃でφ240nmだった平均気孔径が、300℃および500℃で約φ100nmに低下して推移し、800℃でφ260nmと増加に

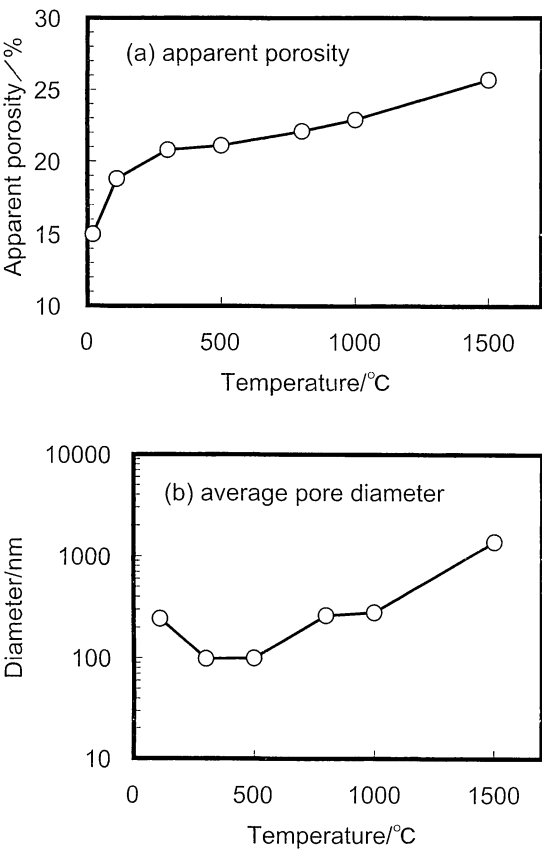


Fig. 14 Change in apparent porosity and average pore diameter by heating of castable D test piece.

転じ、1000℃でφ280nm、1500℃でφ1400nmとなっている。図15に各温度で熱処理された試験片の気孔径分布曲線を示す。図15(a)が110℃および300℃の気孔径分布を、また、図15(b)が代表的な温度における気孔径分布である。これら結果から、まず注目されるのは、図15(a)の300℃の分布曲線においてφ10~100nmの気孔径が110℃のものに比べて大幅に増加していることである。このことは、110℃~300℃までの間にキャスト部微粉部の結合に関与していた水分が見掛気孔率で2%相当蒸発しているが、キャスト内部に新しく生成された気孔の径は、φ10~100nmと非常に小さいことを示唆しており、この小気孔が300℃においても110℃と殆ど差の無い $8 \times 10^{-15} \text{m}^2$ （通気指数 $10 \text{ml} \cdot \text{min}^{-1}$ ）と低い通気率要因となり、キャスト内部でその間に生成される2%もの多量の水蒸気の系外への放出を困難にする要因となっているように考えられる。なお、図15(b)から300℃で生成したφ10~100nmの気孔は、加熱温度が高くなるにつれて低下して行き1500℃では、殆ど認められなくなっている。一方、低温乾燥域での中心的な気孔の径は、φ400~500nmであり、これらが水蒸気の系外への通気を担っていると考えられる。これら気孔も1000℃、1500℃と加熱して行くにつれて気孔径が増し、1500℃焼成後品ではφ1400nm近辺に中心を持つ大きさにまでなっている。気孔径の上昇は、焼結現象によるもので見掛気孔率の増加とも符合すると考えられる。一方、これら不定形耐

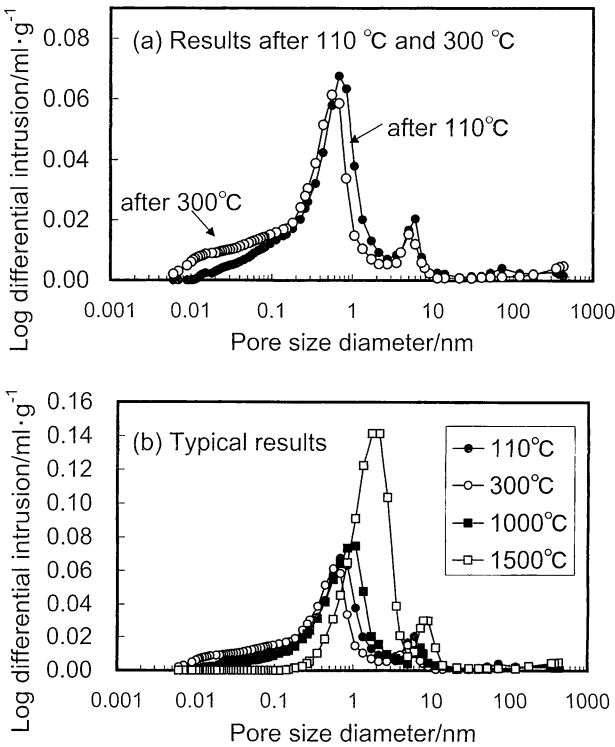


Fig. 15 Pore size distribution curve of castable D test pieces after heating.

火物の平均気孔径は、図3および図15に見られるように1500℃で焼結したものでさえ ϕ 1400nmとプレス成形焼成れんがの ϕ 数千nmなどと比べて小さく、その結果として通気率も図2および図15に見られるように焼成れんがに比べて一桁も低い値となっているものと考えられる。

4 結論

本稿では、通気率測定値の変動要因として測定精度、試料中を流れる流体の特性、有効な測定値を得るための測定条件などの解明に当たった。また、これら検討結果をベースに通気率を実際の耐火物の解析に適用することを試みた。その結果、次の結論を得た。

- (1) 通気率測定値の日間繰返精度RSDは、通常の各種測定と同様に通気率の高い領域で良好（例えば、 $300 \times 10^{-15} \text{m}^2$ 近辺で1.4%）で、通気率が低くなるにしたがって低下（ $1 \times 10^{-15} \text{m}^2$ 近辺で8.1%）する。
- (2) 通気率は、気孔率よりも気孔径と密接に関係している。
- (3) 試験片中の流体は、ダルシーの法則に基づき穏やかな層流として流れていると言うよりも、弱い乱流の要素を持って複雑に流れているものと推察される。また、通気率測定値は流体の密度の影響を受けているのではないかと推察される。
- (4) 通気率測定値は、5～30kPa域で安定した値が得られるので、10kPa、20kPaおよび30kPaの3点で測定し、その平均値を報告値とすることが推奨される。
- (5) 通気率は試験片の厚みの影響を受けない。低通気率試料では、試料を代表できる範囲内の薄肉化によって測定精度を高めることができる。
- (6) 通気率によって、れんが間の個体差および同一れんが内の採取位置による差が識別できた。MgO-Cれんがでは、成形時に起こる黒鉛の配向による加圧方向と直

角方向の通気率の差を明確に検出できた。

- (7) キャスタブルの解析に通気率を適用し、通気率によって混練品相互間および同一混練品内の試験片間の差が評価できること、通気率が添加水分量の僅かの差で大きく変化すること、また、300℃位までに生成される気孔の径は ϕ 10～100nmと小さく通気率を高める効果に乏しいことなどが判った。

謝辞

本稿の実験のために試料を提供頂きました東備地域の当所会員企業の皆様のご好意に心から感謝申し上げます。また、装置開発および装置改造に協力頂きましたセリオ株式会社に謝意を表します。

文献

- 1) 池ノ上典，古海宏一：耐火物工業，3 [9] 17-21 (1951).
- 2) 朝倉秀夫：セラミックス岡山，16，62-64 (2008).
- 3) 朝倉秀夫，馬場直樹，前田朋之，山口明良：耐火物，61 [3] 142 (2009).
- 4) 日本規格協会編：JIS R 2115：2008，(2008) pp.4-5.
- 5) 日本規格協会編：JIS R 2115：2008解説，(2008) pp.解4-5.
- 6) 水収支研究グループ編：「地下水資源・環境論—その理論と実践—」，共立出版 (1993)，P.350.
- 7) 日本熱物性学会編：新編熱物性ハンドブック 養賢堂 (2008)，P.60.
- 8) 日本規格協会編：JIS R 2115：2008，(2008) p.2.
- 9) 物理学辞典編集委員会：物理学辞典 —縮刷版— 培風館 (1986)，pp.12-13.
- 10) ISO/TC33：ISO 8841：1991，(1991) p.1.
- 11) 日本規格協会編：JIS Z 8402：1991，(1991) pp.44-46.

Report

Densification Effect of Al₄SiC₄ Added to Alumina Carbon Refractories

YASUHIRO HOSHIYAMA, AKIRA YAMAGUCHI and JUNJI OMMYOJI

Key words: Al₄SiC₄, Al₂O₃-C, addition effect

1. Introduction

It is important to select additives to refractories that are well adapted to the operation conditions of steel making because the properties of carbon-containing refractories vary with metal antioxidants and nonoxides such as carbides. Recently, Al-Si-C system complex carbides have been investigated as new refractories additives¹⁻¹³⁾. There are various complex carbides of the Al-Si-C system, for instance; Al₄SiC₄, Al₄Si₂C₅, Al₄Si₃C₇, Al₄Si₃C₆ and Al₈SiC₇. Among them, Al₄SiC₄ is a promising additive to carbon-containing refractories because it is stable over a wide temperature range, has a high melting point (see Fig. 1¹¹⁾) and has superior slaking resistance¹⁾.

This paper presents the results of an investigation on the effects of Al₄SiC₄ addition on the densification of an alumina-carbon refractory (hereafter called Al₂O₃-C refractory). The results are discussed relative to SiC that is a commonly used additive to Al₂O₃-C refractories.

2. Experiments

A mixture of aluminum powder (−63 μm), silicon powder (−45 μm) and carbon black (−60 nm) having the mineral composition equal to theoretical Al₄SiC₄ was milled in a dry ball mill for 10 hours, placed in a carbon crucible and heated in an

argon atmosphere at 1700°C to form Al₄SiC₄ powder. The product was milled again in a dry ball mill for 10 hours to a fine Al₄SiC₄ powder with size smaller than 20 μm. The fine powder was sintered by the spark plasma sintering to form sintered aggregates. The aggregates were ground to grains 0.3~0.8 mm in diameter which was used as an additive to the Al₂O₃-C refractory for this investigation.

Table 1 shows the compositions of three kinds of test samples: namely, Sample No. 1 contains neither SiC nor Al₄SiC₄, Sample No. 2 contains SiC and Sample No.3 contains Al₄SiC₄.

Each sample shown in Table 1 was pressed at 127 MPa pressure to form green shapes which were heated at 200°C for 6 hours to consolidate the specimens. The specimens were then buried in carbon powder and heated in an electric furnace in an air atmosphere at prescribed temperatures and times.

The mass, apparent porosity, crushing strength, pore diameter distribution (by mercury porosimetry) and crystal phase (by X-Ray Powder Diffraction) were measured after heating.

3. Results and Discussion

Figure 2 shows the relative change in mass with heating temperature. The standard mass value was the mass of each specimen heated at 200°C for 6 hours. The weight loss of the specimens heated to 800°C was caused by carbonization of the phenol resin binder. The changes in mass when the heating temperatures were higher than 800°C were caused by certain reactions in each specimen. The decrease in mass of the specimen made from the Sample No. 3 (hereafter called Specimen No. 3, and so forth) containing Al₄SiC₄ was smaller at 800°C than that of the other specimens, and the mass increased substantially from this point as the heating temperature

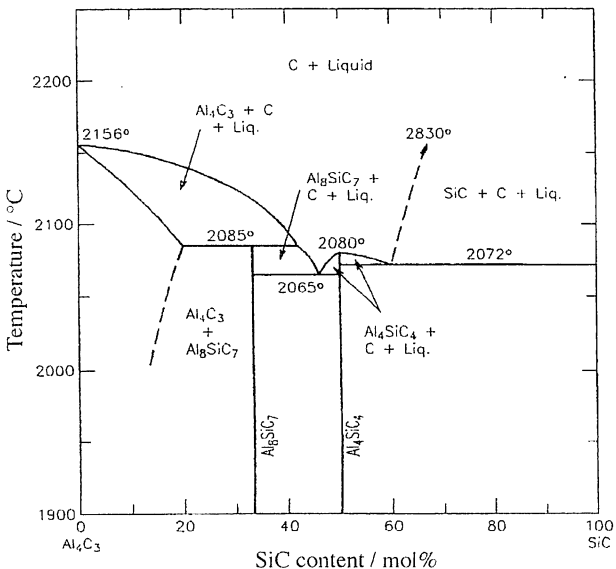


Fig. 1 Phase diagram for pseudobinary Al₄C₃-SiC system.

Table 1 Composition of Al₂O₃-C samples/mass%

No.		1	2	3
Fused alumina − 1 mm		85	75	75
Flake graphite − 150 μm		15	15	15
SiC	0.8 − 0.3 mm	−	5	−
	− 45 μm	−	5	−
Al ₄ SiC ₄	0.8 − 0.3 mm	−	−	5
	− 20 μm	−	−	5
Phenol resin (novolak type)		ex. 4	ex. 4	ex. 4
Hexamethylenetetramine		ex. 0.4	ex. 0.4	ex. 0.4

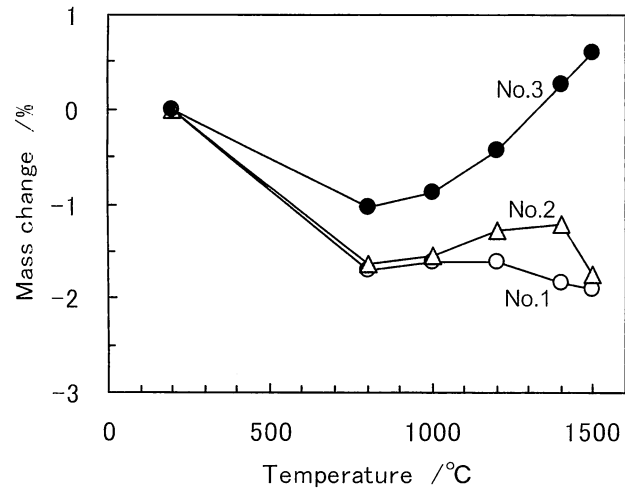


Fig. 2 Relative change in mass of $\text{Al}_2\text{O}_3\text{-C}$ samples with heating temperature.

increased. On the other hand, the loss of mass of Specimen No.2 containing SiC was nearly equal to that of the Specimen No. 1 with neither SiC nor Al_4SiC_4 when the heating temperatures was 1500°C , although the mass of Specimen No. 2 increased slightly between 1200°C and 1400°C . These facts suggest that a reaction concerning Al_4SiC_4 starts from a temperature lower than 1000°C and continues to 1500°C ; namely, a reaction happening over the wider temperature range brings a larger mass increase than a reaction concerning SiC happening only in the narrow range of $1200^\circ\text{C} \sim 1400^\circ\text{C}$.

Figure 3 shows the apparent porosity of specimens heated in carbon powder. The increase in porosity of the specimens heated at 800°C was caused by the carbonization of the phenol resin. The apparent porosity of Specimen No. 1 without Al_4SiC_4 or SiC increased as the heating temperature increased, that of Specimen No. 3 with Al_4SiC_4 decreased linearly and that of Specimen No. 2 with SiC decreased between 800°C and 1200°C , increased from 1400°C and reached the same value as that of Specimen No. 1 when heated at 1500°C . These changes in the apparent porosity coincide well with the mass changes shown in Figure 2. Therefore, it can be said that the decrease in porosity is brought about by a certain reaction accompanying the increase in mass. Namely, Al_4SiC_4 brings about the densification of the $\text{Al}_2\text{O}_3\text{-C}$ refractory structure by a reaction accompanying the increase in the mass as shown in Fig. 2. It is clear that the temperature range where the effect of Al_4SiC_4 is valid is wider than that of the SiC effect. The fact that the porosity of Specimen No. 3 is less than that of the other specimens by as much as 5% proves that Al_4SiC_4 has a large densification effect at 1500°C . It is a promising result to improve an $\text{Al}_2\text{O}_3\text{-C}$ refractory erosion resistance, wear resistance and oxidation resistance because these performances become better as the porosity decreases. It is hopeful that the addition of Al_4SiC_4 makes the erosion resistance, wear resistance and oxidation resistance stronger because of all the above mentioned resistances become better as the apparent porosity becomes less.

Figure 4 shows the crushing strength of the specimens heated in carbon powder. The crushing strength decreased at

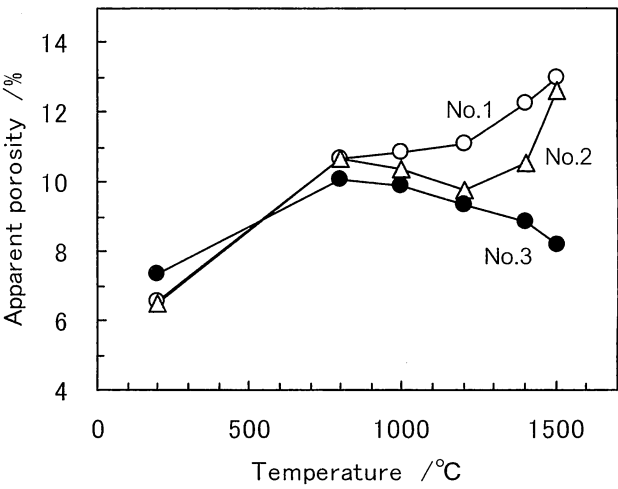


Fig. 3 Change in apparent porosity of $\text{Al}_2\text{O}_3\text{-C}$ samples with heating temperature.

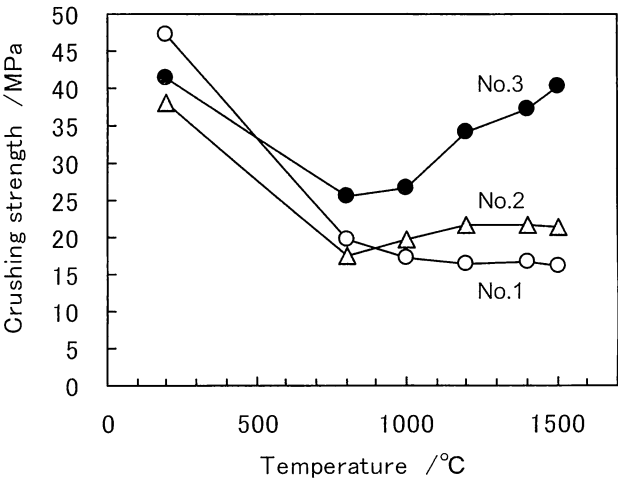


Fig. 4 Change in crushing strength of $\text{Al}_2\text{O}_3\text{-C}$ samples with heating temperature.

800°C because of the carbonization of phenol resin. The crushing strength of Specimens No. 2 and No. 3 increased at temperatures higher than 800°C because of a certain reaction. The crushing strength of Specimen No. 2 increased slightly from 800°C to 1200°C and decreased a little from 1400°C to 1500°C . On the other hand, that of Specimen No. 3 increased extremely as the heating temperature rises. Especially, the value at 1500°C was about two times that of the other specimens. These transitions of crushing strength are coincident to those of the mass (Fig. 2) and the porosity (Fig. 3). It is hopeful that the addition of Al_4SiC_4 makes the wear resistance of $\text{Al}_2\text{O}_3\text{-C}$ refractory stronger, because the wear resistance becomes higher as the mechanical strength becomes higher.

Figure 5 shows the change in the mean pore diameter with the heating temperature. The mean pore diameter of Specimen No. 3 containing Al_4SiC_4 decreased significantly from 1200°C to 1500°C . Although the mean pore diameter of Specimen No. 2 containing SiC was slightly reduced when the heating temperature was 1200°C and higher, the pore size reduction effect of Al_4SiC_4 was larger. It is hopeful that the addition of Al_4SiC_4 increases both the resistance of the pores against the penetration of molten steel and the resistance against the

Densification Effect of Al_4SiC_4 Added to Alumina Carbon Refractories

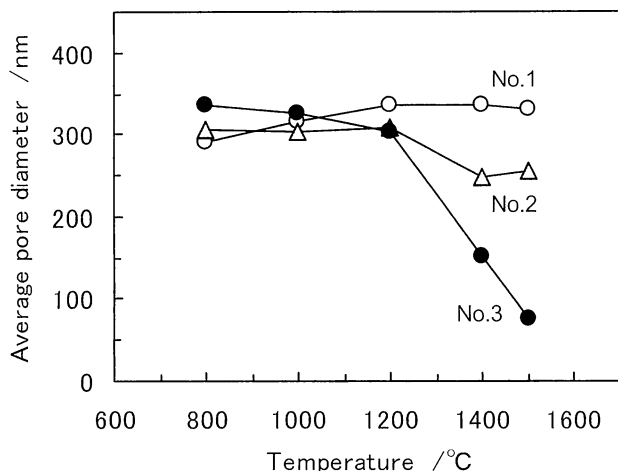


Fig. 5 Change in average pore diameter of Al_2O_3 -C samples with heating temperature.

oxidation of carbon in the Al_2O_3 -C refractory because both the penetration of molten steel and the oxidation of carbon decrease as the pore size becomes smaller.

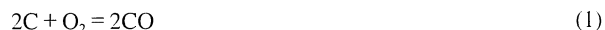
Figure 6 shows the X-Ray Powder Diffraction (hereafter called the XRD) analyses of Specimens No.2 and No. 3 heated in carbon powder. The facts that the amount of Al_4SiC_4 in Specimen No. 3 decreased as the heating temperature rises and the SiC peak appeared at 1200°C and above clarifies that an Al_4SiC_4 reaction progresses as the heating temperature rises. On the other hand, the fact that the amount of SiC in Specimen No. 2 decreased as the heating temperature rises to 1400°C and then suddenly increased at 1500°C shows that a SiC reaction nearly stops at 1400°C.

Al_4SiC_4 added to Al_2O_3 -C refractory brought effects such as densification, an increase in strength and the reduction in pore size by means of a reaction accompanied with an increase in weight as shown in Figs. 2~5. On the other hand, SiC brought effects like the ones brought by Al_4SiC_4 in the range between 1200°C~1400°C, but it was not effective at 1500°C. These phenomena are discussed thermodynamically as follows.

The gas filling the pores is an important factor in considering reactions of a carbonized material in a carbon-containing refractory. The surface of a carbon-containing refractory is exposed to the atmosphere in the operation of almost all furnaces

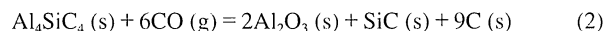
and vessels for steel making. In this case, the inside of a carbon-containing refractory is filled with CO and N_2 at a temperature higher than 1000°C, and the main reaction of carbonized materials is a reaction with CO.

The partial pressure of CO in a carbon-containing refractory is $P_{CO} = 0.355 \times 10^5$ Pa, when O_2 in the atmosphere is changed to CO by Equation (1) and the total pressure is held at 1.013×10^5 Pa (1 atm).

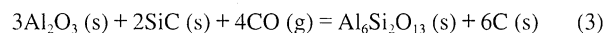


The condition of the specimen heated in carbon powder is analogous to the above mentioned one, namely, it can be considered that the environment of both the exterior and interior of the specimen has a partial pressure of 0.355×10^5 Pa CO when carbon coexists.

The changes in mineral phases shown in Figure 6 (No. 3) can be expressed with Equation (2) forming Al_2O_3 and C as well as SiC.



The reaction forming SiO_2 and C from SiC and CO happens after Al_4SiC_4 changed to Al_2O_3 and SiC and disappeared, as the result, the following reaction progresses.



Both the Equations (2) and (3) express that CO (g) taken in an Al_2O_3 -C refractory deposits as C (s) making a mass increase, a porosity decrease, a more dense structure and higher mechanical strength.

Figure 7 shows the stability domains of condensed phases in the Al-Si-O-C system obtained by calculating from the thermodynamic data the temperature conditions necessary for both Equations (2) and (3) to progress to the right side^{14), 15)}. The y-axis is the dimensionless partial pressure normalized by dividing an actual measurement value by 1×10^5 Pa being the standard pressure of the SI Unit (hereafter called P^0). The curves in Fig. 7 show the boundaries of stable condensed phases. Figure 7 indicates that $\{Al_2O_3 + SiC + C\}$ and $\{Al_6Si_2O_{13} + Al_2O_3 + C\}$ are more stable than $\{Al_4SiC_4 + C\}$ under the

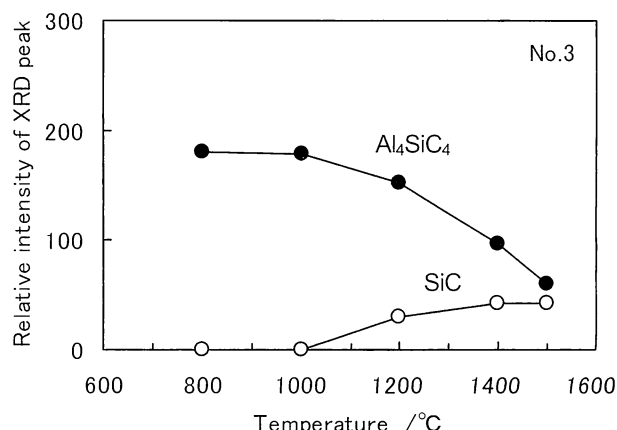
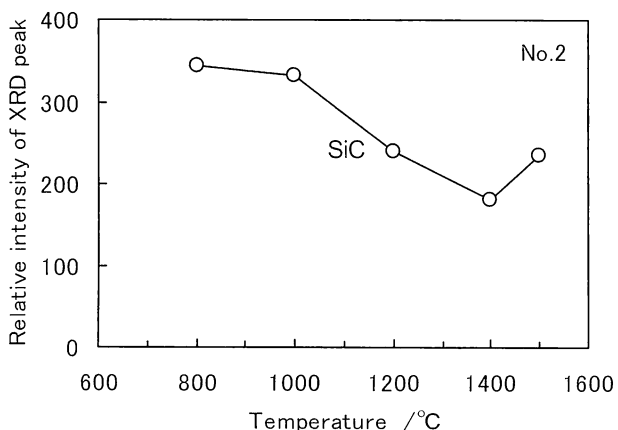


Fig. 6 Change in mineral phases of Al_2O_3 -C samples with heating temperature.

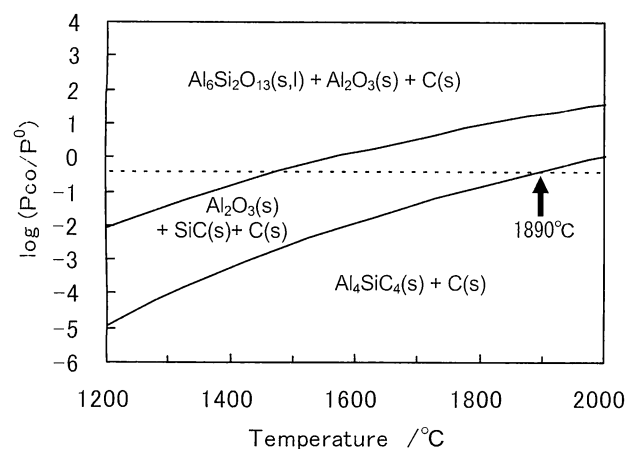


Fig. 7 Stability domains of condensed phases in the Al-Si-O-C system.

condition of $P_{co} = 0.355 \times 10^5$ Pa ($\log(P_{co}/P^0) = -0.450$) in the temperature range lower than 1890°C . Namely, it means that Equation (2) progresses to the right hand side. The heating temperatures of the specimens in carbon powder in this investigation were in the range that Equation (2), being a densification reaction, progresses to the right hand side. This consideration agrees with the experimental results mentioned above. Therefore, it can be expected that Al_4SiC_4 added to an $\text{Al}_2\text{O}_3\text{-C}$ brick used in high temperature conditions between $1300^\circ\text{C} \sim 1800^\circ\text{C}$, such as a steel making furnace or vessel, reacts in accordance with Equation (2) to densify an $\text{Al}_2\text{O}_3\text{-C}$ brick.

Figure 8 shows the stability domains of condensed phases in the Si-O-C system for the SiC reaction expressed by Equation (4) from the thermodynamic data⁽¹⁴⁾.

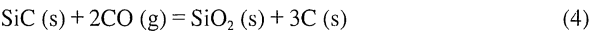


Figure 8 states that $\{\text{SiO}_2 + \text{C}\}$ is more stable than $\{\text{SiC}\}$ in the temperature range below 1430°C under the condition of $P_{co} = 0.355 \times 10^5$ Pa ($\log(P_{co}/P^0) = -0.450$), namely, the reaction of Equation (4) progresses to the right side. However, $\{\text{SiO}_2 + \text{C}\}$ is less stable than $\{\text{SiC}\}$ in the temperature range higher than 1430°C , namely, the reaction of Equation (4) progresses to the

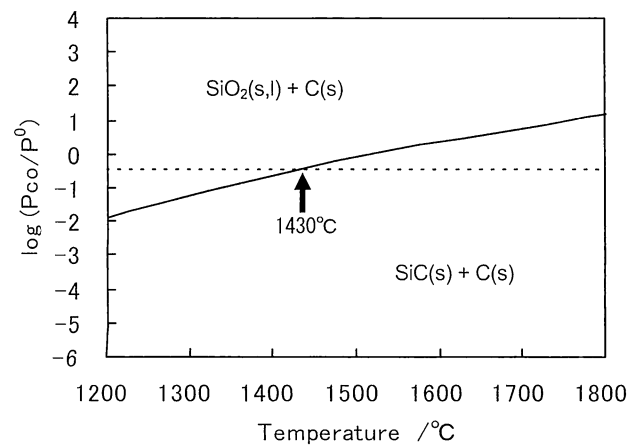


Fig. 8 Stability domains of condensed phases in the Si-O-C system.

left side. This transition temperature, or the phenomenon, agrees well with the XRD analysis shown in Fig. 6 (No.2). It is considered that the decrease in the effect of SiC in the high temperature range shown in Figs. 2~5 was caused by the reversal mentioned above.

This reversion phenomenon is a serious problem for the actual performance of SiC-added $\text{Al}_2\text{O}_3\text{-C}$ refractories. For instance, in the case of a steel making process operated between $1300^\circ\text{C} \sim 1800^\circ\text{C}$ Equation (4) progresses to the right side and densification happens in the inner part where the temperature is lower than 1430°C . As the wear progresses and the inner part reaches a temperature higher than 1430°C Equation (4) progresses to the left and the densification effect of SiC will be lost and the structure will be weakened. Considering that it is important from the view point of wear resistance to make the structure near the hot face strong, the behavior of SiC mentioned above is not favorable for a refractory operated at temperatures higher than 1430°C . On the other hand, Al_4SiC_4 demonstrates a densification effect up to 1890°C . Therefore, the hot face part of an $\text{Al}_2\text{O}_3\text{-C}$ refractory with Al_4SiC_4 added keeps a sound structure at temperatures between $1500^\circ\text{C} \sim 1800^\circ\text{C}$ and Al_4SiC_4 will contribute to the reduction of the wear rate.

4. Conclusion

The effect of Al_4SiC_4 addition on the densification of an $\text{Al}_2\text{O}_3\text{-C}$ refractory was compared with that of SiC. The results were as follows:

- (1) The increase in the mass of an Al_4SiC_4 -containing $\text{Al}_2\text{O}_3\text{-C}$ refractory when heated in carbon powder was caused by the deposition of carbon generated by the reaction between Al_4SiC_4 and CO in the refractory. The deposition of C densified the structure, increased in the strength and reduced the pore diameter.
- (2) It was observed that the reaction between SiC and CO in SiC-added $\text{Al}_2\text{O}_3\text{-C}$ refractory brought the same effects as those of Al_4SiC_4 . However, the effective temperature range was $1200^\circ\text{C} \sim 1400^\circ\text{C}$ and the effects were scarcely observed at 1500°C .
- (3) The above mentioned results agree well with the relation between the temperature and the stability domains of condensed phases predicted by the thermodynamic data. Al_4SiC_4 exhibits a densification ability up to 1890°C but SiC does so up to only 1430°C . Therefore, it is assumed that the effect with SiC disappears at temperatures higher than 1430°C .

It can be expected that the erosion resistance, wear resistance, oxidation resistance and molten steel penetration resistance of an $\text{Al}_2\text{O}_3\text{-C}$ refractory is improved by adding Al_4SiC_4 by making the of $\text{Al}_2\text{O}_3\text{-C}$ refractory structure dense.

References

1) S. Zhang and A. Yamaguchi, J. Ceram. Soc. Japan, 103 [1] 20-24 (1995).

Densification Effect of Al_4SiC_4 Added to Alumina Carbon Refractories

- 2) S. Zhang and A. Yamaguchi, *ibid*, 103 [3] 235-239 (1995).
 - 3) S. Zhang and A. Yamaguchi, *Proc. UNITECR '97*, Vol. 2 (1997) pp. 861-869.
 - 4) K. Inoue, S. Mori and A. Yamaguchi, *J. Ceram. Soc. Japan*, 111 [2] 126-132 (2003).
 - 5) K. Inoue, S. Mori and A. Yamaguchi, *ibid.*, 111 [5] 348-351 (2003).
 - 6) W. Roger and G. Steve, *Ceram. Eng. Sci. Proc.*, 26 [3] 181-188 (2005).
 - 7) A. Yamaguchi and K. Inoue, *CERAMIC DATA BOOK 2006*, Kogyo-Seihin-Gijutu-Kyokai, pp 136-139.
 - 8) M. Fujita, J. Ommyoji and A. Yamaguchi, *Taikabutsu*, 58 [3] 160 (2006).
 - 9) G. w. Wen and X. x. Huang, *J. Eur. Ceram. Soc.*, 26 [7] 1281-1286 (2006).
 - 10) Y. Hoshiyama, J. Ommyoji and A. Yamaguchi, *Proc. UNITECR '07*, (2007) pp. 278-281.
 - 11) J. Zhao, W. Lin, A. Yamaguchi J. Ommyoji and J. Sun, *J. Ceram. Soc. Japan*, 115 [11] 761-766 (2007).
 - 12) Y. Hoshiyama, J. Ommyoji and A. Yamaguchi, *Taikabutsu*, 60 [3] 130 (2008).
 - 13) J. S. Lee, S. H. Lee, T. Nishimura and H. Tanaka, *J. Ceram. Soc. Japan*, 116 [6] 717-721 (2008).
 - 14) M. W. Chase, *NIST-JANAF Thermo-chemical Tables*, 4th ed. National Institute of Standards and Technology (1998).
 - 15) H. Yokokawa, M. Fujishige, S. Ujiie and M. Dokiya, *Metallurgical Transactions B*, 18B 433-444 (1987).
-
- Translated from *Taikabutsu* 61 [6] 290-294 (2009)

Paper

High-temperature Reaction of Al_4SiC_4 Coexisting with Carbon

Yasuhiro HOSHIYAMA, Akira YAMAGUCHI and Junji OMMYOJI

Abstract

Al_4SiC_4 -C specimens heated in carbon powder were studied in order to clarify the high temperature reaction mechanism of Al_4SiC_4 added to carbon-containing refractories. Al_4SiC_4 reacted with CO gas to form mainly $\alpha\text{-Al}_2\text{O}_3$ and SiC above 1000°C . This reaction proceeded at lower temperature as the particle size of Al_4SiC_4 addition was decreased. Al_4C_3 did not form at any particle size and heating temperature. A reaction layer about $15\text{ }\mu\text{m}$ thick was formed at the surface of Al_4SiC_4 particles heated at 1500°C for 5 hours. This indicated that the reaction occurred from the surface toward the inside of Al_4SiC_4 particles. The thickness of the reaction layer was constant at all Al_4SiC_4 particle sizes subjected to the same heating conditions. As a result, the reaction was accelerated as Al_4SiC_4 particle size decreased because smaller particles had larger surface area. The reaction layer was composed of SiC and carbon. It was estimated that aluminum vaporized from Al_4SiC_4 and dispersed to the surrounding texture, and then Al_2O_3 and carbon were condensed in the pore and consequently densification of the texture occurred.

Key words: Carbon-containing refractories, Al_4SiC_4 , Reaction mechanism, Reaction layer, Evaporation-condensation

1. Introduction

Characteristics of carbon-containing refractories show extreme variability with different additive substances such as metals and carbides that are introduced to prevent oxidation of carbon and increase the strength. Therefore it is very important to select the most suitable nonoxide system additives according to the service conditions. Recently, various complex-carbides belonging to the Al-Si-C system have been actively studied and are starting to garner attention as new materials for nonoxide system additives¹⁾⁻⁸⁾. These include compounds with various chemical compositions such as Al_4SiC_4 , $\text{Al}_4\text{Si}_2\text{C}_5$, $\text{Al}_4\text{Si}_4\text{C}_7$, $\text{Al}_4\text{Si}_3\text{C}_6$ and Al_5SiC_7 in the Al-Si-C system. However, among them Al_4SiC_4 is evaluated to be the most promising raw material for refractories because it has many excellent characteristics. It is stable in a wide range of service temperatures, has a comparatively high melting point of 2080°C ⁹⁾, has superior hydration resistance and the oxidized coating layer has superior heat-resistance because the mineral composition of the oxidization product is mullite and corundum¹⁰⁾⁻¹²⁾. According to past researches by the authors, in the case of adding Al_4SiC_4 to MgO-C system refractories or to Al_2O_3 -C system refractories, it has been proved that the apparent porosity at elevated temperature is reduced to a large degree and the densification effect is larger than with the addition of either aluminum metal or silicon carbide^{13), 14)}. This paper introduces the results of investigations that were carried out on the reaction behavior of Al_4SiC_4 during the heating process and the changes in mineral compositions. Specimens of Al_4SiC_4 -C system material were prepared by combining Al_4SiC_4 and graphite as the first step to clarify the reaction mechanism of Al_4SiC_4 in carbon-containing refractories at elevated temperatures.

2. Experimental Procedure

2.1 Preparing Al_4SiC_4

Powdered Al_4SiC_4 was produced by the following procedure: a mixture of metal aluminum powder (99%, minus $63\text{ }\mu\text{m}$), metal silicon powder (98%, minus $45\text{ }\mu\text{m}$) and carbon black (60 nm) was mixed at the theoretical composition and blended for 10 hours in a high purity alumina dry ball mill. The blended mixture was sintered at 1700°C for 3 hours in a graphite crucible under Argon gas atmosphere. The sintered material was once again crushed in the dry ball mill for 10 hours into a pulverized powder less than $20\text{ }\mu\text{m}$ (mean diameter about $8\text{ }\mu\text{m}$) that was used as the raw material for the specimens. In a second preparation method the blended powdered material was sintered by Spark Plasma Sintering (SPS) to get a dense body that was a polycrystalline substance with 3 to $15\text{ }\mu\text{m}$ or so crystal diameter. This product was then crushed and screened with standard sieve size control to obtain two kinds of Al_4SiC_4 particles with medium particle size (0.3 to 0.8 mm in diameter) and fine grain size ($45\text{ }\mu\text{m}$ to 0.3 mm in diameter) to provide granular raw material for specimens. In addition, and the crystal phases of both the pulverized powder and particles was identified as single-phase of Al_4SiC_4 by powder X-ray diffraction.

2.2 Manufacturing Al_4SiC_4 -C System Specimens

Al_4SiC_4 -C system specimens were manufactured by combining different particle sizes of Al_4SiC_4 with flaky graphite powder (99%, minus 150 nm). The flaky graphite is generally used as a raw material for carbon-containing refractories and therefore it was also adopted for this study. The blended compositions of the Al_4SiC_4 -C system specimens are shown in Table 1. The granularity of Al_4SiC_4 in the specimens was three kinds: medium particle (0.3 to 0.8 mm in diameter), fine grain ($45\text{ }\mu\text{m}$ to 0.3 mm in diameter) and fine powder (minus $20\text{ }\mu\text{m}$ in

Table 1 Composition of Al_4SiC_4 -C samples (mass%)

	No.	1	2	3
Flake graphite - 150 μm		70	70	70
Al_4SiC_4	0.3 - 0.8 mm	30	-	-
	45 μm - 0.3 mm	-	30	-
	- 20 μm	-	-	30
Phenol resin (Novolac)		ex.5	ex.5	ex.5
Hexamethylenetetramine		ex.0.5	ex.0.5	ex.0.5

diameter) indicated as No.1, No.2 and No.3 respectively. Al_4SiC_4 and flaky graphite with added phenolic resin as a binder were kneaded and the mixture was formed in a mold under a pressure of 98 MPa. After forming it was heat-treated at 200°C for 6 hours to prepare the specimen for testing.

2.3 Heating and Measuring

The Al_4SiC_4 -C system specimens were heated in graphite powder as illustrated in Fig. 1, to reproduce the atmosphere of the field furnace service conditions of carbon-containing refractories. The heating conditions were heating at a rate of 10°C/min, holding at the prescribed temperature for 3 hours and then allowed to cool. After heating, changes in mineral phases in the specimens were investigated by powder X-ray diffractometry. Also, specimens were cut and polished and examined by SEM and EPMA to observe changes due to reaction in the vicinity of Al_4SiC_4 particles.

3. Results

The phenolic resin binder is pyrolytically decomposed and changed into the carbide as the heating temperature increases and consequently the weight of the specimen initially decreases. However, the pyrolysis reaction is essentially complete at about 800°C¹⁵⁾. Therefore it is possible to conclude that the weight decrease occurring above this temperature reflects the effects of reactions in the interior of the specimens. Accordingly in this paper the weight of the specimen after heating at 800°C was used as a benchmark for the experiment. Figure 2 shows the percent weight increase for heating above 800°C. As seen in Fig. 2, the weight increased at temperatures higher than 1000 to

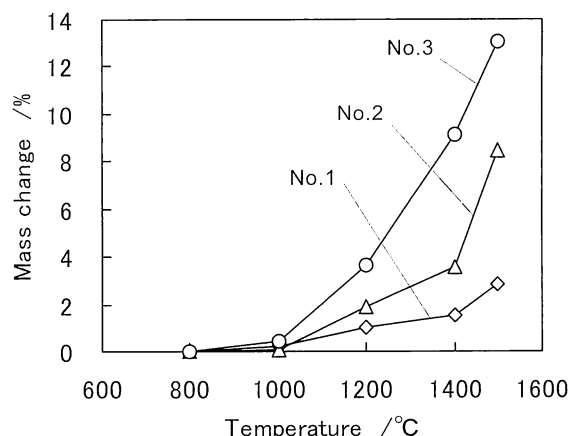


Fig. 2 Mass change of Al_4SiC_4 -C samples with heating.

1200°C in all the specimens and therefore it was possible to conclude that the reactions accompanying the weight increase were making steady progress within the specimens. Also, because the weight increase was significantly larger as the size of the Al_4SiC_4 particles decreased in the order of No.1 (medium particle), No.2 (fine grain) and No.3 (fine powder), it was possible to understand that the smaller the Al_4SiC_4 particle diameter the faster the reaction.

A graphic representation of the mineral phase changes of each specimen is shown in Figs. 3 to 5 for specimens No.1 to 3 respectively. In order to emphasize the changes in the reaction of Al_4SiC_4 , the peaks for graphite were omitted in the graphs. In No.1 specimen (see Figure 3) with medium particle size Al_4SiC_4 0.3 to 0.8 mm in diameter, there was little or no weight increase observed up to 1400°C and the formation of a little $\alpha\text{-Al}_2\text{O}_3$ and SiC were finally observed at 1500°C.

On the other hand, in No.2 specimen (see Figure 4) with fine grain Al_4SiC_4 45 μm to 0.3 mm in diameter, the formation of $\alpha\text{-Al}_2\text{O}_3$ and SiC began at 1200°C or so, and with an elevation of temperature to 1400°C and 1500°C, the quantities of $\alpha\text{-Al}_2\text{O}_3$ and SiC increased accompanied with a decrease in Al_4SiC_4 . In addition, the formation of a slight amount of ALON ($\text{Al}_3\text{O}_3\text{N}_7$) was also observed.

In No.3 specimen (see Figure 5) with fine Al_4SiC_4 powder minus 20 μm in diameter, it was observed that the formation of

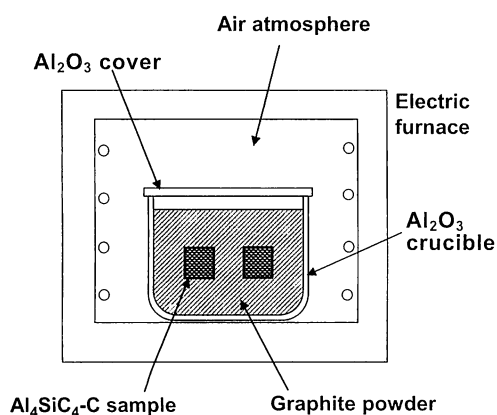


Fig. 1 Outline of heating test.

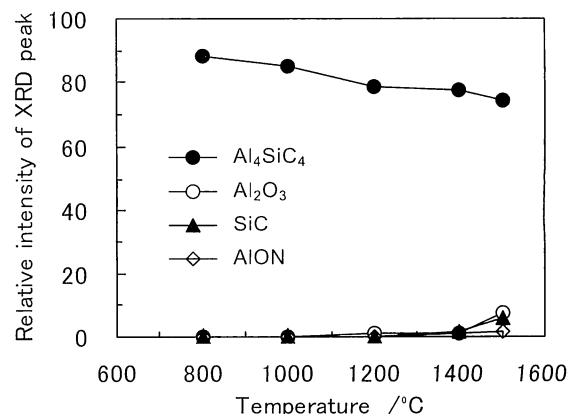


Fig. 3 Mineral phase change of No.1 Al_4SiC_4 -C sample after heating.

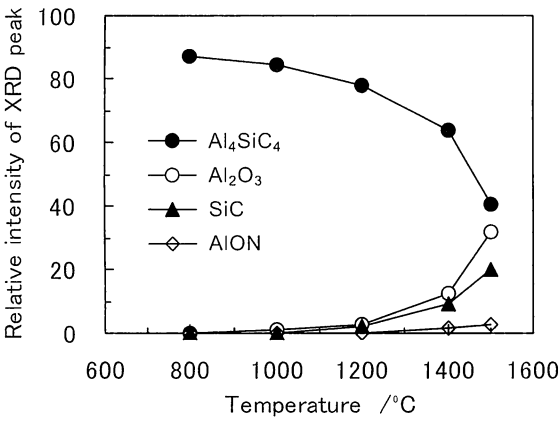


Fig. 4 Mineral phase change of No.2 Al_4SiC_4 -C sample after heating.

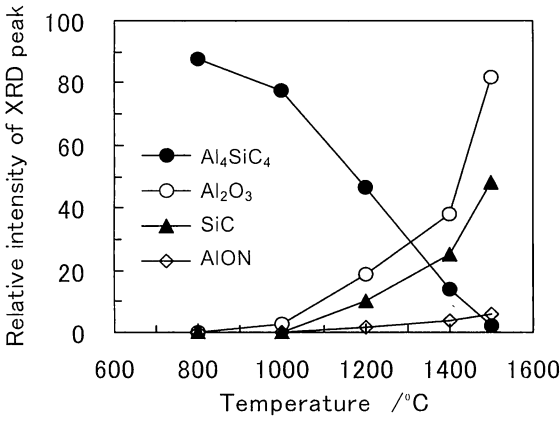


Fig. 5 Mineral phase change of No.3 Al_4SiC_4 -C sample after heating.

α Al_2O_3 and SiC began as early as 1000°C and the quantities significantly increased with increasing heating temperature. Accompanying the increase in formation quantities of α Al_2O_3 and SiC , the volume of Al_4SiC_4 drastically decreased so that nearly all the Al_4SiC_4 was gone at 1500°C . In this case the formation of a slight amount of ALON ($\text{Al}_3\text{O}_3\text{N}_7$) was also observed.

It is possible to understand from these phenomena that Al_4SiC_4 heated in carbon reacts due to reductive sintering and mainly forms α Al_2O_3 and SiC . And it is possible to understand that the reaction rate depends on the granularity of Al_4SiC_4 , and as the particle size becomes smaller the reaction begins at a lower temperature. In addition, no formation of Al_4C_3 was observed in any particle size at any temperature.

Figures 6 and 7 are optical microscopic images of cut specimens illustrating the microstructure of specimens No.1 and No.2 after reductive sintering. The cross-section of the sintered test pieces were prepared for observation by vacuum impregnation with epoxy resin and polishing to a mirror finish. In these figures the light areas are Al_4SiC_4 particles and the grayish areas with elongated texture are flaky graphite. In both specimens No.1 and No.2 phase-changes in the Al_4SiC_4 particles were scarcely observed at 1000 and 1200°C . However, at 1400°C a thin dark layer believed to be a reaction layer appeared on the surface of the Al_4SiC_4 particles. At 1500°C the thickness of the

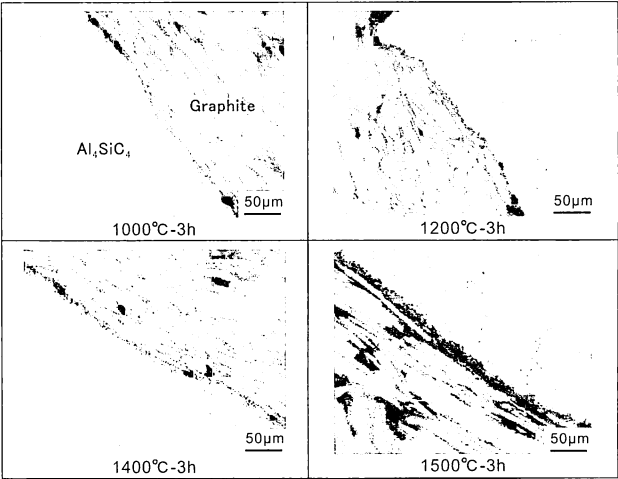


Fig. 6 Microstructure of No.1 Al_4SiC_4 -C sample after heating.

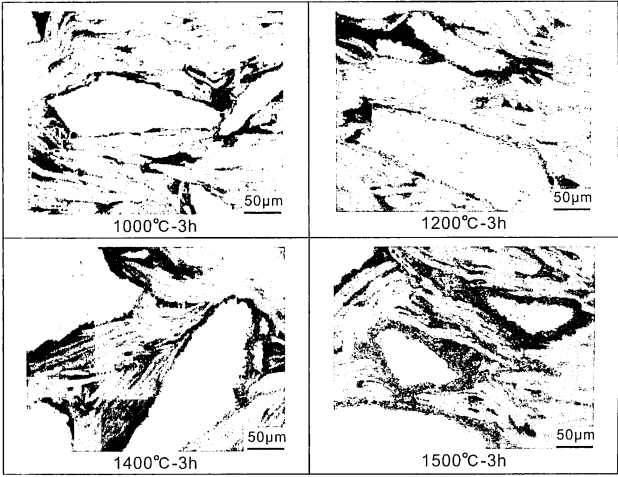


Fig. 7 Microstructure of No.2 Al_4SiC_4 -C sample after heating.

reaction layer increased rapidly and the reaction layers could be clearly identified. In the internal part of the Al_4SiC_4 particles there was no phase-change at any of the sintering temperatures and the body maintained a dense texture. These phenomena establish that the phase-change reaction progresses from the surface of particles toward the interior. The thickness of the reaction layer at 1500°C was about 10 to $20\ \mu\text{m}$ and was relatively uniform regardless of the location. In addition there was no difference in layer thickness between specimens No.1 and No.2. Therefore it is possible to conclude that the difference in the quantity of reaction with particle size illustrated in Figs. 2 to 5 is wholly attributable to the difference of the surface area of the particles, namely the difference of the reaction area. It became clarified, judging from the above-mentioned results, that the reaction of Al_4SiC_4 with carbon material progressed from the surface toward the interior of the Al_4SiC_4 , particle promoting the formation of a reaction layer with an even thickness.

Next, observation and measurement of the elemental analysis were carried with an electron microscope on the same position of the polished section of specimen No.2 after heating at 1500°C . The results are shown in Fig. 8. The SEM secondary electron image shows surface texture in the observation area. The Al_4SiC_4

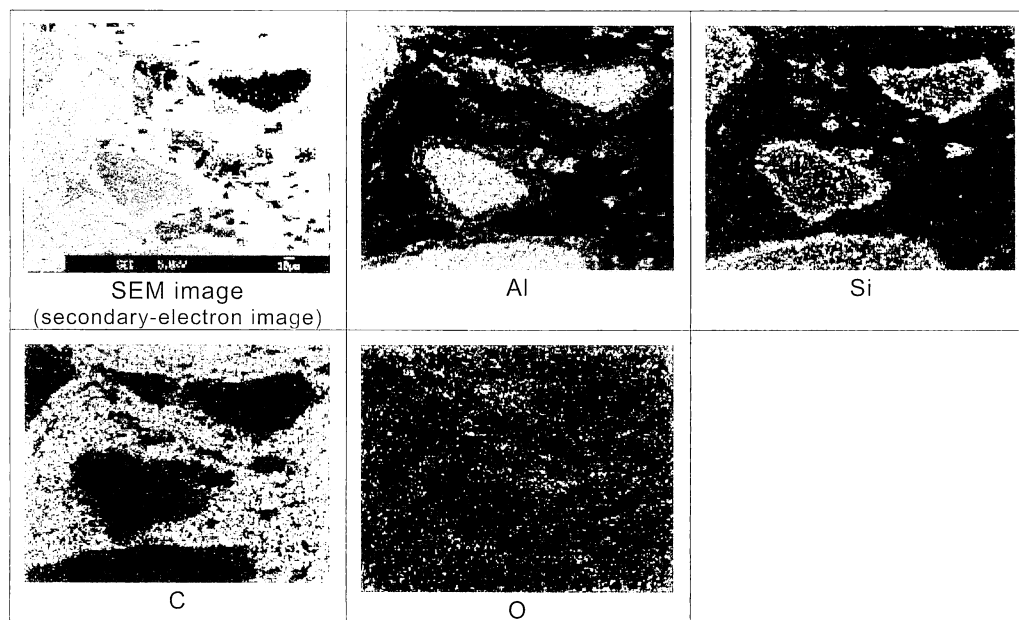


Fig. 8 EPMA images of No.2 Al_4SiC_4 -C sample after heating at 1500°C.

particles appear grayish and it is possible to understand that the cut sections of the particles are flat. On the other hand, the reaction layers on the exterior surface of the particles, shown here in section as a thin line around the particle, appear bright and therefore it is possible to presume that these areas are slightly irregular, namely the reaction layers consist of fine particles. Looking at the distribution of the elements, it is apparent that less Aluminum exists in the reaction layer than within the Al_4SiC_4 particles and the concentration of Silicon is higher. Also, it appears that the carbon concentration is higher in the reaction layer than within Al_4SiC_4 particle.

Figure 9 shows a close-up picture in the vicinity of the reaction layer of the No.2 Al_4SiC_4 -C specimen after heating at 1500°C. The reaction layers consist of a lot of fine particles less than 1 μm in size and show clear signs of a fairly dense texture. The interface surfaces between the reaction layer and Al_4SiC_4 particle are not flat but irregular and are in close contact with

each other. Furthermore the reaction layers also appear to be in tight and firm contact with the flaky graphite. Figure 10 shows the elementary distribution (EPMA images) at this position. It was possible to recognize clearly that there was a decrease in aluminum and an increase in silicon in the reaction layer relative to Al_4SiC_4 particle. Looking at the carbon distribution, it was possible to understand that carbon exists more in the reaction layer rather than within Al_4SiC_4 particle and therefore this trend is the same as that shown in Fig. 8. As shown in Fig. 4, it is possible to make judgments that a large amount of silicon and carbon existing in the reaction layer may exist as silicon carbide (SiC), because the amount of SiC increases as the reaction progresses.

Looking at the distribution of aluminum more closely, it is possible to observe that there is a slightly higher concentration of aluminum at the interface between the reaction layer and graphite layer and at the same position the oxygen concentration is also higher than at other locations. Also, there is a region at a position in the graphite slightly distant from the interface in which the aluminum concentration is somewhat higher than in the graphite particles. In order to clarify these distribution phenomena, EPMA line analysis was carried out on the pertinent position in the same specimen. The results are shown in Fig. 11. It was recognized that there was a position with coexisting Al and O existing on the surface of the reaction layer and also it was recognized clearly that a position with coexisting Al and O was present between graphite particles (shown by arrowheads in the figure). This phenomenon expressly suggests that during progress of the reaction Al components travelled far ahead of the reaction layer into the graphite particles to form Al_2O_3 .

It became clear from the above-mentioned results that a reaction layer with concentrated silicon and carbon formed on the surface of Al_4SiC_4 particles during sintering within carbon powder and that the Al component travelled into the graphite from the surface of the Al_4SiC_4 particles. In the following section

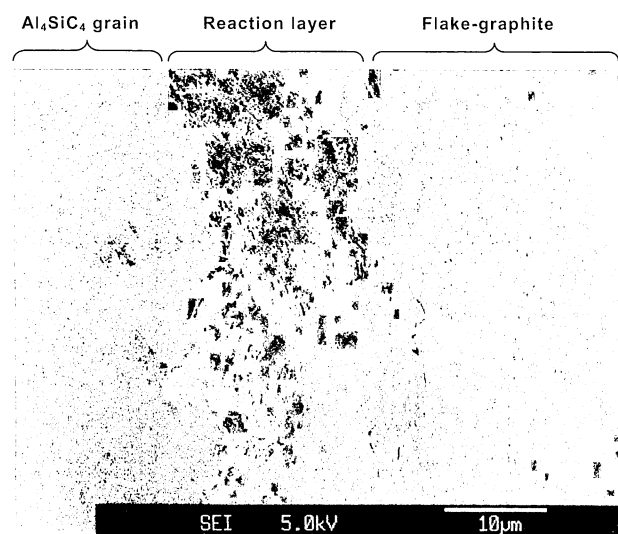


Fig. 9 SEM image of No.2 Al_4SiC_4 -C sample after heating at 1500°C.

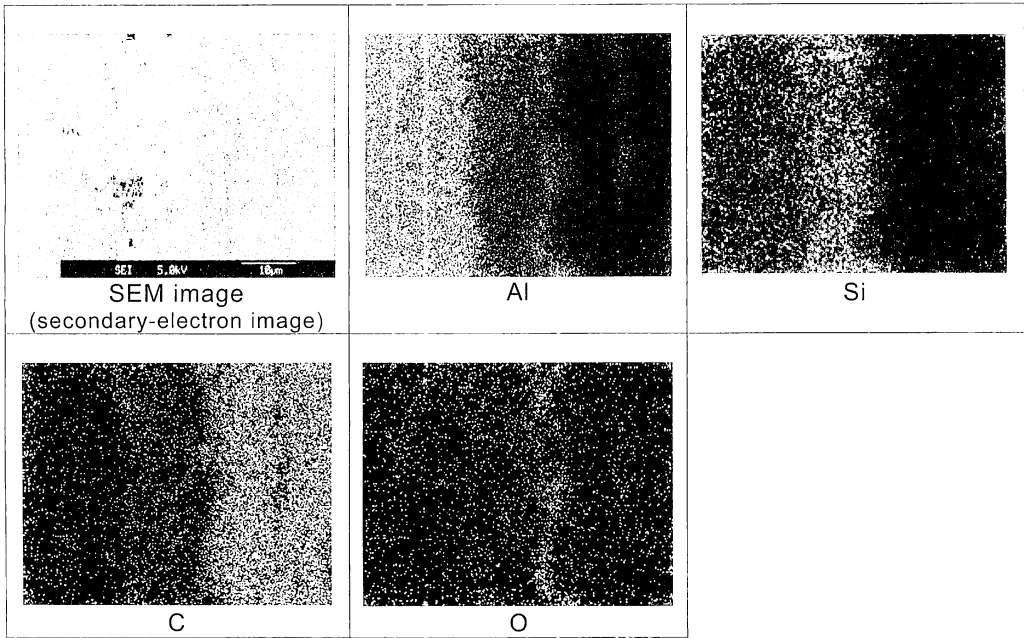


Fig. 10 EPMA images of No.2 Al_4SiC_4 -C sample after heating at 1500°C.

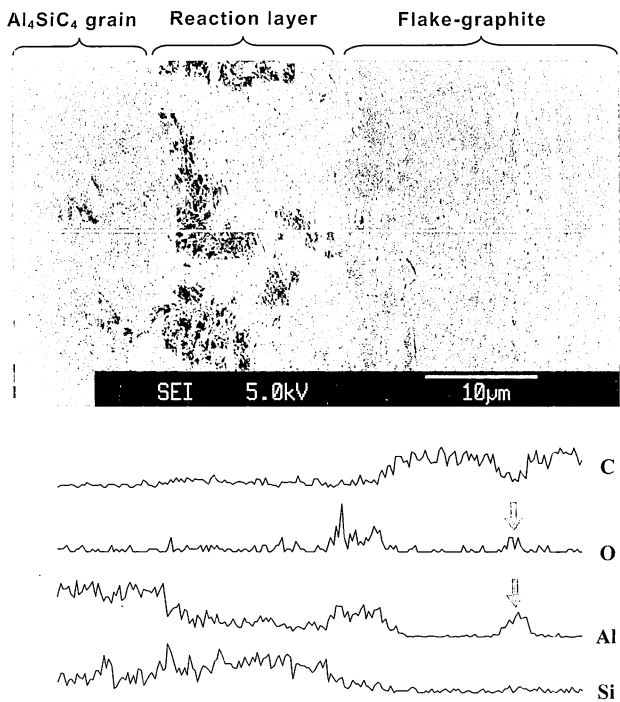


Fig. 11 EPMA line analysis of No.2 Al_4SiC_4 -C sample after heating at 1500°C.

detail discussions are presented on the formation of the reaction layer and the mechanism of aluminum migration.

4. Discussion

In thinking of the reaction of metal carbide in carbon-containing refractories, the gas phase filling the pores of the refractories becomes the most important consideration. As the field furnaces are generally used in the condition of an open air system, the surfaces of the refractories are open to air atmosphere. In this case, in the high temperature range more

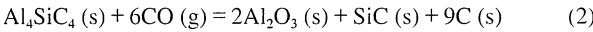
than 1000°C, the interior of the carbon-containing refractories is infiltrated by CO and N₂ gas, and therefore the metal carbide is mainly exposed to reaction with CO gas^{16), 17)}.

In this case the partial pressure of CO gas in the refractories can be quantified as $P_{\text{CO}} = 1.013 \times (2 \times 0.21) / (0.79 + 2 \times 0.21) = 0.35 \times 10^5 \text{ Pa}$ on the assumptions that O₂ gas in the atmosphere changes into CO gas according to Eq. (1) below, the total pressure is kept as $1.013 \times 10^5 \text{ Pa}$ and the composition of air is N₂ = 79% and O₂ = 21% ,



The sintering reaction in this research was under the same conditions as these assumptions, and therefore it is possible to presume that the environment of the periphery and interior of the specimen buried into the graphite powder is fairly close to the CO partial pressure of a substance coexisting with carbon, namely $0.35 \times 10^5 \text{ Pa}$. In addition, as shown in Figs. 3 to 5 a small amount of AlON was recognized as a product of reaction with N₂ gas. However, the amount formed due to such a reaction was so small that all the reactions with N₂ gas are omitted in the following to simplify the discussion.

At first glance, the crystal phase changes shown in Figs. 3 to 5 indicate a decrease in the quantities of Al_4SiC_4 with increasing sintering temperature and the generation of Al_2O_3 and SiC. The reaction can be expressed as Eq. (2) with the additional generation of C (s) at the same time.

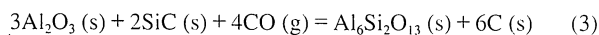


Because this reaction plays the role to entrain CO gas and to establish the solid phases (oxide and carbon), it is possible to think that the weight of the system increases according to the progress of the reaction and this is in good agreement with the results of Fig. 2.

On the other hand, as shown in Figs. 8, 10 and 11, within

the reaction layer formed on the surface of Al_4SiC_4 particles, the concentration of Al decreased and that of Si and C increased. Therefore, it is possible to think that the Al component travelled from the surface of the Al_4SiC_4 particle toward the periphery. As a consequence it is possible to conclude that the reaction of Eq. (2) is making progress accompanied with coincidental migration these elements.

The phenomenon that the Al component travels to a region away from the Al_4SiC_4 particle can be understood by an evaporation-condensation reaction. In the following, the authors will consider the phenomenon of Aluminum migration in conformity to the thermodynamic data. First, by looking for the relation between temperature and the stable condensed phases coexisting with carbon in the Al-Si-C system using the JANAF tables and values from previous literature¹⁸⁾, one is able to obtain Fig. 12. The ordinate axis expresses the normalized dimensionless partial pressure obtained by dividing the partial pressure of CO by the standard state pressure of 0.1 MPa (shown as P^0). In the following discussion the normalized dimensionless partial pressure will be simply referred to as the partial pressure. Figure 12 shows the stability domains of condensed phases in the Al-Si-C-O system as a function of temperature and partial CO gas pressure. When the actual partial pressure of CO gas is at 0.035 MPa, the dashed line in Fig. 12 is at $\log(0.35) = -0.46$. The mixture of $\text{Al}_6\text{Si}_2\text{O}_{13}$ (mullite) + Al_2O_3 + C is the most stable at temperatures less than 1470°C (left side from “a” point). In the case of the range between 1470 to 1890°C (between points “a” and “b”) the mixture Al_2O_3 + SiC + C is the most stable. Consequently it is possible to understand the migration of Al_4SiC_4 phase toward these stable condensed phases in the present sintering experiments that were in the temperature range less than 1500°C. The whole reaction formula in this case can be expressed in Eq. (2) and Eq. (3). In the case of sintering at less than 1470°C, reaction by Eq. (2) occurs first and is then succeeded by the reaction of Eq. (3). It follows that only reaction by Eq. (2) progresses in the range between 1470 and 1890°C.



For example, as shown in Fig. 12, at 1400°C as long as the Al_4SiC_4 phase exists, in other words during the reaction of Eq. (2), the CO gas partial pressure in the vicinity of the Al_4SiC_4 phase maintains at approximately $10^{-3.3}$ and therefore the SiC

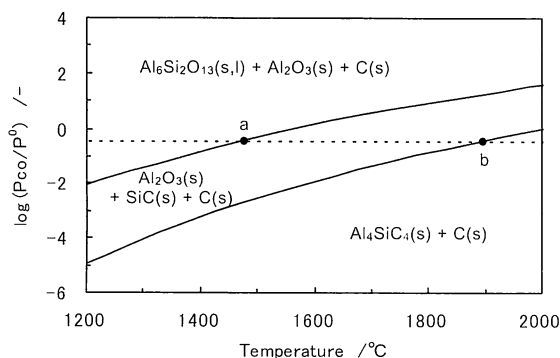


Fig. 12 Stability domains of the condensed phases in the Al-Si-C-O system.

phase coexists stably. Then, in the case of elimination of the Al_4SiC_4 phase, the CO gas partial pressure rises to $10^{-0.9}$ and it follows that only reaction by Eq. (3) progresses. Also, taking another example, in the case of 1500°C, as long as Al_4SiC_4 phase exists, the CO gas partial pressure in the vicinity of Al_4SiC_4 phase maintains at approximately $10^{-2.6}$ and therefore SiC phase coexists stably. Then, in the case of elimination of the Al_4SiC_4 phase, the CO gas partial vapor pressure rises to $10^{-0.46}$ ($P_{\text{CO}}/P^0 = 0.35$, $P_{\text{CO}} = 0.35$ MPa) and it follows that SiC exists as a stable condensed phase. In addition, as evidenced by Fig. 12, because Al_4C_3 does not exist as a stable phase, it is possible to understand from the thermodynamic data that the formation of Al_4C_3 is impossible in the reaction process and this is consistent with the results of Figs. 3 to 5.

Next, the authors will discuss the equilibrium partial pressure of the various gasses in the Al-Si-C-O system in order to investigate the migration of the Al component under reduction sintering at 1500°C. Because the thermodynamic data are listed in 100 K intervals in the JANAF tables, the authors will discuss this using the values at 1800 K (1527°C) which are the nearest to 1500°C. Figure 13 illustrates the changes in the equilibrium partial vapor pressure (P_i) of various gasses in Al-Si-C-O system at 1800 K obtained from the JANAF tables and values from previous literature¹⁸⁾. As shown in the figure there are various kinds of gas phases and among them the gas phases containing Al, Al (g) and Al_2O (g) show the highest partial pressure in the region of $\log(P_{\text{CO}}/P^0) < 0$. The following discussion considers reactions with particular attention to these two gasses. The equilibrium partial pressures of various gasses are strongly dependent on the CO partial pressure and consequently the partial pressures of Al (g) and Al_2O (g) rise up to the level of $10^{-3.7}$ at the highest point. Therefore it is possible to say that both are at a level to make significant contribution to evaporation even in heating for only a few hours. Figure 13 also shows the

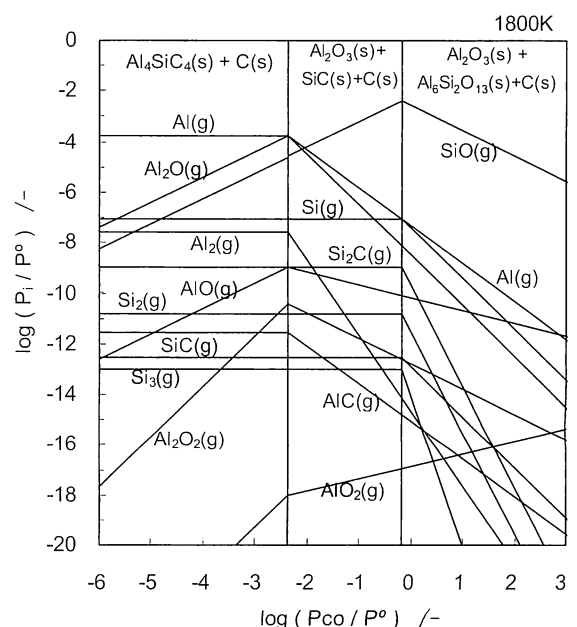
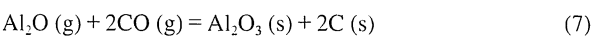
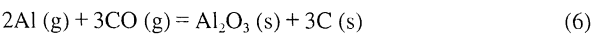
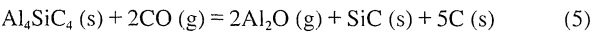
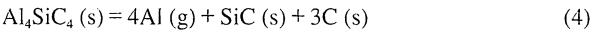


Fig. 13 Equilibrium partial pressures of the gases in the Al-Si-C-O system.

stable condensed phases with different CO partial pressures and consequently it is possible to understand that when CO partial pressure is at $10^{-2.4}$, $\text{Al}_4\text{SiC}_4(\text{s})$ can coexist stably together with $\text{Al}_2\text{O}_3(\text{s})$ and $\text{SiC}(\text{s})$. Therefore during reaction by Eq. (2) the CO partial pressure is maintained approximately at $10^{-2.4}$ in the vicinity of the Al_4SiC_4 phase. It follows under this condition that the partial pressure of Al (g) and Al_2O (g) rise up to $10^{-3.7}$ and vaporization of Al components occurs from the Al_4SiC_4 phase. The reaction formulas at that time are represented as Equations (4) and (5). Silicon carbide and carbon are left behind in the traces of aluminum vaporization. Both Al (g) and Al_2O (g) diffuse throughout the periphery of the Al_4SiC_4 phase, but on the other hand the region distant from the Al_4SiC_4 is a location with just as high partial pressure of CO gas. On the occasion when Al (g) and Al_2O (g) migrate to a place where the CO partial pressure is higher than $10^{-2.4}$, it is clear from Fig. 13 that the equilibrium partial pressures of these gases fall and it follows as the result that they condense as Al_2O_3 and carbon according to Equations (6) and (7). This vaporization-condensation reaction is thought to occur continually in the vicinity of Al_4SiC_4 particles and therefore it is possible to presume that Al_4SiC_4 particles gradually are converted to SiC and carbon. In addition, the combined entire reaction formula of Equations (4) and (6) or (5) and (7) becomes Equation (2).



Summarizing the above discussion, the reaction in the vicinity of the surface of Al_4SiC_4 particles within carbon powder at 1500°C can be modeled as illustrated in Fig. 14. Aluminum-containing gaseous phases like Al (g) and Al_2O (g) are generated because the CO partial pressure is low, less than 10^{-2} , on the surface of Al_4SiC_4 particles. The generated gaseous phases are dispersed toward the periphery texture by diffusion and they condense as Al_2O_3 (s) and C (s) because of the decrease in the equilibrium partial pressure when migrating up to the location of higher CO partial vapor pressure. On the other hand, on the surface of Al_4SiC_4 particles the layer consisting of SiC (s) and C (s) is formed as the residual after evaporating aluminum. As the

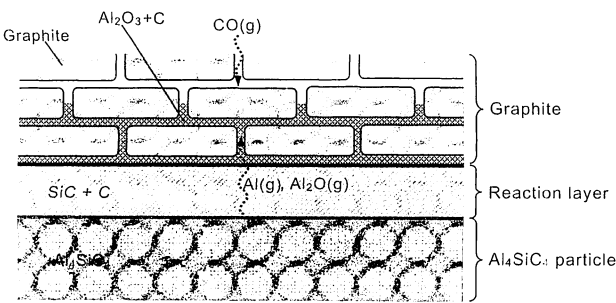


Fig. 14 Reaction model of Al_4SiC_4 grain in the carbon.

result it is possible to conclude that by continuous progress in the evaporation condensation reaction of the Al-component, the reaction layer on the surface of Al_4SiC_4 particles gradually increases in thickness and void portions of the periphery graphite texture are gradually filled up with Al_2O_3 and C.

It is possible to postulate that in the case of heating carbon-containing refractories containing added Al_4SiC_4 particles, the void portions are filled up with Al_2O_3 and C due to evaporation condensation of Al-component, and therefore the phenomenon produces improvements such as higher density texture, and lower apparent porosity that result in increased mechanical strength and decreased pore diameter^{13), 14)}. Also, as mentioned previously, it is possible to think that because Al_4SiC_4 particles do not generate Al_4C_3 in the reaction process, there is no need for apprehensions regarding texture breakdown from the slaking of Al_4C_3 . It is possible to conclude judging from these various advantages that Al_4SiC_4 is a very beneficial material as reinforcement for texture that is able to fill up the voids in carbon-containing refractories with alumina and carbon.

5. Conclusions

To clarify the reaction mechanism of Al_4SiC_4 particles in carbon-containing refractories at elevated temperature, Al_4SiC_4 -C system specimens were prepared that combined different size Al_4SiC_4 particles with graphite. The specimens were sintered at various temperatures and analyzed. As the result, the following knowledge was obtained:

- (1) Al_4SiC_4 particles in graphite start to react at temperatures higher than 1000°C and form mainly $\alpha\text{-Al}_2\text{O}_3$ and SiC. The degree of reaction varies according to the particle size: the smaller the Al_4SiC_4 particle size the lower the temperature at which the reaction starts and the greater the degree of reaction at every temperature. The formation of Al_4C_3 was not observed at any particle sizes and heating temperature,
- (2) On the occasion when Al_4SiC_4 -C system specimens were sintered at 1500°C for 3 hours, a reaction layer 10 to $20\text{ }\mu\text{m}$ thick was formed on the surface of the Al_4SiC_4 particles and the interior of the particles remained as a dense texture: It is possible to conclude that the reaction progresses from the surface to the interior of the particles.
- (3) For a given heating condition the thickness of the reaction layer formed on the surface of Al_4SiC_4 particles remained constant regardless of the Al_4SiC_4 particle size. It is possible to conclude therefore that the reason why the reaction apparently progresses faster in smaller particles is because of the larger reaction surface area.
- (4) The reaction layer mainly consists of SiC and C. The Al-component evaporates and diffuses as Al (g) and Al_2O (g), and these gasses migrate into voids in the periphery texture, react with CO gas within the voids and condense as Al_2O_3 and C resulting in densification of the texture.

References

- 1) A.Yamaguchi and S. Zhang; J. Ceram. Soc. Japan. 103 [1] pp20-24 (1995)
- 2) K. Inoue, S. Mori and A. Yamaguchi; J. Ceram. Soc. Japan. 111 [2] pp126-132 (2003)
- 3) K. Inoue, S. Mori and A. Yamaguchi; J. Ceram. Soc. Japan. 111 [5] pp348-351 (2003)
- 4) Wills Roger and Goodrich Steve; Ceram. Eng. Sci. Proc., 26 [3] pp181-188 (2005)
- 5) Wen G. w. and Huang X.x.; J. Eur. Ceram. Soc., 26 [7] pp1281-1286 (2006)
- 6) Lee Jin-seok, Lee Sea-hoon, Nishimura Toshiyuki and Tanaka Hidehiko; J. Ceram. Soc. Japan. 116 [6] pp717-721 (2008)
- 7) Toshiyuki Nishimura, Lee Jin-seok, Hidehiko Tanaka and Hisanobu Hiroaki; *Taikabutsu*, 61 [3] p138 (2009)
- 8) Hidemine Ohashi, Sinobu Hashimoto, Sawao Honda, Yuhji Iwamoto and Kohji Inoue; Japan Ceram. Soc. Proc.in 2009, pp25 (2009)
- 9) J. Zhao, W. Lin, A. Yamaguchi, J. Ommyouji and J. Sun; I. Ceram. Soc. Japan, 115 [11] pp 761-766 (2007)
- 10) S. Zhang and A. Yamaguchi; J. Ceram. Soc. Japan. 103 [3] pp235-239 (1995)
- 11) S. Zhang, and A.Yamaguchi; Proceedings of UNITECR'97 Vol2 (1997) pp861-869
- 12) Motonari Fujita, Junnji Ommyouji and Akira Yamaguchi; *Taikabutsu*, 59 [3] p160 (2006)
- 13) Yasuhiro Hoshiyama, Junji Ommyouji and Akira Yamaguchi; *Taikabutsu*, 60 [10] p540-548 (2008)
- 14) Yasuhiro Hoshiyama, Junji Ommyouji and Akira Yamaguchi; *Taikabutsu*, 60 [3] p130 (2008)
- 15) Kyouhei Funabiki, Masayuki Nakamura and Masaaki Tsuritani; *Taikabutsu*, 33 [2] p64-80 (1981)
- 16) Akira Yamaguchi; *Taikabutsu*, 35 [7] p365-370 (1983)
- 17) Akira Yamaguchi; *Taikabutsu*, 35 [11] p617-622 (1983)
- 18) H. Yokokawa, M. Fujishige, S. Ujiie and M. Dokiya; Metallurgical Transactions B, 18B pp433-444 (1987)

Translated from *Taikabutsu* 61 [10] 548-555 (2009)

Review

Methods of Thermal Conductivity Measurements for Refractories and Some Problems Accompanying Their Methods

Hideo ASAKURA, Akira YAMAGUCHI and Kunio HAYASHI

1. Introduction

The thermal conductivity of refractories gives rise to temperature gradients within furnace walls and affects furnace bodies in various ways. And it also plays a very important role from an environmental point of view as a characteristic in thermal loss from the furnace walls. Therefore, measurement of thermal conductivity has been carried out by various methods¹⁾. With regard to thermal insulating firebricks, the standard JIS R 2616 (heat flux method) was established in 1954 and JIS R 2618 (hot wire method) in 1979. However, nothing further was done until 2007 with the establishment of a JIS standard for the measurement of thermal conductivity for all classes of refractories²⁾. The authors were requested by TARJ (The Technical Association of Refractories, Japan) to comment on the contents of JIS R 2251 1 to 3 established in 2007 in accordance with the spirit of the title of this paper presented at the Symposium on Environment and Refractories sponsored by TARJ. In this paper the authors intend to introduce the content of the newly established JIS from the viewpoint of measuring technologies for thermal conductivity, to describe the points considered in the measuring technique and further to report some problems requiring some new thought. In addition the authors intend to introduce some new information on the application of the laser flash method to measure thermal conductivity of refractories that is a classic yet new problem from the viewpoint of the measuring technique.

2. Concept of Thermal Conductivity and Major Test Methods (General Considerations)

With regard to the concept of methods to measure thermal conductivity, Hayashi's commentary on "Measuring Equipment for Thermal Diffusivity and Thermal Conductivity"³⁾ is thought to serve as a useful reference and therefore the authors introduce it to carry a quotation from the literature. Figure 1 shows temporal changes in temperature distribution within a parallel flat plate in which surface I of a parallel flat plate with dimensions of thickness L (m) and cross sectional area A (m²) was maintained at a beginning temperature θ_0 (K) and then exposed to temperature θ_2 (K). The changes in the surface temperature and the temperature distribution within the flat plate are illustrated on a conceptual basis as time (t) advances. As clarified from the figure, the temperature within the flat plate moves upward gradually forming a temperature distribution as

shown in the figure due to the heat inflow into the plate. During the initial stages (t_0 to t_4), all the input heat Q_{in} is accumulated within the plate body and therefore the temperature of surface II does not change, remaining as it was at θ_0 . When the elapsed time reaches t_5 , the heat passing through the flat plate arrives at the edge of surface II and the temperature of surface II starts on an upward path, but at the same time the rate of heat accumulation into the body remains the same. The transient state like this is called an unsteady state.

After enough time passes to arrive at t_n , the temperature of surface I becomes equal to the temperature θ_2 (K) of the elevated temperature side, and if the plate is homogeneous and flat, the temperature gradient at every position within the plate becomes constant. Consequently the temperature of surface II becomes constant at θ_1 (K) and this is called a steady state condition. At this time the input heat Q_{in} becomes equal to the output heat Q_{out} .

Whereas, the method to measure the thermal conductivity in the unsteady state is called the transient method, in the steady state it is called the steady method. In the following the authors briefly describe the relations between the elapsed time and the typical test methods of thermal conductivity in accordance with this concept.

2.1 Transient hot wire method

This method utilizes the phenomena occurring during the time interval t_0 to t_4 of the transient shown in Fig. 1.

This is a method to obtain the thermal conductivity in which wires set up on surface I of Fig. 1 are electrically heated and the temperature rise of the specimen during the stage t_0 to t_4 is measured in unsteady state condition. There are two methods in this category: one is termed the cross array system that utilizes a principle where the temperature in the vicinity of the hot wire increases at a rate proportional to the logarithmic value of time ($\log t$), while the other method is termed the parallel array system which measures the temperature rise at a constant distance of 15 mm from the specimen. In the former method, the thermal conductivity is obtained by measuring the temperatures θ_a and θ_b at the times t_a and t_b . The latter method utilizes the theoretical formula of $-E_1 \cdot r^2 \cdot (4\alpha t)^{-1}$ evaluated from the ratio of the rise in temperature $\Delta\theta(2t)/\Delta\theta(t)$ measured at time t and time $2t$ respectively. This latter method has an advantage to be able to obtain the thermal conductivity directly regardless of which unsteady state transient hot wire method is utilized.

Nowadays, both internationally and domestically this latter evaluation method has become a standardized measurement

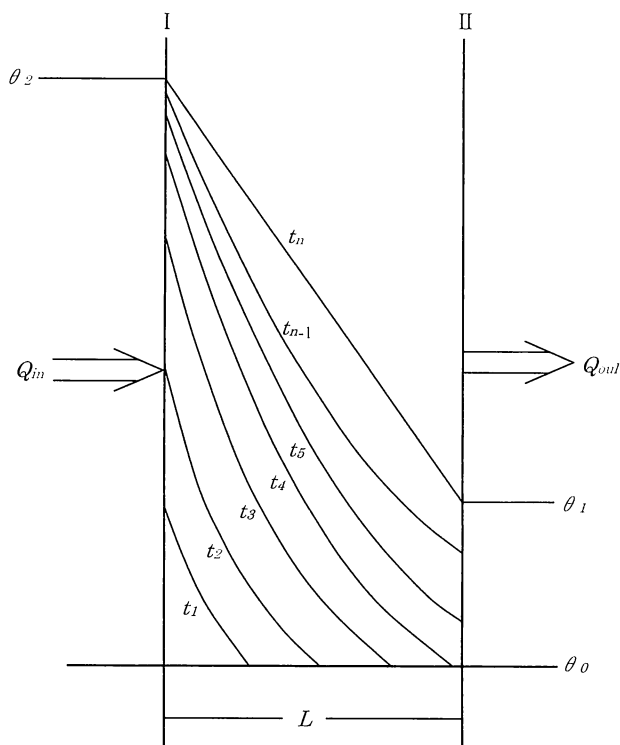


Fig. 1 Temporal changes in temperature distribution within parallel flat plate.

method.

2.2 Transient indirect method

This method utilizes the period from the beginning stage to the time just prior to the thermal equilibrium state, that is, from t_0 to t_{n-1} , in Fig. 1.

The thermal conductivity is obtained by first getting the thermal diffusivity α ($\text{m}^2 \cdot \text{s}^{-1}$) by measuring the thermal diffusion on the surface I and the surface II in the unsteady state, (t_0 to t_{n-1}). The thermal conductivity λ ($\text{W} \cdot \text{m}^{-1} \cdot \text{K}^{-1}$) can then be calculated from the thermal diffusivity, the specific heat capacity c ($\text{J} \cdot \text{kg}^{-1} \cdot \text{K}^{-1}$) and the bulk density ρ ($\text{kg} \cdot \text{m}^{-3}$) using the following relational expression where the units of W are ($\text{J} \cdot \text{s}^{-1}$).

$$\lambda = \alpha \cdot c \cdot \rho \quad (1)$$

There are various heating systems for measurement by the transient indirect method such as: periodic heating, stepwise heating, flash heating and constant temperature increase rate. A laser flash method that come into widespread use recently measures the thermal diffusivity from the temporal change in the temperature increase of surface II during the period from t_5 to t_{n-1} in Fig. 1.

2.3 Steady heat flux method

This method utilizes the completion of thermal equilibrium after time t_n in Fig. 1.

Under the condition of thermal equilibrium the amount of heat Q (W) flowing within the flat plate in unit time is proportional to the cross sectional area A and temperature gradient $(\theta_2 - \theta_1) \cdot L^{-1}$ as shown in Equation (2) below.

$$Q = \lambda \cdot A \cdot \frac{\theta_2 - \theta_1}{L} \quad (2)$$

Because the proportionality constant λ determining the volume of the heat flux is the thermal conductivity itself, Equation (2) can be rewritten as the following:

$$\lambda = \frac{Q \cdot L}{A (\theta_2 - \theta_1)} \quad (3)$$

The thermal conductivity obtained with the help of this principle is related to the value at the average temperature $(\theta_2 - \theta_1)/2$ between the temperature θ_2 of surface I and θ_1 of surface II, in contrast to the unsteady state method that is related to the value at each measured temperature.

3. Test standards of thermal conductivity

The standardization of test methods for thermal conductivity for refractories is making progress in every country and region. Consequently in the International Standards (ISO) and in the European Standards (EN), which are the regional based standards intended for 29 European countries, the relevant provisions have been already specified. Table 1 summarizes a revised list of test standards for the thermal conductivity of refractories specified in the engineering specifications of various countries and regions which was compiled by Hayashi⁴⁾. It is possible to understand, judging from this list, that engineering specifications for the test methods of thermal conductivity for refractories in the world can be consolidated into three methods: the cross array wire method (including single wire method), the parallel hot wire method and the heat flux method.

In addition, standards for fine ceramics are provided in Table 2 for the thermal conductivity, the thermal diffusivity and the specific heat capacity. The characteristic measurement specification to obtain the thermal conductivity of fine ceramics is by calculation using the relational expression of Equation (1) after obtaining the thermal diffusivity by the laser flash method.

In the subsequent chapters the authors will consider two hot wire techniques, the cross array wire-fixing method and the parallel array method, plus the heat flux method as specified in JIS R 2251-1 to 3 and the laser flash method that is applied to fine ceramics. The latter method needs further research in the field of refractories. All four methods and their problems will be discussed.

4. Four test methods for thermal conductivities and their problems

4.1 JIS R 2251-1 Hot wire method (cross array wire-fixing method)

Figure 2 is a schematic drawing of test equipment for the hot wire cross array wire-fixing method (hereafter referred to as cross array method) for refractories. Also, Fig. 3-1 shows the layout of the hot wire and thermocouples in a storage vessel (in the case of inverted V type connection pattern) and Fig. 3-2 is a schematic drawing of a heat resisting specimen storage vessel for powdered and granular bodies. This method was originally

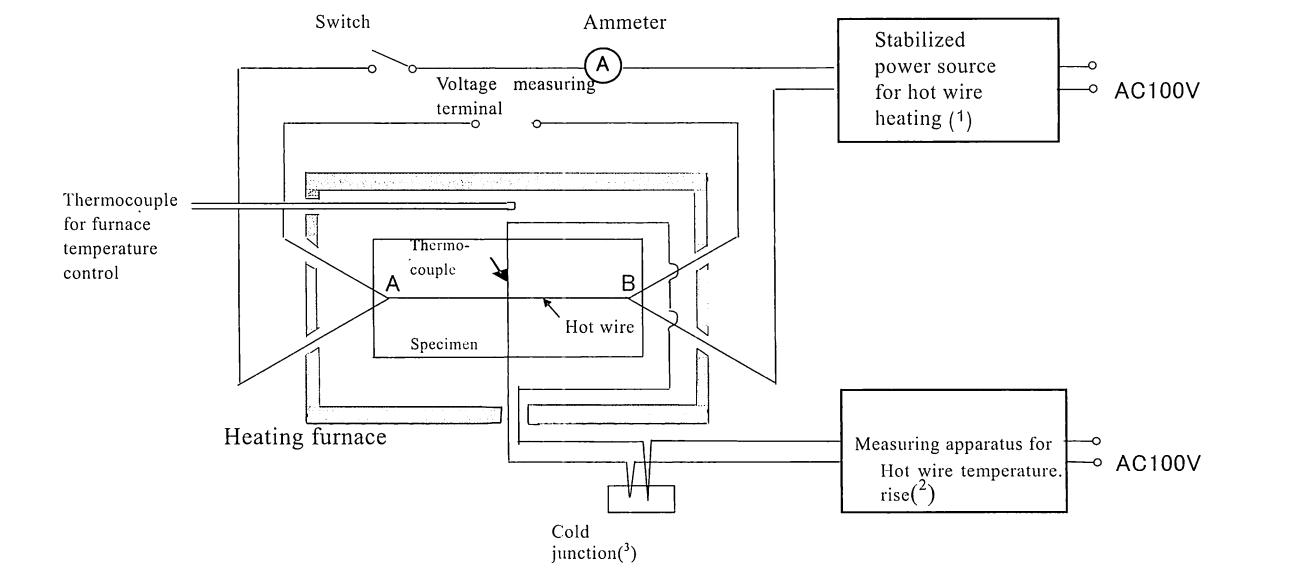
Table 1 Engineering specifications of test method for thermal conductivity in various countries and regions

Nations or Region	Japan			International		EU		U.S.A.		Germany	Australia
Standard	JIS R 2251-1	JIS R 2251-2	JIS R 2251-3	ISO 8894-1	ISO 8894-1	EN 993-14		ASTM C 201	ASTM C 1113	DIN 51046	AS 1774.14
Established year	2007	2007		1987	2007	2007		1993	1999	1979	1966
Application material	Shaped refractories, monolithic, raw materials, powdered and granular bodies, fiber, however electrically conductive material are excluded.	Shaped refractories, monolithic, raw materials, powdered and granular bodies, fiber, however electrically conductive material are excluded.	Refractories, it may use for electrical conductive material	Shaped refractories, monolithic, raw materials, powdered bodies, however electrically conductive material and fiber are excluded.	Shaped refractories, monolithic, raw materials, powdered and granular bodies, however electrically conductive material are excluded.	Shaped refractories, monolithic, raw materials, powdered and granular bodies, however electrically conductive material are excluded.	Shaped refractories, monolithic, raw materials, powdered and granular bodies, however electrically conductive material are excluded.	Refractories, refractory materials	Refractories, castable, ramming mix, powdered and granular bodies, fiber	Refractories, raw materials, powdered and granular bodies	Refractories, refractory materials, powdered and granular bodies, fiber are excluded.
Measurement principle	Hot wire method	Hot wire method	Heat flux method	Hot wire method	Hot wire method	Hot wire method	Hot wire method	Steady method	Hot wire method	Hot wire method	Steady method
Measurement type (wiring)	Cross connection V connection	Parallel array method	-	Cross connection	Parallel array method	Cross connection	Single wire method	Plate process	Single wire method	Cross connection	Plate process
Kind of hot wire	87%Pt-13%Rh Ni/Cr	87%Pt-13%Rh Ni/Cr	-	Pt/Rh Base metal wire	Pt/Rh Base metal wire	Pt/Rh Base metal wire	Pt/Rh Base metal wire	-	Pt	Pt/Rh	K
Temperature measurement method	Thermocouple	Thermocouple	Sheathed thermocouple	Thermocouple	Thermocouple	Thermocouple	Turning current of 100mA on hot wire, converting the changes in electric resistance	Thermocouple	Converting the changes electric resistance in	Thermocouple	Thermocouple
Maximum measured temperature /°C	1250	1250	750	1250	1250	1250	1250	-	1500	1600	Superior surface temperature 1550
Measuring range /W(m·K) ⁻¹	10	25	10 - 60	1.5	25	1.5	15	-	15	2	30
Measuring time	The time region ascertained during $\Delta\theta/10^\circ\text{C}$	65 s - 20 min	-	2 - 10 min	65 - 2500 s	5 - 15 min	5 - 15 min	-	15 min	2 - 10 min	-
Kind of hot wire	R or S Ni/Cr	R or S Ni/Cr	-	Pt/Rh Base metal wire	Pt/Rh Base metal wire	Pt/Rh Base metal wire	Pt/Rh Base metal wire	-	Pt	Pt/Rh	K
Kind of thermocouple	Pt/Rh K	Pt/Rh K	K	Pt/Rh Base metal wire	Pt/Rh Base metal wire	Pt/Rh Base metal wire	Pt/Rh Base metal wire	-	Pt	Pt/Rh	-
Electric supply source	Constant current, constant voltage, constant power	Constant current, constant voltage, constant power	-	Constant power	Constant power	It is recommended DC or AC in constant power, in particular AC is better	AC in constant power of 1 kHz	-	Constant current	Constant voltage	-
Reference								Netsubusei, 6, 89 (1992)		Takahashi, 30, 360, 46 (1978)	

Remarks : ISO 8894-1 was modified the title into Part 1 : Hot wire methods (cross-array and resistance thermometer) and amended on May 15 in 2010, on the other hand in European standard (EN) there is parallel method as 993-15, which acts as a benchmark for ISO 8894-2 2007. In ASTM, on the basis of C 201, each is specified : C 182 (for heat resistant brick), C 202 (for fireclay brick), C 417 (for unburnt monolithic refractories) and C 767 (for carbon block)

Table 2 Standards of thermal conductivity in fine ceramics field

Standard No.	Established	Standard
JIS R 1611	1977	Test methods of thermal diffusivity, specific heat capacity, and thermal conductivity for fine ceramics by laser flash method
JIS R 1650-3	2002	Method for measurement of fine ceramics thermoelectric materials Part 3 : Thermal diffusivity, specific heat capacity, and thermal conductivity
JIS R 1667	2005	Determination of thermal diffusivity of continuous fiber-reinforced ceramic matrix composites by the laser flash method
JIS R 1672	2006	Determination of specific heat of fiber-reinforced ceramic composite by differential scanning calorimetry
ISO 18755	2005	Fine ceramic (advanced ceramics, advanced technical ceramics) – determination of thermal diffusivity of monolithic ceramics by laser flash method



Note⁽¹⁾ It may use either direct or alternate constant current, constant voltage or constant power source, but confines to one without fluctuation more than 2% during measurement.

⁽²⁾ It consists of digital multi-meter possessing of response speed more than 0.5s and resolving power more tha 0.05 μV or 0.01 $^\circ\text{C}$ and personal computer.

⁽³⁾ In caseonf utilizing digirtal multi-meter equipped with temperature indication function complete with internal temperature compensation circuit, this in no nessesary to use the cold junction.

Fig. 2 An example of measuring apparatus for thermal conductivity by cross array method.

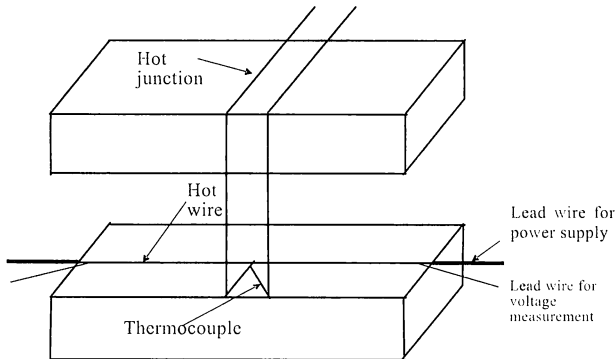


Fig. 3-1 Layout of hot wire and thermocouples in a storage vessel (in case of inverted V type connection pattern).

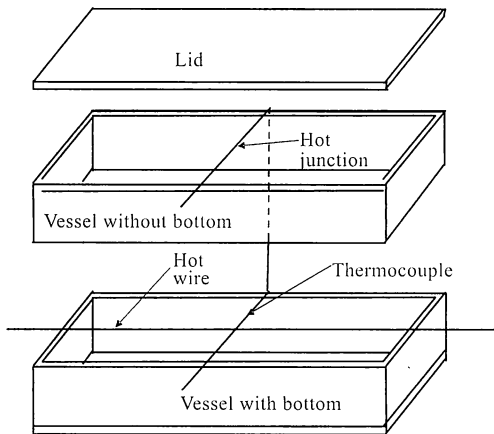


Fig. 3-2 Schematic drawing of specimen storage heat resisting vessel for powdered and granular bodies.

proposed from DIN, but as seen in Table 1, it is in wide use nowadays in all the countries of the world as an ISO, EN and AS standard. In the domestic area, Hayashi et al. brought forward development and improvement in this method early on and it is in widespread use.

Measurement operations are as below:

- 1) The specimen assembly is placed in an electric resistance furnace capable of stable temperature control in the manner shown in Figs. 3-1 and 3-2, where Fig. 3-2 is for the measurement of the thermal conductivity of a packed powder body with a given bulk density.
- 2) Keeping the desired ambient temperature within the electric furnace in the measurement range from room temperature to 1250°C, observe that the ambient temperature variation is less than 0.05°C during 5 min. (A personal computer measuring system is widely used to detect temperature and temperature changes automatically)
- 3) When the temperature becomes stable, a constant electrical current is passed through the hot wire and the temperature rise is measured at a given time interval. (For instance, one second intervals). Table 3 shows the adequate supply power and the maximum measuring time against the thermal conductivity.
- 4) The relations of temperature and measuring time are expressed as a plot of temperature (θ) versus $\log t$ as shown in Fig. 4 measurement example by the OCRF and a continuing straight line domain of $\theta - \log t$ line is searched. A sequence

Table 3 Adequate supply power and maximum measuring time for thermal conductivity

Thermal conductivity/ $\text{W} \cdot \text{m}^{-1} \cdot \text{K}^{-1}$	Maximum measuring time/s	Adequate supply power/ $\text{W} \cdot \text{m}^{-1}$
2	600	50
4	300	100
6	200	120
8	160	125
10	120	150

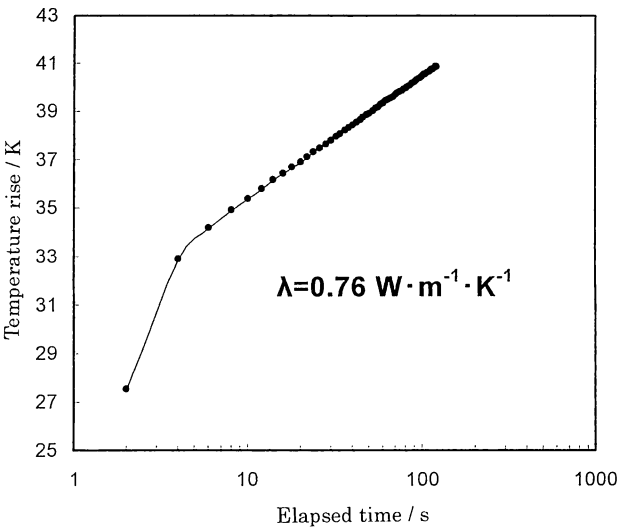


Fig. 4 An example of $\theta - \log t$ line (measured by OCC).

of procedures may be searched using a computer.

- 5) From the straight line domain of the $\theta - \log t$ line, temperature rise θ_a at time t_a and θ_b at time t_b are obtained using the measured values and it is possible to obtain the thermal conductivity λ from the following equation.

$$\lambda_0 = \frac{I^2 R}{4\pi} \times \frac{\ln \frac{t_b}{t_a}}{\theta_b - \theta_a} \quad (4)$$

Where:

- λ_0 : thermal conductivity at the measurement temperature θ
- R : the value of electric resistance of hot wire ($\Omega \cdot \text{m}^{-1}$)
- I : the value of current run through the hot wire (A)

- 6) The data of the measured example by OCRF shown in Fig. 4 were gathered at 2 second intervals. The slope of the $\theta - \log t$ line increased rapidly at the initial stage and after 8 seconds the slope became stable. For example, the relational expression of the $\theta - \log t$ line between 12 seconds and 120 seconds may be expressed by the equation $\theta = 30.353 + 2.194 \times \ln(t)$ and it is possible to calculate $\theta_{12} = 35.8 \text{ K}$ and $\theta_{120} = 40.9 \text{ K}$. Substituting 120/12 into t_b and t_a of Equation (4), $\ln(t_b \cdot t_a^{-1}) = \ln 10 = 2.303$ is obtained. And also, substituting the electrical current value of 2.31 A and electric resistance value $3.94 \Omega \cdot \text{m}^{-1}$ into Equation (4) the following values are obtained:

$$\begin{aligned} \lambda_{200} &= (2.31)2 \cdot 3.94 / 4.314 \times 2.303 / (40.9 - 35.8) \\ &= 0.76 \text{ W} \cdot \text{m}^{-1} \cdot \text{K}^{-1} \end{aligned}$$

As clearly shown above, the measurement of the thermal conductivity can be carried out easily. However, on the other side there is a serious point that requires careful attention. Figure 5 shows the $\theta - \log t$ line of high magnesia content material (the thermal conductivity is $15 \text{ W} \cdot \text{m}^{-1} \cdot \text{K}^{-1}$). In Fig. 4, even after 100 seconds from the beginning point the $\theta - \log t$ line relation maintains linear. In contrast, in Fig. 5 the linearity is suddenly lost in the vicinity of 70 seconds. It is thought that this behavior arises from the phenomenon that the heat arrives at the exterior surface of the specimen as at t_5 in Fig. 1. Table 4 shows the relations between the radial size (the thickness) and the axial size (the length) of the specimen and the thermal conductivity in the time up to the arrival at t_5 following the calculation based on Hayashi's equations^{5,6)} under the conditions of t_b is 300 seconds and a hot wire diameter of 0.3 mm. For example, from the results in the table, when the thermal conductivity of a standard sized brick 230 by 114 by 65 mm was measured in the state of double layers, the length direction is no problem because the conductivity is $15 \text{ W} \cdot \text{m}^{-1} \cdot \text{K}^{-1}$. However, for the radial direction, the solution is limited up to $4 \text{ W} \cdot \text{m}^{-1} \cdot \text{K}^{-1}$ because $114/2 = 56 \text{ mm}$. It is possible to explain, judging from the various behaviors mentioned above, that in the high thermal conductivity material shown in Fig. 5, the diffusion heat from the hot wire arrives at the exterior surface early and due to the thermal environment of the specimen exterior the $\theta - \log t$ line started to be curved at time more than 70 seconds.

This behavior complements the maximum measuring time of Table 3. In other words, in the case of measuring high thermal conductivity material using the cross array method, it shows that compliance with the maximum measuring time is very important to the measurement precision and that the measurement time t_a and t_b must be kept as short as possible for high thermal conductivity material like carbon containing brick in particular.

The second problem of this method is that a single wire method (resistance thermometer method used in ASTM C 1113 and EN 993-14) was introduced for use as an official international standard through the proper channels by amending ISO 8894-1 as of May 15 in 2010. This method, as shown in Figs. 6 and 7, consists of heating the hot wire by a stabilized

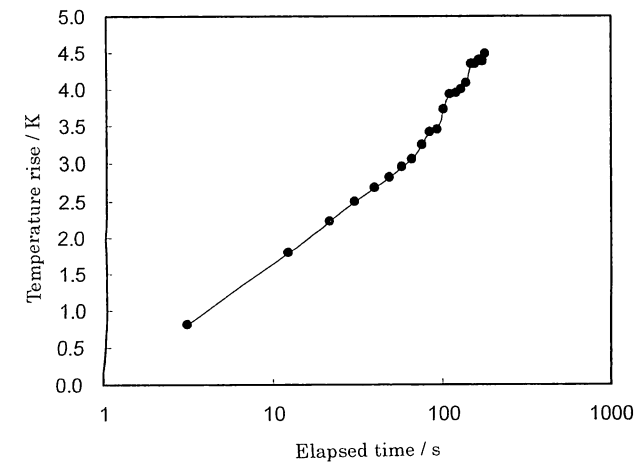


Fig. 5 An example of $\theta - \log t$ line (in the case of MgO system brick).

Table 4 Relation between thermal conductivity and specimen dimensions

Thermal conductivity $/\text{W} \cdot \text{m}^{-1} \cdot \text{K}^{-1}$	Radial direction/ mm	Axial direction/ mm
0.1	8.5	22
0.5	19	36
1	27	45
2	38	57
3	46	65
4	54	71
5	60	76
7	71	85
10	85	95
15	104	108

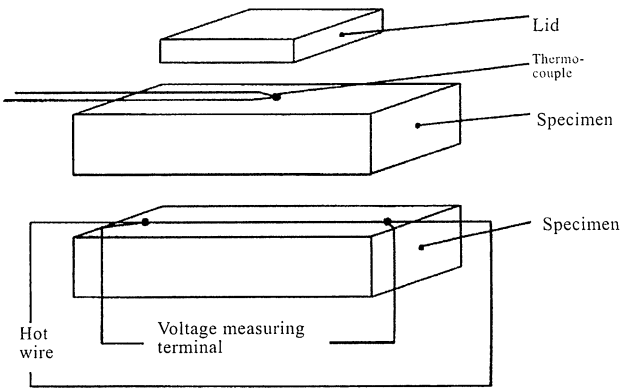


Fig. 6 Connection diagram of the single wire method (resistance thermometer method) (ISO/DIS 8894-1).

alternating current and then turning on a direct current (in this case 100 mA) and measuring the voltage change accompanying the temperature rise of the hot wire to calculate the temperature rise on the basis of the principle of metallic resistance thermometer. This method rests on the same concept as the cross array method in principle but because no thermocouples are used to measure the hot wire temperature it is possible to simplify the platinum wiring arrangement. With regard to establishment of a JIS standard, for instance in the case of JIS R 2251-1 (cross array method), it required time and effort covering about three and one-half years from starting from July 2003 to formulation of the standard in February 2007. However, this single wire method is in widespread use in the USA, Europe and Australia and it is becoming a world standard nowadays and therefore it is thought that it is now time that Japan must make a concerted effort for its practical application.

4.2 JIS R 2251-2 Hot Wire Method (Parallel Method)

Figure 8 shows a schematic drawing of a test apparatus for thermal conductivity by the hot wire parallel array method (hereafter referred to as parallel method), and Fig. 9 displays the layout of the specimen and the connection diagram of the hot wire and thermocouples in the furnace. This method is said to originate from the formulation of a BS specification, but as seen clearly in Table 1, it is in widespread use nowadays throughout the world as well as ISO, EN and AS.

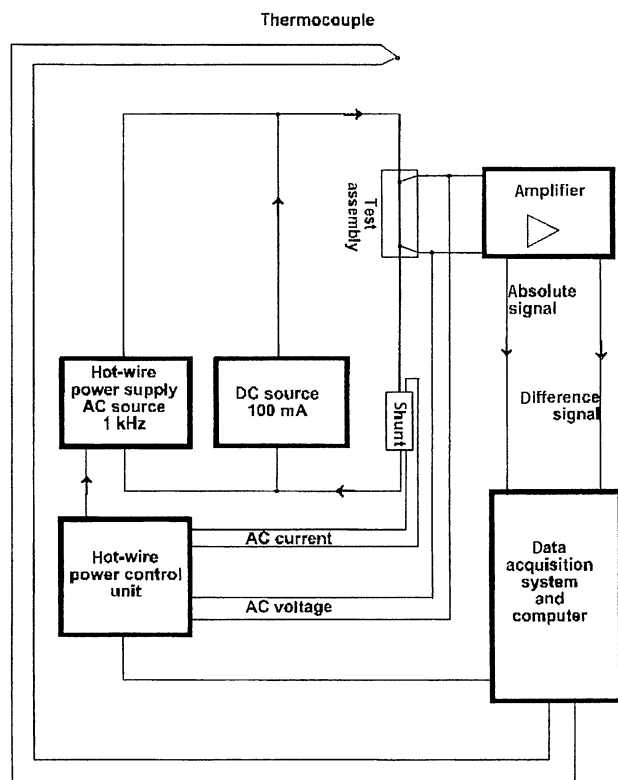


Fig. 7 Overview of test apparatus for single wire method (ISO/DIS 8894-1).

There is little literature in Japan on the parallel method but a lot of papers are found from laboratories overseas. A reason for this difference seems to be the wide scope of measurements of $25 \text{ W} \cdot \text{m}^{-1} \cdot \text{K}^{-1}$. One of the authors engaged in an experiment to develop the measurement apparatus for this method in an effort to complement the cross array method⁷⁾. Nowadays there is an apparatus that can use the parallel method in conjunction with

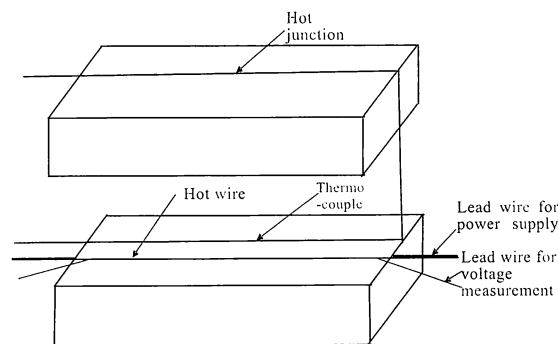
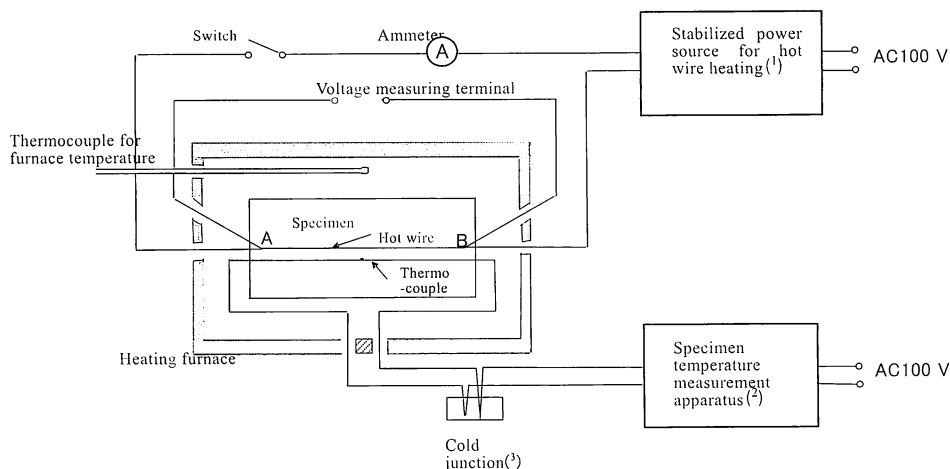


Fig. 9 An example of connection diagram in the parallel method.

the cross array method and further there is even an overseas appliance to use it together with the single wire method.

Measurement operations are as follows:

- 1) The specimen assembly shown in Fig. 9 is placed in an electric furnace with stable temperature control in the manner shown in Fig. 8. (It is also possible to use the vessel for powders and granular particles as shown in Fig. 3-2.)
- 2) Keeping the temperature of the electric furnace at the desired temperature in the measurement range from room temperature to 1250°C , observe that the temperature variation is within 0.05°C during 5 min.
- 3) When the temperature becomes stable, a constant electrical current is applied to the hot wire and the rising temperature is measured by a thermocouple distant from specimen by 15 mm (for example at every one second interval). Table 5 provides the specifications for an adequate supply power and the maximum measuring time against the thermal conductivity.
- 4) The thermal conductivity against each measurement temperature is obtained according to Equation (5):



Note ⁽¹⁾ : It may use either direct or alternate constant current, constant voltage or constant power source, but it confines to one without fluctuation more the 2% during measurement. It is necessary to have the capacity of 10V in voltage and 8A in current.

⁽²⁾ : It consists of a digital multi-meter possessing of time constant more 0.5s and resolving power more than $0.05 \mu\text{V}$ or 0.01°C and a personal computer.

⁽³⁾ : In case of utilizing digital multi-meter equipped with temperature indication function complete with internal temperature compensation circuit, this is no necessary to use.

Fig. 8 An example of test apparatus for thermal conductivity by parallel method.

$$\lambda_0 = \frac{EI}{4\pi l} \times \frac{-E_i\left(\frac{-r^2}{4\alpha t}\right)}{\Delta\theta(t)} \tag{5}$$

where,

- λ_0 : thermal conductivity at measured temperature $\theta(^{\circ}\text{C})$ ($\text{W}\cdot\text{m}^{-1}\cdot\text{K}^{-1}$)
- I : value of electric current applied to the hot wire (A)
- E : voltage drop between A to B of the hot wire in Fig. 8 (V)
- l : length between A to B of the hot wire in Fig. 8 (m)
- $-E_i[-r^2\cdot(4\alpha t)^{-1}]$: exponential integral
- r : distance between hot wire and thermocouple (m)
- α : thermal diffusivity ($\text{m}^2\cdot\text{s}^{-1}$)
- t : heating time for the hot wire (s)
- $\Delta\theta(t)$: rising temperature of the specimen measured by thermocouple ($^{\circ}\text{C}$)

Because the values of $-E_i[-r^2\cdot(4\alpha t)^{-1}]$ are already given as a table filled with the values corresponding to the ratio of rising temperature $\Delta\theta(2t)/\Delta\theta(t)$ at time (t) and $(2t)$, it is possible to read out the required value as needed. Among the thermal conductivity values obtained from this equation, the ones calculated when $\Delta\theta(2t)/\Delta\theta(t)$ is in the midpoint of 1.5 to 2.4 possess the highest reliability.

Table 6 provides measured examples following JIS R

Table 5 Adequate supply power and maximum measuring time for thermal conductivity

Thermal conductivity / $\text{W}\cdot\text{m}^{-1}\cdot\text{K}^{-1}$	Maximum measuring time/ s	Adequate supply power/ $\text{W}\cdot\text{m}^{-1}$
0.1	1200	—
0.4	1200	—
1	900	15
2	450	30
4	350	60
8	190	120
16	100	240
25	65	375

2251-2. In ISO 8894-2: 2007 Annex A, more detailed practical examples are given with a table and a figure (Fig. 10).

According to Table 6 the thermal conductivity can be determined as $15.5\text{ W}\cdot\text{m}^{-1}\cdot\text{K}^{-1}$ which is the mean value of measurement from 18 s to 60 s. On the other hand, according to Fig. 10, it is possible to decide that $5.92\text{ W}\cdot\text{m}^{-1}\cdot\text{K}^{-1}$ is a mean value of measurement results from 40 s to 150 s.

The parallel method is naturally affected by the thickness of specimen in the same manner as the cross array method and the maximum measuring time is determined according to the level of thermal conductivity. This behavior can be understood easily from the practical example mentioned above and therefore it is necessary to pay special attention in the measurement.

Figure 11 displays the results of joint research by a subcommittee of the Standardization Committee in TARJ (hereafter simply referred to as round robin test) carried out for fireclay bricks by the cross array⁸⁾ and parallel methods⁹⁾. (The calculations for the parallel method were carried out using the same program except for specimen L7.1.). It became clarified from these results that: ① Even in the same measuring method there were differences of 0.3 to 0.4 $\text{W}\cdot\text{m}^{-1}\cdot\text{K}^{-1}$ between laboratories. ② There were great differences in measured values between the cross array method and the parallel method and it was possible to infer the obvious trend that the values of the cross array method were larger than those of the parallel method. It is possible to conclude, judging from the results mentioned above, that the values of the thermal conductivity obtained by the cross array method and the parallel method are not in an accuracy class as high as $\text{RSD}<0.5$ found in chemical analysis, but in a class as rough as RSD between laboratories, $>\pm 10$ to 20%, that show deviations similar to those between the above methods. In addition, according to the simple repeated test at OCC, it was possible to obtain results with RSD at 1% or within a few%, which was excellent performance. It is possible to think that the reasons leading to such great differences arise largely from differences in the apparatus and the manufacturing techniques for the test specimen assembly (particularly the technique of setting the hot wire and thermocouple on the

Table 6 Calculation example for thermal conductivity by parallel method-transient hot wire method

Time t s	$\Delta\theta(t)$		$\frac{\Delta\theta(2t)}{\Delta\theta(t)}$	$-E_i\left(\frac{-r^2}{4\alpha t}\right)$	Thermal conductivity λ $\text{W}\cdot\text{m}^{-1}\cdot\text{K}^{-1}$	Average λ $\text{W}\cdot\text{m}^{-1}\cdot\text{K}^{-1}$
	μV	K				
6	0.55	0.054	4.46	0.049 6	13.2	15.5
12	2.47	0.241	2.46	0.243 4	14.5	
18	4.45	0.434	1.96	0.478 8	15.8	
24	6.08	0.593	1.78	0.652 1	15.7	
30	7.47	0.729	1.69	0.776 4	15.3	
36	8.72	0.851	1.61	0.919 7	15.5	
48	10.82	1.056	1.52	1.135 8	15.4	
60	12.60	1.229	1.46	1.327 4	15.5	
72	14.05	1.371				
96	16.47	1.607				
120	18.40	1.795				

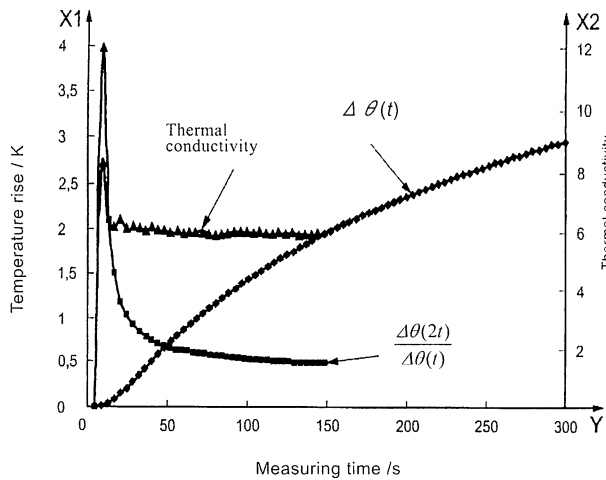


Fig. 10 An example of summary of measured results by parallel method.

specimen)

4.3 JIS R 2251-3 Heat Flux Method

Figure 12 is a schematic drawing of the test apparatus for the heat flux method specified in JIS R 2251-3. Figure 13 displays a detailed diagram of the measurement system for thermal conductivity and Fig.14 shows the shape and dimensions of the specimen. This apparatus was adopted for joint research because this type of apparatus is in operation now in at least 5 domestic laboratories of the same industry.

The apparatus of ASTM C 201 (Fig. 15) introduced in Table 1 measures the thermal conductivity of refractories by the heat flux method, but at the time the standard for this method was under review, there was no apparatus of this type in operation in Japan. The appeal of the ASTM method is that a straight standard shape brick can be used as the specimen and the specimen is large, similar to the two methods described

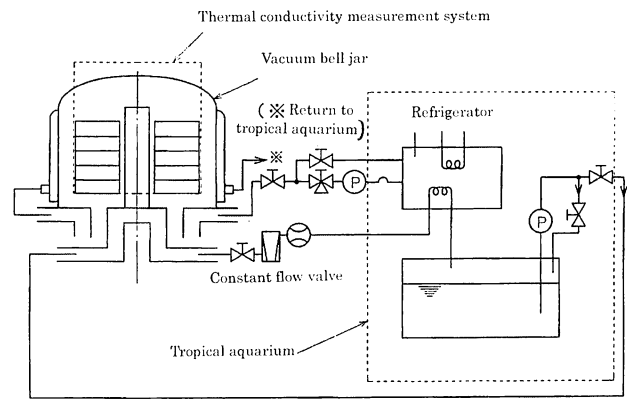


Fig. 12 Schematic drawing of test apparatus for heat flux method.

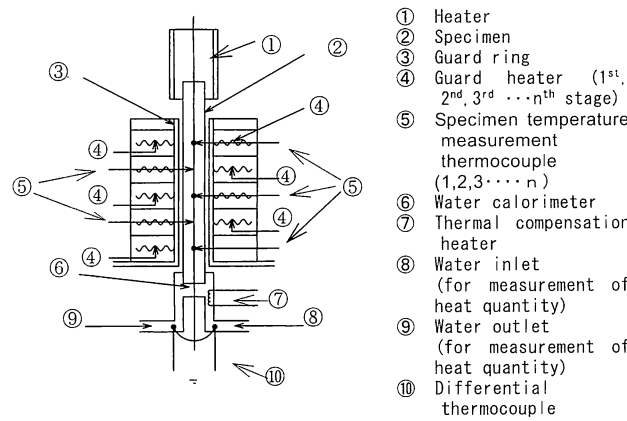


Fig. 13 Detail view of measurement system for thermal conductivity.

previously. On the other hand, the heat flux method in the JIS specification uses a specimen of a particular cylindrical shape of 150 mm long and 20 mm in diameter with five holes 2.2 mm ϕ and 10 mm deep to accommodate thermocouples placed as shown in Fig. 14. The measurement operations are as below:

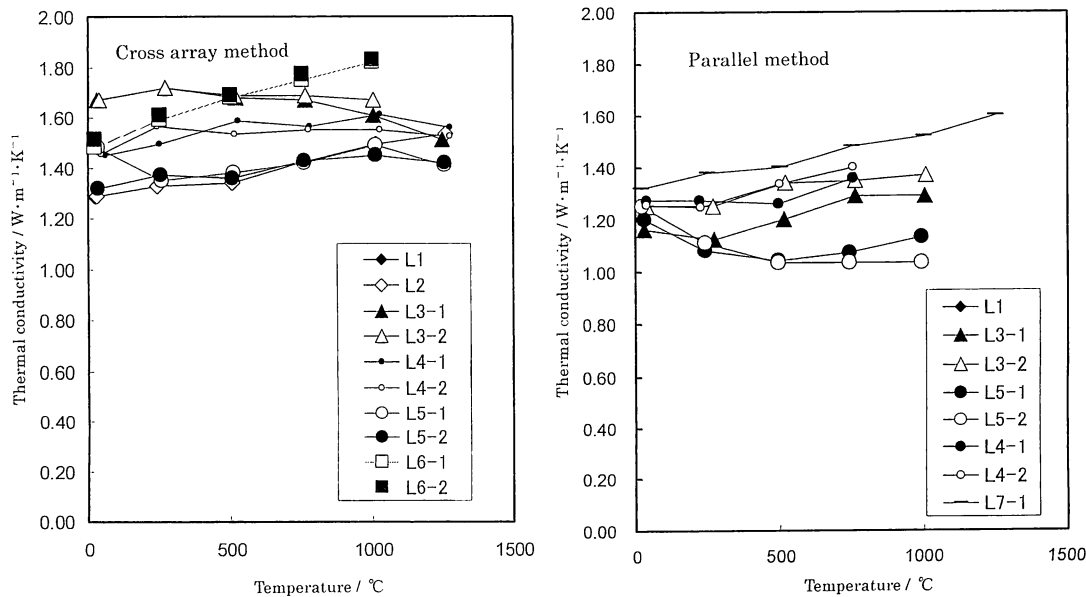


Fig. 11 Results of round robin test (measurement of thermal conductivity for fireclay bricks by cross array method and parallel method).

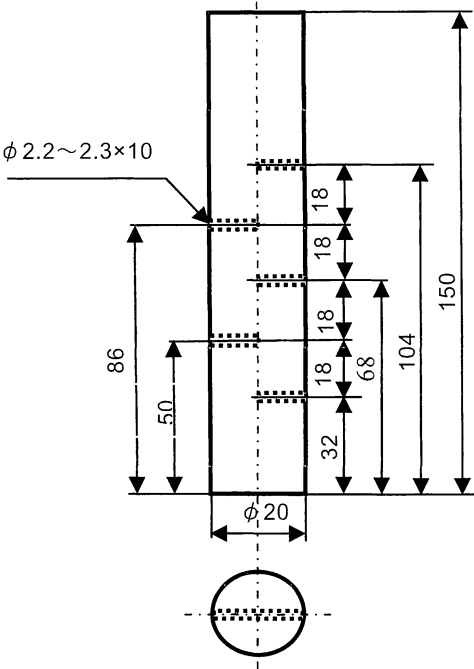


Fig. 14 Shapes and dimensions of specimen.

- 1) The specimen is set up in the manner shown in Fig. 13 so that the central specimen axis aligns with the central axis of specimen heater ① and water calorimeter ⑥. Sheathed thermocouples are attached in each hole in the specimen.
- 2) A certain amount of water (for example $400 \pm 1 \text{ ml} \cdot \text{min}^{-1}$) is flowed into the water calorimeter ⑥ for calorimetry.
- 3) Power is applied to the specimen heater and, after the temperature of the top and bottom surfaces of the specimen reach a given value, the system is kept another 30 min or more to obtain a steady state.

- 4) The local temperature at each thermocouple position is measured.
- 5) A micro potentiometer (with the sensitivity in $1 \times 10^{-6} \text{ V}$ or so) is used to measure the temperature difference of the water between the inlet ⑧ and outlet ⑨ for measurement of the quantity heat in the water calorimeter ⑥.
- 6) Applying a certain electric power $P \text{ (W)}$ (for example, $3 \text{ V} - 1.8 \text{ A}$) on a compensation heater ⑦, the value of the micro potentiometer is read to measure the temperature difference between the water inlet ⑧ and outlet ⑨ for calibration of the heat quantity.
- 7) The thermal conductivity at each measuring temperature is obtained according to following equation.

$$\lambda_{\theta_{i-1}} = \frac{PL}{A} \times \frac{T_1}{(T_2 - T_1)(t_{i-1} - t_i)} \quad (6)$$

where,

θ_{i-1} : measured temperature at the $(i-1)$ th point from high temperature side. (the mean temperature between t_{i-1} and t_i) ($^{\circ}\text{C}$)

$\lambda_{\theta_{i-1}}$: thermal conductivity at the measured temperature at the $(i-1)$ th point from higher temperature side. ($\text{W} \cdot \text{m}^{-1} \cdot \text{K}^{-1}$)

t_{i-1} : temperature within the hole for temperature measurement at the $(i-1)$ th point from higher temperature side ($^{\circ}\text{C}$)

t_i : temperature within the hole for temperature measurement at the (i) th point from higher temperature side ($^{\circ}\text{C}$)

P : supplied electric power to compensation heater (W)

L : distance between each hole in the specimen (m)

A : cross sectional area of specimen (m^2)

T_1 : temperature difference obtained from step 5 ($^{\circ}\text{C}$)

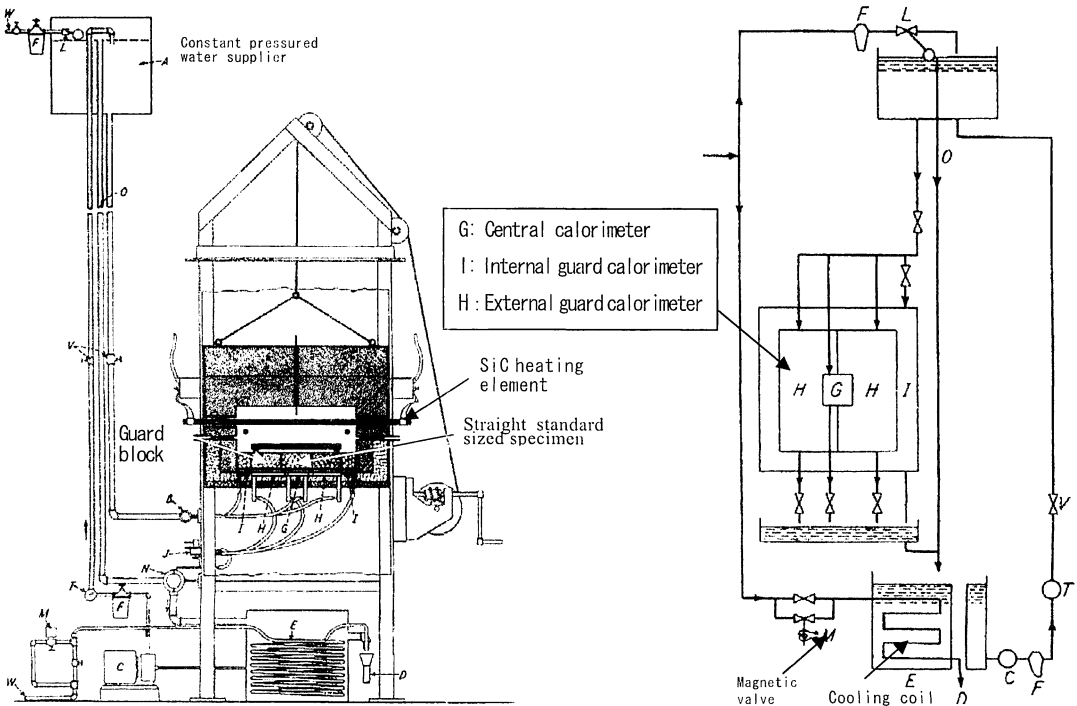


Fig. 15 Brief overview of test apparatus for heat flux method by ASTM C 201.

T_2 : temperature difference obtained from step 6 (°C)

Figure 16 shows some measured results using a stainless steel rod with known thermal conductivity in an effort to ascertain the accuracy of this method. In addition a laser flash test method was applied to compare with the results of the heat flux method by several laboratories. It is possible to conclude, judging from this result, that there was very little difference between the measured values of each laboratory. This is because the test apparatus used was the same type by the same manufacturer, the specimen was comparatively homogeneous and a commonly worked specimen was distributed to each laboratory. Also, the results by heat flux method were in good agreement with those of the laser flash method.

The characteristics and problems of this heat flux method can be enumerated as follows:

- (1) It is even applicable to an electrically conductive material.
The cross array method and parallel methods are impossible to apply to electrically conductive carbon and silicon carbide containing refractories or to zirconia system refractories that become electrically conductive at high temperature. This heat flux method has solved this difficult problem by taking advantage of the property of the steady method that does not make an issue of measurement time delay due to utilizing a sheathed thermocouple.
- (2) Different from the ASTM method, it is able to measure the thermal conductivity at four levels of temperature in a single procedure. The heat flux method is a steady state method and therefore it is based on the rule that the measured temperature is obtained from a mean temperature of two measurement points and the thermal conductivity is determined as the value at this temperature. Making up the temperature within each hole to t_1 , $t_2 - t_5$ from high temperature side, the measured temperature θ_i becomes 4 ($= 5 - 1$).
- (3) In the apparatus for this method, it is impossible to design a heater to heat the typical specimen to more than 1000°C and therefore the upper limit of measurement is as low as 800°C (It is impossible to heat the top sufficiently to make the mean temperature between the first and the second points greater than 800°C)

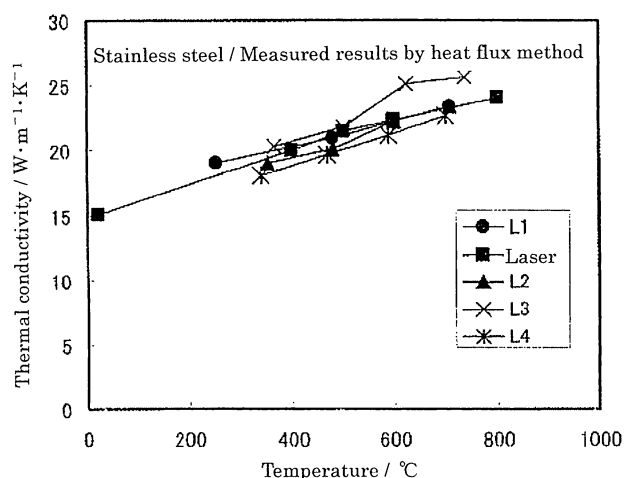


Fig. 16 Test results of round robin test by heat flux method.

- (4) It requires a lot time to prepare the specimen because the shape of the specimen is so complex,
- (5) It is necessary to pay careful attention in the case of using a specimen containing large grain size because the specimen diameter is only 20 mm and the interval between each measuring hole is as narrow as 18 mm,
- (6) The measurement temperature of the thermal conductivity by the steady state method is represented as the mean temperature between two points. Therefore, unlike stainless steel, in the case of a material whose thermal conductivity varies along a quadratic curve with rising temperature, strictly speaking, the data obtained by the steady state method is different from that of the transient state method.

4.4 Laser Flash Method

Differing from the cross array method and the parallel method mentioned above, the laser flash method does not measure the thermal conductivity directly as mentioned in the Section 2.2. It is a method to get the thermal conductivity by calculation based on the relational Equation (1) using the values of the thermal diffusivity and specific heat capacity obtained from the rising temperature curve of the reverse face of a specimen when the obverse face is radiated by a laser pulse. In addition, in the case of a complex continuous fiber reinforced ceramic material, which as shown in Table 2 is the same sort of heterogeneous material as refractories, the laser flash method plays the role to measure only the thermal diffusivity while the specific heat capacity is measured with a differential scanning calorimeter (DSC). In the following, the authors describe the measuring method for thermal diffusivity and specific heat capacity by the laser flash method and consider the problems in applying this method to refractories.

4.4.1 Thermal Diffusivity

Figure 17 shows an example of a constitution drawing of a laser flash apparatus for thermal diffusivity measurement specified in JIS R 1667. Measurement operations are given below. (It combines measurement for specific heat capacity).

- 1) Provide a disc shape specimen with flat and smooth surfaces (for example 10 mm in diameter and 3 mm thick). Measure and record the thickness (with accuracy of 1 μm), the diameter (with accuracy of 1 μm) and the mass (with accuracy of 0.1 mg).
- 2) Spray coat a paint containing carbon micro-particles on the entire specimen surfaces (It may be vacuum deposition) to form thin homogeneous blackened carbon membrane on the surface.
- 3) Put the specimen into a specimen holder and attach it to the apparatus shown in Fig. 17. The specimen is then heated in an electric furnace in flowing ambient gas up to a predefined temperature.
- 4) When the specimen temperature becomes stable, irradiate a laser pulse homogeneously on the top face of the specimen and then measure the time change of the temperature on the reverse face with an infrared sensing device. The result is the

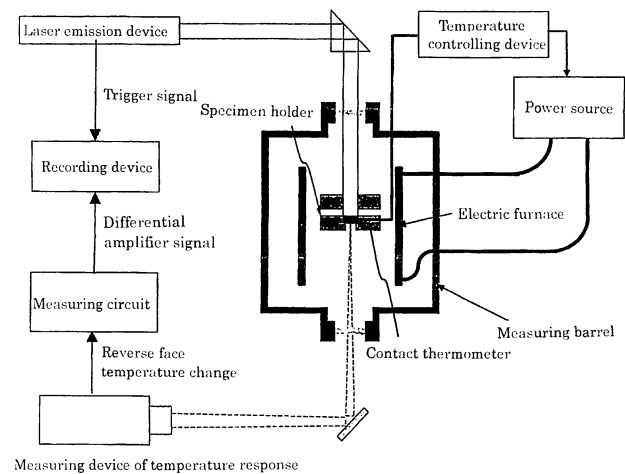


Fig. 17 An example of constitution drawing of laser flash apparatus.

temperature increase curve by the laser flash method as shown in Fig. 18.

5) From the values measured at half rise-time, the thermal diffusivity can be calculated by following equation:

$$\alpha = 0.1388 \times k_{bc} k_m \frac{l^2}{t_{1/2}} \quad (7)$$

where,

- α : thermal diffusivity ($\text{m}^2 \cdot \text{s}^{-1}$)
- l : thickness of specimen (m)
- $t_{1/2}$: half rise-time (s)
- k_{bc} : modification coefficient against blackened carbon membrane
- k_m : modification coefficient for the measurement condition

Generally speaking in the case of refractories, the modification against k_{bc} and k_m can be ignored and therefore the thermal diffusivity is obtained easily from Equation (7). Fig. 19 is an example of the rising temperature curve for MgO-C brick at room temperature⁽¹⁰⁾.

4.4.2 Specific Heat Capacity

When measuring the specific heat capacity, it is necessary to place a thermocouple on the specimen as shown in Fig. 20, and in particular in the case of measuring both the specific heat capacity and the thermal diffusivity at once, it is necessary to pay careful attention not to overlap the thermocouple position and the contact-free measuring position.

The specific heat capacity can be obtained with the following equation by substituting the values q (the relative laser intensity) obtained from the rising temperature curve of Fig. 18 using the specimen thermocouple set-up shown in Fig. 20, ΔT_{ext} (extrapolated value of rising temperature), and the modification value obtained from measuring a standard material with well known in specific heat capacity measured in a similar way to the specimen (in the case of room temperature).

$$C = \frac{1}{m} \left(\frac{Q}{\Delta T_0} - C_2 m_2 - C_3 m_3 \right) \quad (8)$$

where,

- C : specific heat capacity of specimen ($\text{J} \cdot \text{kg}^{-1} \cdot \text{K}^{-1}$)
- m : mass of specimen alone (g)
- Q : absorbed heat quantity (J)
- $Q = a + b \cdot q$ (a and b are correction factors)
- C_2 : specific heat capacity against a light reception board ($\text{J} \cdot$

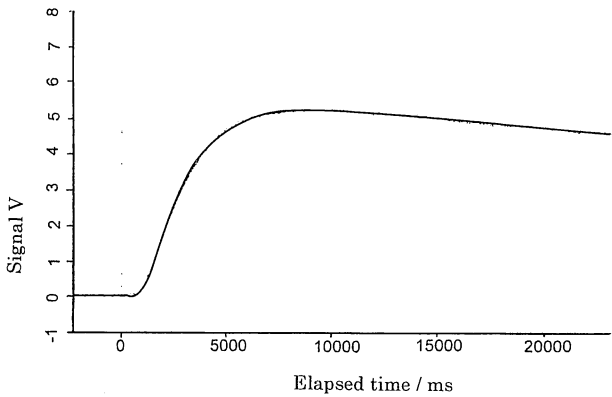


Fig. 19 An example of temperature rising curve of MgO-C brick.

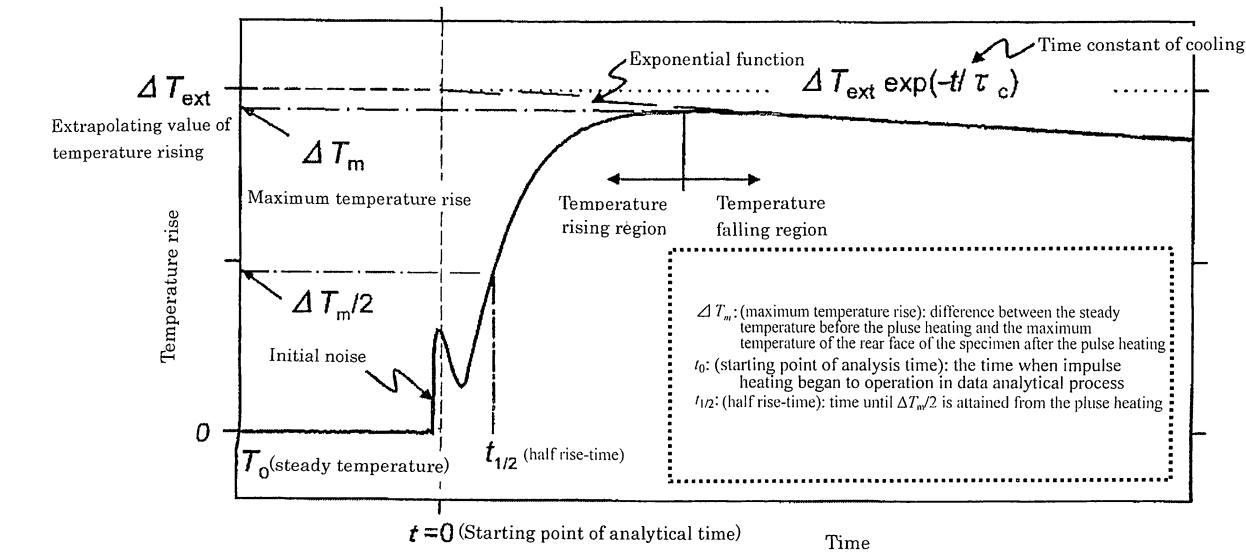


Fig. 18 Temperature rising curve observed by laser flash method.

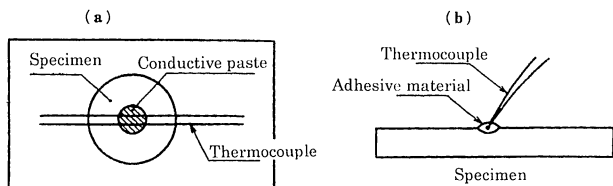


Fig. 20 Method of attaching the thermocouple to the specimen.

$$\text{kg}^{-1}\cdot\text{K}^{-1})$$

C_3 : specific heat capacity against the adhesive material ($\text{J}\cdot\text{kg}^{-1}\cdot\text{K}^{-1}$)

m_2 : mass of the light reception board (g)

m_3 : mass of adhesive material before test (g)

For measuring the specific heat capacity, it is essential include a correction using a standard material, even in the DSC method, and therefore there is no choice regarding the execution of the correction. However, in the case of the laser flash method with the attachment of a thermocouple, the correction against a light reception board and the adhesive material (in case of JIS R 1611) are not only very complicated but also cause a decrease in measurement accuracy and therefore it is very desirable to have improvement as a burning issue in the JIS specification.

4.4.3 Thermal Conductivity

Thermal conductivity can be calculated by multiplication of the values of thermal diffusivity, specific heat capacity and bulk density substituted into Equation (1) in Section 2.2.

Figure 21 shows an example of measurement results for thermal conductivity of MgO-C brick by means of the laser flash method¹⁰⁾.

4.4.4 Discussions on Application Possibility of Laser Flash Method to Measurement for Thermal Conductivity of Refractories

The explanation mentioned above with regard to the laser flash method is mainly with reference to fine ceramics related JIS specifications. It is not too much to say that the laser flash method has become completely established as an essential technology to measure thermal conductivity of fine ceramics at

least. The authors describe below the technological problems in the case of applying the laser flash method to measure the thermal conductivity of refractories and the recent movement on this method.

(1) Specimen shapes and thermal conductivity:

Refractories are heterogeneous bodies consisting of dissimilar materials including different kinds and different sizes of particles. Therefore it is desirable that the size of a test specimen is large enough that these particle sizes and heterogeneous structures appear homogeneous. It is difficult to think that the previously mentioned specimen dimensions of 10 mm diameter×3 mm thick are enough to satisfy such a requirement. In the German-made apparatus that OCRF imported recently, a specimen of $\phi 25.4\times 10$ mm can be utilized as a standard. Although it is impossible to make an assertion that even such a size is enough, there is a table shown in Table 7¹⁰⁾ as an annex to the manufacturer data. Details such as the thermal history records of specimens are unexplained, but judging from the table, the relative standard deviation (RSD) is only 1 % or so among all the items and therefore it is possible to say this is excellent compared with data obtained from the other measuring methods for thermal conductivity

(2) Measuring technique of specific heat capacity.

As mentioned above, it was necessary to attach a thermocouple and to correct the values against a light reception board and the adhesive material in the conventional apparatus used in Japan. However, in the advanced apparatus introduced by OCRF as mentioned above, these treatments are unnecessary. The values provided in Table 7 are results showing the reproducibility of repetitive tests under controlled unified test conditions. As for the measurement of specific heat capacity, it is necessary to execute corrections using a standard material. There are a few correction equations to apply to correct variation, but it is not uncommon to increase the variation to 10% or more according to the operation of the equation. For example, in the case of correcting against heterogeneous materials such as refractories, it is necessary to make use of a standard material possessing the same quality as the one being tested, but unfortunately there is no material appropriate in this situation. In

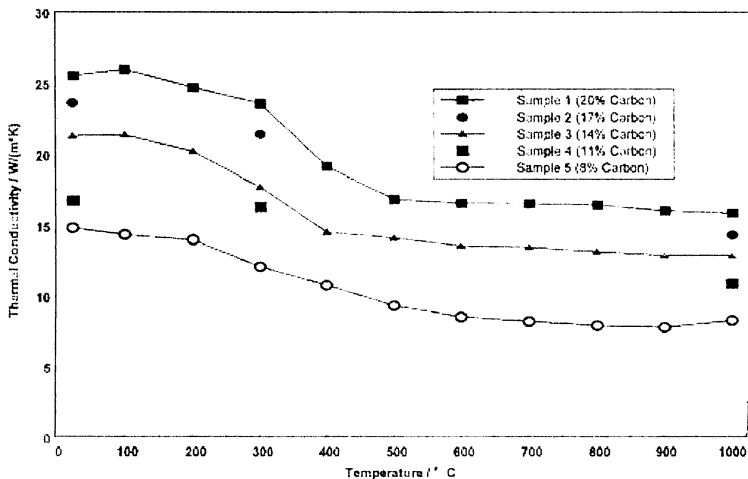


Fig. 21 An example of measured results of thermal conductivity for MgO-C brick.

Table 7 Results of reproducibility test in measurement of thermal conductivity for MgO-C brick

Item		Thickness mm	Bulk density g·cm ⁻³	Thermal diffusivity mm ² ·s ⁻¹	Specific heat capacity J·g ⁻¹ ·K ⁻¹	Thermal conductivity W·m ⁻¹ ·K ⁻¹
Specimen No.	x ₁	10.44	2.878	9.95	0.891	25.5
	x ₂	10.43	2.893	9.83	0.879	25.0
	x ₃	10.22	2.908	9.75	0.890	25.2
	x ₄	10.43	2.896	9.70	0.901	25.3
Avarage		10.38	10.38	2.904	9.81	0.890
SD		0.107	0.11	0.012	0.11	0.009
RSD(%)		1.0	1.0	0.4	1.1	1.0

Remarks: using four test specimens cut off from original specimen under test, each specimen was measured on the items at room temperature (at 26℃)

other words, it is considered that a lot of standard material assignments must be resolved for the sake of measurement of specific heat capacity for refractories. When the specific heat capacity was measured in the case of continuous fiber reinforced ceramics, DSC was used, and on the basis of a similar concept, it may be a good option to adopt DSC for the measurement of the specific heat capacity of refractories. Also, for measurement of the specific heat capacity it may be necessary to investigate a method other than DSC; e.g. a dropping method.

(3) Investigation of previous literature and re-examination of application feasibility

With regard to review of the application feasibility of the laser flash method to refractories, there is literature in the Ceramic Society of Japan, "Survey Research Committee on Standardization of Energy Saving Industrial Furnaces" led by Prof. Dr. Suzuki on observations through seven years in the 1980's. In this review the committee concluded that knowing exact values of the thermal conductivity of refractories used in industrial furnaces is an essential condition for the standardization of industrial furnaces. Therefore comparison examinations were carried out using the same specimen and calling out all kinds of measuring apparatuses that existed at that time in Japan. The authors would like to reexamine the literatures obtained at that time and are currently searching the availability. In any event, mentioning the example of OCRF's apparatus, nowadays both the measuring apparatus and the measuring technologies are making rapid progress supported by the epoch-making diffusion of personal computers. The laser flash method can be measured relatively easily and can measure up to higher temperature than the heat flux method. In particular, it raises the expectation for application to electrically conductive materials that up to now have not had an applicable test method to measure thermal conductivity.

5. Conclusions

In 2007, the JIS test method for thermal conductivity of

refractories was established. This paper introduced the technologies.

Official test methods are very important as evidence to support daily experimental and measurement work of people engaged in the field. Therefore it is thought that the establishment of JIS R 2251-1 to -3 became God's Word for persons occupied in examination and measurement services. However, as a result of compiling this paper, it became apparent that in speaking about JIS specifications there are problems that remain to be solved such as the single wire method, reproduction accuracy and inspection for the laser flash method as new problems. For these problems the authors know full well it is necessary to continue discussions and research from now on.

References

1) for example, Sadao Mouri: *Yougyou Kyoukaishi*, 62 [698] 493-497 (1954)
2) Masao Fukui and Kunio Hayashi : *Taikabutsu* 30 [7] 360-364 (1978)
3) Kunio Hayashi: *Taikabutsu* 41 [5]270-279 (1989)
4) Kunio Hayashi: Standardization Committee in TARJ, 17th Physical Test Subcommittee Data No. 225 (2007)
5) Kunio Hayashi, Yuzo Nishikawa and Isao Uei: *Yougyou Kyoukaishi*, 81 [12] 532-537 (1973)
6) Kunio Hayashi, Yuzo Nishikawa and Isao Uei: *Yougyou Kyoukaishi*, 82 [4] 202-208 (1974)
7) Masayuki Nakatsukasa, Hideo Asakura and Kenji Ichikawa: *Taikabutsu* 49 [11] 651 (1997)
8) Hideo Asakura: Standardization Committee in TARJ, 6th Physical Test Subcommittee Data No. 53 (2004)
9) Hideo Asakura: Standardization Committee in TARJ, 6th Physical Test Subcommittee Data No. 54 (2004)
10) Data of LFA 457 from Bruker AXS K. K.
Translated from *Taikabutsu* 62 [8] 388-400 (2010)

Paper

Influences of Distribution of Al Additive on Properties of MgO-C Refractories

Fuminori HIROSE, Akira YAMAGUCHI, Yasuhiro HOSHIYAMA and Junji OMMYOJI

Abstract

Various kinds of metals are added to carbon-containing refractories as antioxidants. The degree of the effect of the metals is quite different by their kind, quantity and distribution in the refractories. In this study the most effective and ideal method the distribution of metal Al in refractories was examined. As a result, when metal Al was distributed homogeneously among graphite grains, the pore size in the refractories became smaller and there was less decrease in strength after heating. Moreover, densification of the refractories was promoted because of the formation of spinel crystals among the graphite grains. On the other hand, when Al grains were in contact with the surface of MgO grains, the pore size became larger and there was greater decrease in the strength.

From the above-mentioned results, it is desirable to distribute Al grains during process of mixing raw materials of the refractories.

Key words: microstructure, Al-additive, MgO-C brick, carbon- containing refractories, densification

1. Introduction

Anti-oxidants in carbon containing refractories not only take on the role of preventing oxidization of the carbon but also advancing the strength after thermal loading¹⁾. The most important factors on such occasions are the correct selection of the kind of anti-oxidant to exert the most effective results at the service temperature and the proper execution of the method of addition. At present the SiC and/or Al powder anti-oxidants that are commonly used are good choices on the basis of the chemical thermodynamics to function properly as anti-oxidants at the service temperature²⁾. The behavior of metals added to carbon-containing refractories as anti-oxidants has been the subject of a number of researches up to now, and it has been clarified that addition of metals brings about changes in the microstructure and in the corrosion resistance of MgO-C bricks at high temperature according to the kind of added metals³⁻⁵⁾. Also it is well known that the addition of metal to carbon containing refractories reduces the open porosity and prevents the oxidation of carbon during use at high temperature⁶⁾. Furthermore it is adequately understood that with regard to the behavior of Al metal added to MgO-C bricks, the particle size of the Al metal has a great influence on the amount of pore formation at high temperature. Also it is said that the introduction of smaller grains of Al metal improves the densification of the structure at high temperature⁷⁾. As described above, with regard to the behavior of metal addition to carbon containing refractories and the influence of metal on the properties of bricks, the mechanisms have been clarified from various viewpoints such as microstructure observation and thermodynamics. On the other hand, the influence of the microstructure of refractories as related to the distribution morphology of anti-oxidant on the properties of bricks has been scarcely investigated in detail. Recently the graphite content in carbon containing refractories has consistently decreased every year. It is important to clarify the relation between the

microstructure and the properties of carbon containing refractories for the special benefit of preventing the oxidation of graphite effectively. Moreover, the reaction between the added anti-oxidant agent and the oxides of the prime components of refractories progresses through the intermediary of vapor phases in carbon containing refractories and therefore the microstructure after use at high temperature is quite different from that before use. Consequently it is possible to conclude that the microstructure of bricks has an extremely important influence on the brick properties. For this reason the authors provided two kinds of MgO-C bricks with different distribution morphologies of Al grains added as an anti-oxidant and investigated the microstructures and properties of the bricks after heating. As the result it was clearly indicated that the microstructure has an influence on the properties of bricks in carbon containing refractories. The paper reports the proceedings of this research.

2. Experimental Procedures**2.1 Preparation of Specimens**

Table 1 provides raw materials and their proportions used in specimens of MgO-C bricks. In addition "ex. 5 mass%" in the table expresses an exclusive percentage; in other words it denotes that when the sum of the mass of electro-fused MgO and flaky graphite, the main raw materials, was defined as 100 mass%, the mass of metal Al powder added corresponded to 5% of the sum. The raw materials used were: electro-fused MgO (hereafter referred to as MgO) made by Tateho Chemical Industries Co., Ltd. with 99 mass% purity and sieved to select a grain size interval less than 1.0 mm and greater than 0.5 mm. and flaky graphite (hereafter referred to as graphite) made in China, with 99 mass% purity and less than 150 μm in size. The antioxidant material used was metal aluminum powder (hereafter referred to as Al powder) of 99 mass% purity and size less than 45 μm made by Toyo Aluminum KK. As a binder, novolac type liquid phenolic resin made in Sumitomo Bakelite Co., Ltd. was

used, and as the hardening agent commercially produced hexamethylene tetramine. The mixed body shown in Table 1 was well kneaded for a specified time, formed by a uniaxial pressing machine and baked for heat-treatment at 200℃ for 12 hours to prepare the brick specimen.

Figure 1 illustrates production processes of the MgO-C brick specimens. Two procedures were employed to provide specimens with different microstructures. One method was to knead the MgO, Al powder and phenolic resin together and then add the graphite. The specimen produced by the above method is referred to as the M-Al specimen. The second method was to knead the MgO and phenolic resin together first and then add graphite to the mixture. The mixed body was well stirred, Al powder was then added to the mixture and the final kneading was carried out. The specimen produced by the second procedure is referred to as the M-C specimen. Part of each mixed body was formed into cylindrical shapes 30 mm in diameter and 25 mm long and the residual part was formed into rectangular solid bodies 120 by 25 by 25 mm using a uniaxial pressing machine. The formed bodies were baked at 200℃ for 12 hours. Polished pieces were produced from the cylindrical specimens for microstructure observation and elemental analysis measurements and the rectangular solid specimen was utilized for measurements of physical properties such as apparent porosity, bulk density, apparent specific gravity and the modulus of rupture.

Table 1 Composition of MgO-C brick samples

Raw material	Mass%
Fused MgO (0.5-1mm)	50
Flake graphite (<0.15mm)	50
Al powder (<45 μm)	ex. 5
Phenol resin	ex. 6
Hexamethylenetetramine	ex. 0.6

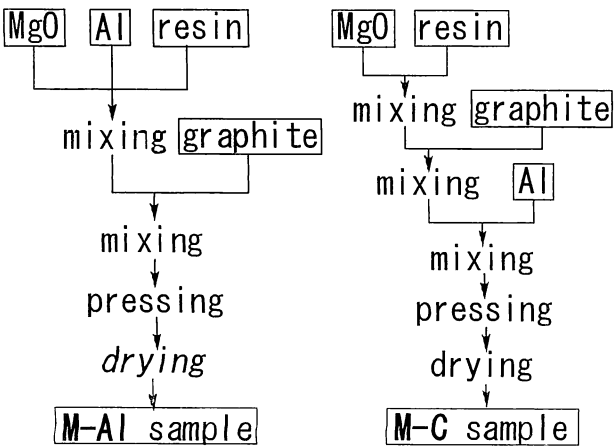


Fig. 1 Production process of MgO-C brick samples.

2.2 Measurement and Microstructure Observation

The measurements of apparent porosity, bulk density and apparent specific gravity after baking at 200℃ for 12 hours were carried out by the Archimedeian method according as JIS R 2205. The modulus of rupture was measured by three-point bending using a rectangular solid specimen 25 by 25 by 120 mm supported on rollers at a span length of 100 mm,. The microstructure observation was on a polished section encapsulated in epoxy resin using an optical microscope and a scanning electron microscope (SEM). Also with the aim of observing changes in the microstructure and the values of physical properties due to heating, specimens were buried in graphite powder and heated up in reducing ambient atmosphere at a rate of at 5℃/min to 1600℃ and held for 3 hours. The physical properties of apparent porosity, bulk density, apparent specific gravity and modulus of rupture after firing were measured and compared with those before firing. Also, the pore diameter distribution in the specimens after firing was measured by Mercury intrusion. Moreover the crystal phases in the specimen after firing were examined by powder X-ray diffractometry and the element distribution was measured by EDS (Energy dispersive X-ray spectrometry) using a polished piece encapsulated in epoxy resin.

3. Results

Figure 2 displays an optical photomicrograph of the microstructure of both MgO-C brick specimens after baking. The structure of the M-Al specimen is characterized by a lot of Al powder contacting MgO grains, while in the M-C specimen a lot of Al is dispersed among the voids of graphite grains.

Figure 3 compares the apparent porosity of both MgO-C brick specimens after baking at 200℃ and after heating at 1600℃. Both after 200℃ baking and after 1600℃ heating, the apparent porosity of the M-C specimen was lower than that of M-Al.

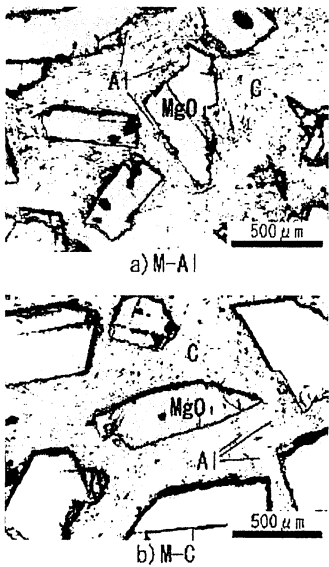


Fig. 2 Microstructure of MgO-C brick samples after baking at 200℃.

Figure 4 compares the modulus of rupture of specimens after baking at 200°C and after heating at 1600°C. As a reference the values for a specimen without Al powder additive are included. In the case of baking at 200°C there was no significant difference in the strength among three specimens: no additive, M-Al and M-C. On the contrary, after heating at 1600°C, the M-C specimen displayed the highest value with the M-Al specimen in the middle while the specimen with no Al powder additive showed the lowest value.

Figures 5 and 6 show the powder X-ray diffraction patterns of M-Al and M-C specimens after heating at 1600°C. In both M-Al and M-C, the aluminum peaks disappeared and new peaks of spinel were observed. It is well known that when a mixture of Al, MgO and graphite is heated at high temperature, $MgAl_2O_4$ is formed¹⁾, and therefore it is consistent with the experiment results observed here.

Figure 7 shows a SEM image in the vicinity of a boundary between a MgO grain and Al grains and the elemental mapping of Al, Mg and O in the M-Al specimen. In the SEM image, the upper part of the image shows a portion existing in graphite. With regard to the MgO grain, a high concentration of Mg is observed within the original MgO grain. On the other hand, Al, Mg and O coexist in the vicinity of the surface of the MgO grain. Also, pores 10 to 15 μm in diameter were observed in the peripheral part of MgO grains that seemed to be vestiges of Al grains, and around the pores a thin layer about 1 μm wide is seen that contains distributed Al, Mg and O is indicated by (X) in the photo. Furthermore, Al, Mg and O are observed to coexist among the graphite grains.

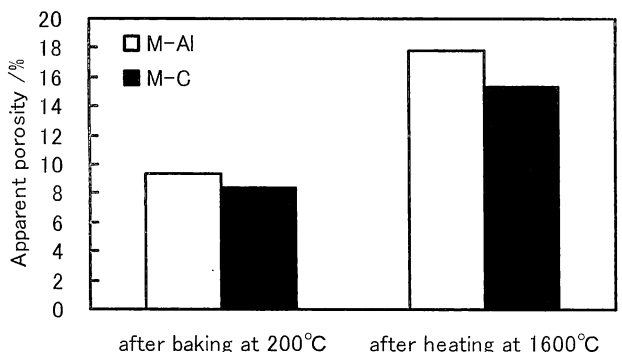


Fig. 3 Apparent porosity of MgO-C brick samples after baking at 200°C.

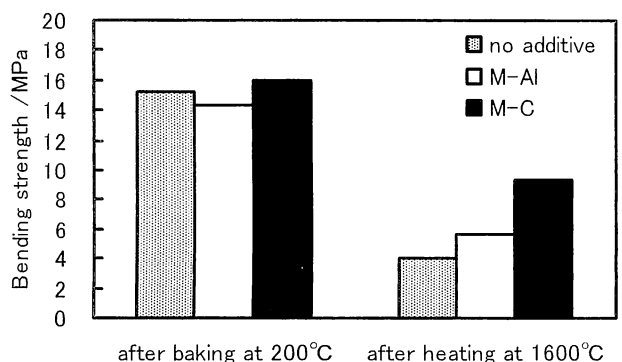


Fig. 4 Bending strength of MgO-C brick samples after baking at 200°C.

Figure 8 shows a SEM image in the graphite matrix area that includes features that seem to be vestiges of Al grains and the elemental mapping of Al, Mg and O in the M-C specimen. It can be observed in the portion (X) that Al, Mg and O are distributed in a 10 μm wide circular strip around a pore less than 5 μm in diameter. Even in the portion (Y) where it seems that no Al grain exists, the presence of Al, Mg and O is observed.

Figure 9 shows pore diameter distributions for both MgO-C

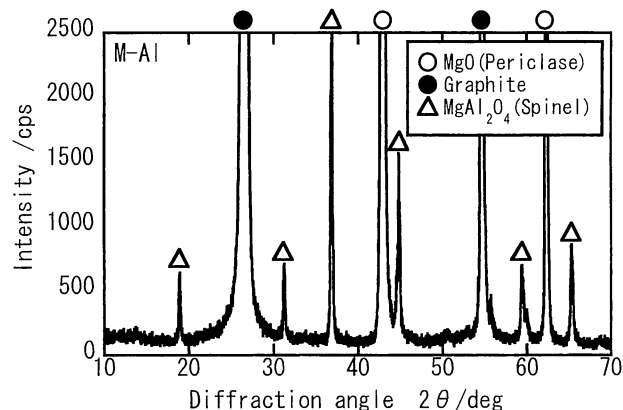


Fig. 5 X-ray diffraction pattern of M-Al sample after heating at 1600°C.

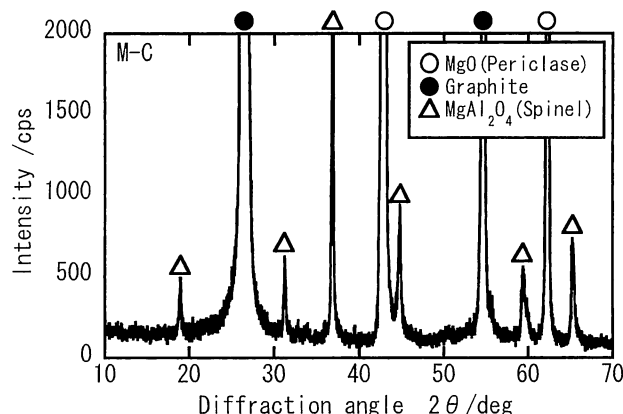


Fig. 6 X-ray diffraction pattern of M-C sample after heating at 1600°C.

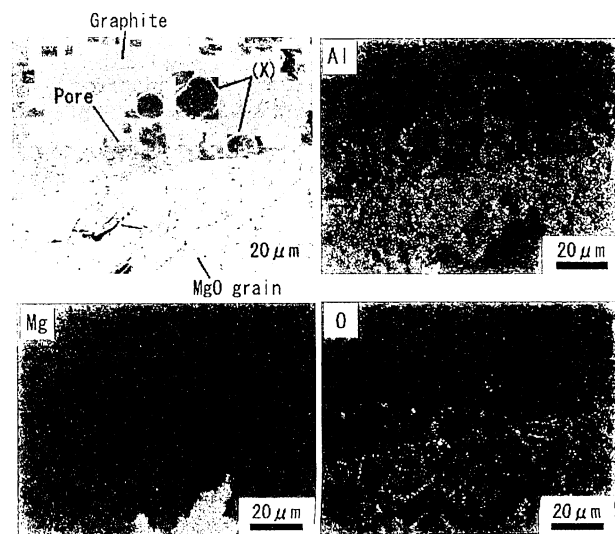


Fig. 7 EDS analysis of M-Al sample after heating at 1600°C (surface area of MgO grain).

brick specimens after heating at 1600°C. In the M-Al specimen, the peak (a) was observed at 8 to 14 μm pore diameter but in the M-C specimen such a peak was not present. Also, as for the median diameter of μ-fine pores, in the M-Al specimen the peak was observed at 2.1 μm and in the M-C specimen at 0.7 μm; therefore it can be concluded that the M-C specimen has a smaller pore diameter than M-Al.

4. Discussion

4.1 Pore Formation Mechanism

As shown in Figs. 7 and 8, the existence of pores adjacent to spinel was observed in both M-Al and M-C specimens after heating at 1600°C. Furthermore there was a clear tendency for the pore size to be larger in the vicinity of MgO grains and smaller among the graphite grains. The forming process of those pores can be considered as follows⁷⁾: Figure 10 illustrates a schematic drawing of a proposed model of pore formation in MgO-C brick with Al additive during heating at high temperature. Al metal powder added to MgO-C brick begins to melt when the temperature reaches the Al melting point of 600°C

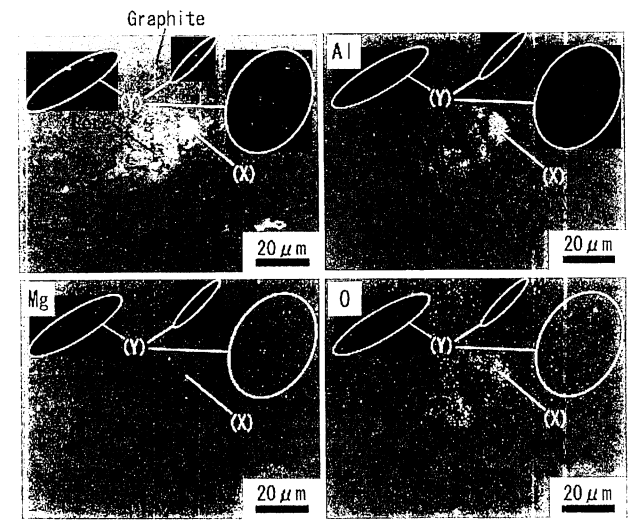


Fig. 8 EDS analysis of M-C sample after heating at 1600°C (graphite matrix area).

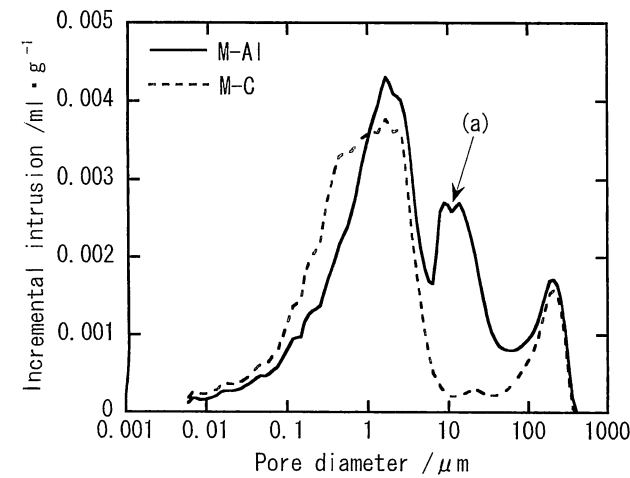


Fig. 9 Pore diameter distribution of MgO-C brick samples after heating at 1600°C.

and adjacent Al grains form consolidated bodies of melted Al. On the other hand in the case of Al grains adjacent to graphite grains, the Al forms an Al₄C₃ layer at about 700°C by reaction at the periphery of the Al according to Equation (1).



After formation of an Al₄C₃ layer, cracks generate on the surface of the Al₄C₃ layer because the volume expansion coefficient of Al-melt inside the Al₄C₃ layer is larger than that of Al₄C₃ layer. Then, considering the behavior of an Al grain under the condition of much higher temperature it is possible to think that the following phenomenon arises. Figure 11 shows the comparison of equilibrium partial pressures of Al gas phases volatilizing from metal Al (l) and that volatilizing from Al₄C₃ (s). The values of the ordinate axis in the figure are expressed by a normalized dimensionless number obtained by dividing by the standard state 0.1 MPa (representing by P⁰). It is possible to understand from the figure that the vapor pressure of Al (g) from Al (l) is higher than that of Al (g) from Al₄C₃, and therefore the Al (g) volatilizes preferentially from the Al (l), resulting in pores forming inside the Al₄C₃ layer. It is possible to estimate that

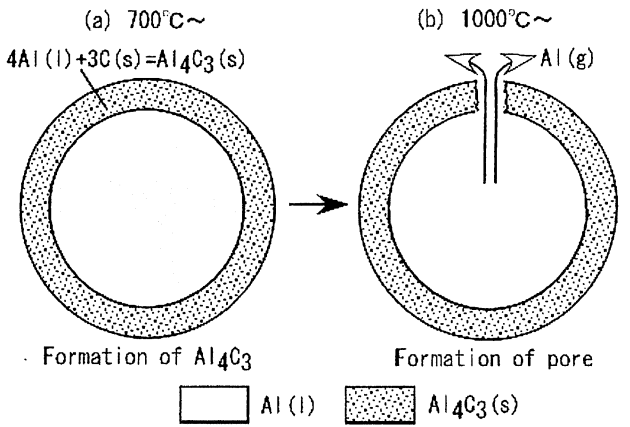


Fig. 10 A model of the pore formation in MgO-C brick with Al additive during heating.

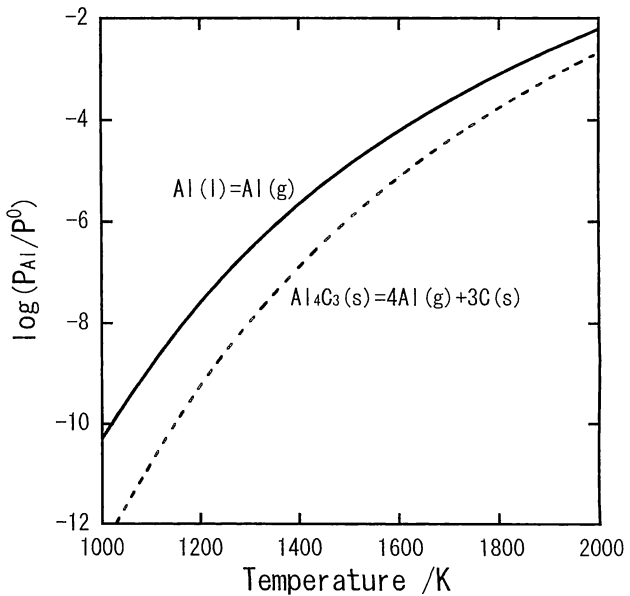


Fig. 11 Equilibrium partial pressure of Al gas (P⁰=0.1 MPa).

because Al (l) in the presence of carbon reacts to form Al_4C_3 , an Al_4C_3 layer is formed around Al (l) according to Equation (1), even if Al (l) liquid flows out through the breach of a crack.

Moreover the source of the difference in pore diameter between the M-Al and M-C specimens after heating can be considered as follows: Figure 12 shows schematic drawings for a proposed model of pore formation due to changes of Al grains within M-Al and M-C specimens during heating. In the M-Al specimen, some of the Al grains are contacting MgO grains and others are contacting graphite grains. During heating, Al_4C_3 (s) is formed where Al grains contact graphite grains by the reaction of Equation (1) while an oxidized film of Al_2O_3 is formed on the surface of Al grains where Al grains contact MgO grains. Though Al_4C_3 (s) grows up to about $20\text{ }\mu\text{m}$ in thickness⁷⁾, the thickness of the oxidized film seems to be extremely small. On the other hand, in the M-C specimen, because Al grains are surrounded by graphite grains, a $20\text{ }\mu\text{m}$ thick layer of Al_4C_3 (s) is formed around the entire periphery of the Al grains according to the reaction of Equation (1).

As mentioned above, it is possible to speculate that because the addition of Al grains to the M-Al specimen produced a smaller amount of Al_4C_3 (s) during heating compared with a similar addition to the M-C specimen, a lot of Al (l) is surviving within the M-Al specimen. Therefore it is possible to think that the pore diameter formed by Al volatilization becomes larger in the M-Al specimen after heating. Also, as seen in Fig. 2, in the M-Al specimen the Al grains are distributed together in groups at the periphery of MgO grains. For this reason, it is possible to make an assertive forecast that Al grains commingle on melting resulting in a larger diameter Al component. In this case much larger diameter pores may be formed if accompanied with volatilization of Al (l) at the same time. It can be concluded that the difference in pore diameter in Fig. 9 arose from the difference in distribution of Al grains that influenced the thickness of the Al_4C_3 layer formed and resulted in the difference in amount of Al (l) volatilization. Furthermore, it is possible to presume that the intensity of the pore diameter peak at (a) in the M-Al specimen became much larger as a result of commingling of Al particles on melting.

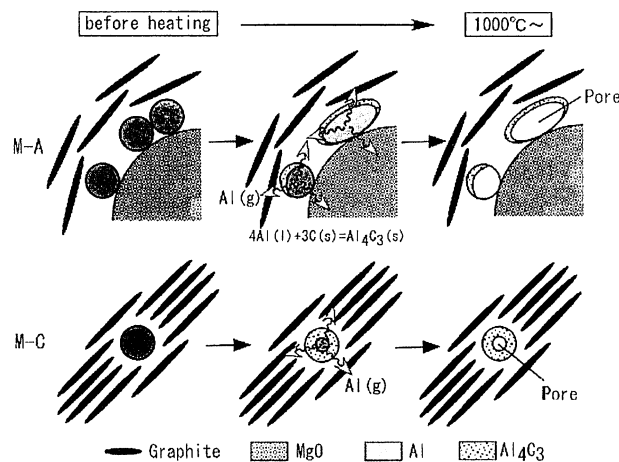


Fig. 12 A proposed model of the pore formation in M-Al and M-C samples during heating.

4.2 Formation Mechanism of Spinel

As seen in Figs. 7 and 8, coexisting regions of Mg, Al and O were observed in the structure after heating in both the M-Al and the M-C specimens. The spinel peaks of $(\text{MgAl}_2\text{O}_4)$ are identified by powder X ray diffraction analysis in Figs. 5 and 6, and therefore it is considered that the portion of coexisting Mg, Al and O may be spinel. In the case of MgO-C brick, the difference in formation mechanism and formation location of spinel due to distribution of Al powder can be thought of as follows: Figure 13 shows equilibrium partial pressures P_x of gases in the Mg-Al-C-O system coexisting with carbon at 1900 K and under conditions that (mol% Al/mol% Mg) is less than 2. In the same way as Fig. 11, the partial pressure is indicated by a dimensionless number normalized by dividing by the standard state 0.1 MPa (referred to as P^0). As shown in Fig. 11 there are various kinds of gaseous phases and among them Mg (g) in the Mg system and Al (g) in the Al system display the highest values in each system. Therefore it is possible to consider that the reactions occurring in the whole systems are only due to those two gaseous phases. In Fig. 13 changes of stable condensation phases corresponding with changes of CO partial pressure are also shown. From this information it is possible to understand that in the case CO partial pressure less than $[\log (P_{\text{CO}}/P_0) = -3.1]$ the system $[\text{Al}_4\text{C}_3 \text{ (s)} + \text{Mg (l)} + \text{C (s)}]$ is stable. In the case of CO partial pressure in the range $[\log (P_{\text{CO}}/P_0) = -3.1 \text{ to } -2.2]$, the system $[\text{Al}_4\text{C}_3 \text{ (s)} + \text{MgO (s)} + \text{C (s)}]$ is stable, and in the case of CO partial pressure more than $[\log (P_{\text{CO}}/P_0) = -2.2]$, the system $[\text{MgAl}_2\text{O}_4 \text{ (s)} + \text{MgO (s)} + \text{C (s)}]$ is stable. It also shows that the stable coexistence of carbon and Al (l) is impossible and all the Al (l) becomes Al_4C_3 . By the way, CO partial pressure in carbon containing refractories at high temperature is thought to be about at 0.1 MPa ⁸⁾, but in the

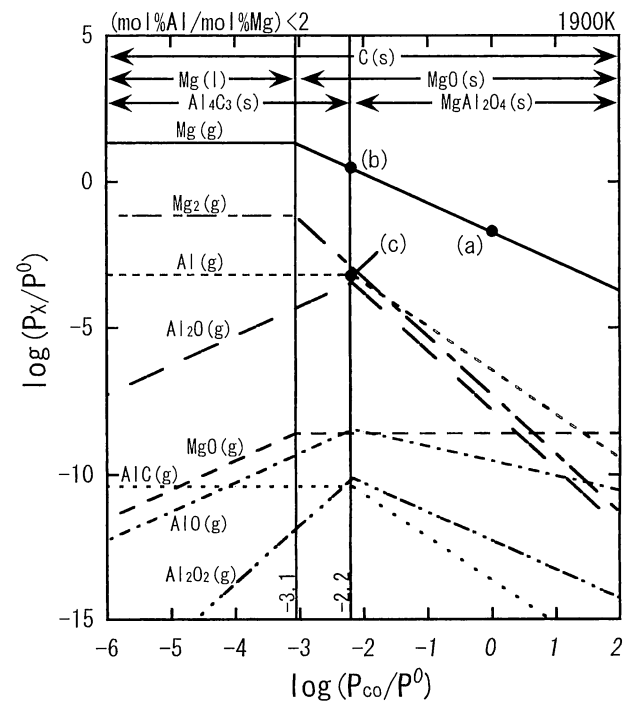
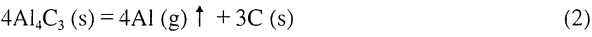
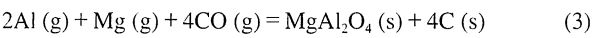


Fig. 13 Equilibrium partial pressures of gases in the Mg-Al-C-O system ($P^0=0.1\text{ MPa}$).

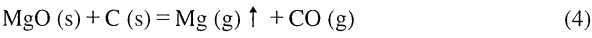
vicinity of the surface of Al_4C_3 grains the CO partial pressure maintains at approximately $[\log (P_{\text{CO}}/P_{\text{O}}) = -2.2]$, which is the lower rather than the value of the circumference. Under these conditions, the Al (g) vapor is generated mainly from the surface of Al_4C_3 and it diffuses into the structure possessing a higher CO partial pressure. The reaction can be expressed by Equation (2). In proportion to diffusion of Al (g) into the structure possessing high CO partial pressure, MgAl_2O_4 (s) begins to deposit in succession to Al_4C_3 .



As for the formation of MgAl_2O_4 (s) in the Mg-Al-C-O system, various reaction mechanisms are possible, of which authors especially discuss the reactions among three gaseous phases; Al (g), Mg (g) and CO (g) shown in Equation (3) because Al, Mg and O coexist in voids among graphite grains as shown in Figs. 7 and 8.

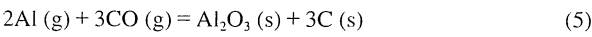


Mg (g) of this reaction is generated from MgO grains according to the reaction of Equation (4).



It is possible to consider the behavior of the generated Mg (g), as follows: The equilibrium partial pressure of Mg (g) against the partial pressure of CO (g) can be expressed as $[\log (P_{\text{Mg}}/P_{\text{O}}) = -1.7]$ (point [a] in Fig. 13) under the condition that the partial pressure of CO is 0.1 MPa. But it becomes $[\log (P_{\text{Mg}}/P_{\text{O}}) = 0.4]$ (point [b] in Fig. 13) under the condition of the partial pressure of CO at $[\log (P_{\text{CO}}/P_{\text{O}}) = -2.2]$, so that Al_4C_3 (s) is a stable phase. In other words, it is possible to understand that for the CO partial pressure such that Al_4C_3 (s) may be stable, the Mg (g) partial pressure becomes higher. Consequently Mg (g) generated from MgO grains diffuses toward circumference of Al_4C_3 (s) that isn't filled up with Mg (g) and the Mg (g) partial pressure is high. On the other hand, as for the behavior of Al (g) generated from Al_4C_3 (s) going along with Equation (2) it is possible to consider as below:

The partial pressure of Al (g) generated from Al_4C_3 (s) is at $[\log (P_{\text{Al}}/P_{\text{O}}) = -3.2]$ (point [c] in Fig. 13), but in the region where the circumferential CO partial pressure is higher the partial pressure of Al (g) becomes lower. Consequently Al (g) volatilized from Al_4C_3 (s) is condensed at the vicinity of Al_4C_3 (s) according to the reaction of Equation (5) and forms spinel going along with Equation (3) when Mg (g) is present.



In other words, Mg (g) generated from MgO grains diffuses toward the circumference of Al_4C_3 (s) while Al (g) generated from Al_4C_3 (s) condenses in the vicinity of Al_4C_3 (s) and therefore it is possible to think that the condensation reaction of spinel by Equation (3) becomes easy in the vicinity of Al_4C_3 (s).

MgAl_2O_4 (s) is found at the circumference of pores and among graphite grains around the pores in Figs. 7 and 8. Pores are formed from Al_4C_3 (s) reaction products by Equation (1) and

volatilization of Al (l) occurs within the interior of the Al_4C_3 (s) as mentioned in the previous section. Therefore the figures verify the evidence that the condensation reaction of spinel due to Equation (3) occurred in the vicinity and at the circumference of Al_4C_3 (s). The routing line that Mg (g) generated from MgO grains and Al (g) generated from Al_4C_3 (s) diffuse into the structure is thought to act as a continuous pore within the structure and that the places where these gases condense also locate in a continuous pore within the structure. In other words, Al (g) and Mg (g) diffuse into pores, condense as spinel as well as form carbon, resulting in filling up almost of all the voids mainly in the vicinity of Al_4C_3 .

It was also observed that MgAl_2O_4 formed in the vicinity of the surface of MgO grains in M-Al in which MgO grains and Al powder are contacting each other according to the result of Fig. 7. This is possible to explain as below: because CO partial pressure becomes lower as $[\log (P_{\text{CO}}/P_{\text{O}}) = -2.2]$ in the vicinity of Al_4C_3 as seen in Fig. 13, the partial pressure of Mg (g) generated from MgO grains existing in the neighborhood increases up to $[\log (P_{\text{Mg}}/P_{\text{O}}) = 0.4]$ (point [b] in Fig. 13). Also in M-Al, a lot of the molten Al (l) survives within Al_4C_3 (s) layer and therefore it is possible to infer that Al (g) is generated from Al (l) as well as Al_4C_3 (s). The partial pressure of Al (g) generated from Al (l) is higher than the vapor pressure generated from Al_4C_3 (s) as seen in Fig. 11. Therefore it is possible to conclude that in the case of the M-Al specimens the partial pressures of both Mg (g) and Al (g) become extremely high in the vicinity of the surface of MgO grains, and in the case of such high vapor pressure, the mutual diffusion between Mg (g) and Al (g) is occurs resulting in formation of a large amount of spinel in the vicinity of surface of MgO grains.

Figure 14 shows a schematic drawing of a proposed model for spinel formation in both M-Al and M-C specimens during the heating process. For the sake of simplification, graphite grains are omitted in the diagrammatic representation. In the M-Al specimen, the formation of spinel was concentrated in the vicinity of the surface of MgO grains but in the M-C specimen, spinel was produced widely among graphite grains in the brick structure. It is desirable to form spinel uniformly in the structure by distributing Al powder homogeneously among graphite grains in order to accelerate the densification of the structure by forming spinel in the voids within the structure.

4.3 Relation Between Distribution of Al Powder and Characteristics

It became clarified that varying the distribution morphology of Al powder exercises an influence on the pore size and location of spinel formation. If the bricks require especially high strength during high temperature operation or after operation, it is desirable that the size of pores formed by heating is small. Also, because spinel formed at high temperature densifies the structure and contributes to the development of high strength¹⁾, it is essential to form the spinel homogeneously through the entire brick structure. In other words, it is most effective to add Al powder to the system so that the formed pore size is as small as

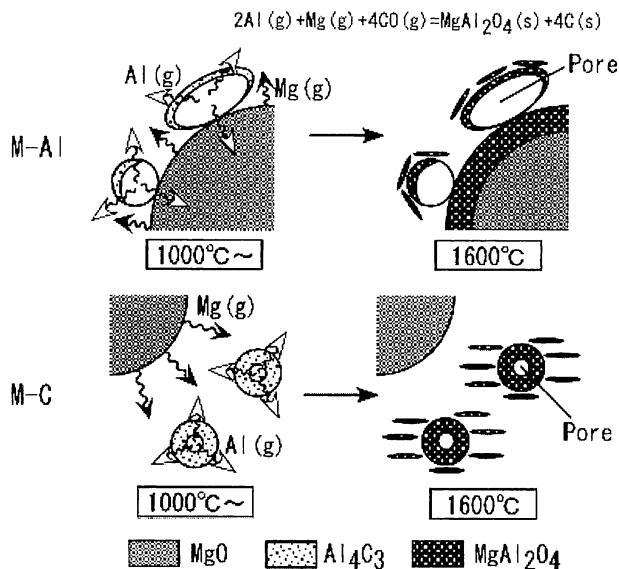


Fig. 14 A proposed model for formation of MgAl_2O_4 in M-Al and M-C during heating.

possible and spinel is produced widely through the entire structure. Spinel is formed in the vicinity of Al_4C_3 generated through the reaction between Al powder and graphite grains. Consequently, distributing the Al powder as widely as possible among the graphite grains makes a considerable contribution to the homogeneous formation of spinel through the entire structure. As shown in Fig. 4, the M-C specimen with Al powder distributed widely among the graphite grains resulted in higher strength than that of the M-Al specimen after heating. This phenomenon provides substantiation that M-C specimen produced a large amount of spinel widely among graphite grains and attained a densified structure compared with the M-Al specimen. Furthermore on the occasion when Al powder exists in close association with graphite, thicker Al_4C_3 is formed and smaller pores are produced. The results of Fig. 9 establish obvious proof that the method to distribute Al powder widely among graphite grains brings about the formation of smaller pores after heating.

5. Conclusions

As a result of investigating the most effective addition method of Al metal powder to MgO-C bricks, the following knowledge was obtained:

- (1) In the case of adding Al powder that is well dispersed among graphite grains, the reaction between Al powder and graphite progresses during heating and a thicker Al_4C_3 layer is formed in the peripheral portion of an Al grain and therefore the amount of the residual Al (l) becomes less. In the result, the pore formed in the residual Al_4C_3 after volatilizing Al (l) is remarkably small.
- (2) Spinel formed by sintering is produced extensively in the vicinity of Al_4C_3 and is generated by reaction between Al powder and graphite. Therefore, in the case of dispersing Al powder widely within the graphite grains, spinel is homogeneously produced in the voids among the graphite grains. As a result it is possible to obtain products possessing a dense structure and high strength after heating.

References

- 1) Akira Watanabe, Hirokuni Takahashi, Shigeyuki Takanaga, Nobuo Goto, Kenji Anan and Mineo Uchida: *Taikabutsu*, 38, [11] pp740-746 (1986)
- 2) Akira Yamaguchi: *Taikabutsu*, 35, [11] pp617-622 (1983)
- 3) S. Zhang, N. J. Marriott and W. E. Lee: *J. Eur. Ceram. Soc.*, 21, pp1037-1047 (2001)
- 4) S. Zhang and W. E. Lee: *J. Eur. Ceram. Soc.*, 21, pp2393-2405 (2001)
- 5) C. G. Aneziris, J. Hubalkova and R. Barabas: *J. Eur. Ceram. Soc.*, 27, pp73-78 (2007)
- 6) Akira Yamaguchi and Jingkun Yu: *Taikabutsu*, 44, [12] pp700-707 (1992)
- 7) Jingkun Yu and Akira Yamaguchi: *J. Ceram. Soc. Japan*, 101, [4], pp475-479 (1993)
- 8) Akira Yamaguchi: *Taikabutsu*, 35, [7] pp65-370 (1983)

Translated from *Taikabutsu* 62 [7] 339-345 (2010)

Report

Effect of Adding Al₄O₄C to Carbon-Containing Refractories

Yasuhiro HOSHIYAMA and Akira YAMAGUCHI

Key words: Carbon-containing refractories, Al₄O₄C, Reaction, Densification

1. Introduction

Metallic Al is added to carbon-containing refractories such as MgO-C brick and Al₂O₃-C brick to prevent the oxidation of carbon. Metallic Al reacts with C and CO existing in the brick to make the structure dense and increase the strength at high temperature. Metallic Al gives a large effect on improvement in the service life. However, its field application is restricted to the case that there is no hydration reaction; namely, that there is no water vapor present at a low temperature because Al₄C₃ that is generated by the reaction of metallic Al with C and CO is easily hydrated and deteriorates the brick structure. Therefore, metallic Al has a weak point as an additive in that it cannot be used as an antioxidant in refractory castables.

Al₄O₄C is anticipated as a possible material to solve the above mentioned problems¹⁻³⁾. It is assumed that Al₄O₄C has a high resistance against a hydration, has a densification effect equal to metallic Al and does not form Al₄C₃ in any reaction process¹⁾. Therefore, the application of Al₄O₄C instead of metallic Al to carbon-containing bricks and castable refractories may improve their performance²⁾. Furthermore, compared with Al₄SiC₄ and other additives, Al₄O₄C may be more widely applicable because it does not contain any metallic elements except Al.

This paper presents the results of an investigation on the application of Al₄O₄C to MgO-C and Al₂O₃-C brick, typical carbon-containing refractories.

2. Preparation of Al₄O₄C Powder

Al₄O₄C powder was prepared as follows⁴⁾: The raw materials were alumina, metallic aluminum and carbon powders. The alumina powder was α-Al₂O₃ with 0.2 μm average diameter and purity of 99.9%. The aluminum powder had 30 μm average diameter (maxim 63 μm) and purity of 99.8% while the flake graphite was 99% pure with a maximum particle size of 75 μm.

Raw materials in the proportions shown in Table 1 were mixed in a dry ball mill for 10 hours and put in a graphite crucible. The graphite crucible was placed in a vessel type carbon furnace and fired. The carbon furnace was evacuated with a vacuum pump and argon gas was flowed into it at a flow rate of 1 liter per minute while heating. The temperature was elevated to 1700°C at 10°C per minute and held at temperature for 1 hour. The mixture was cooled naturally in the carbon furnace. The

Table 1 Particle size and mixing ratio of raw materials for preparing Al₄O₄C

Raw materials	Size of particle	Mixing ratio (mass%)
α-Al ₂ O ₃	Av. 0.2 μm	73.9
Al powder	Under 63 μm	19.6
Flake graphite	Under 75 μm	6.5

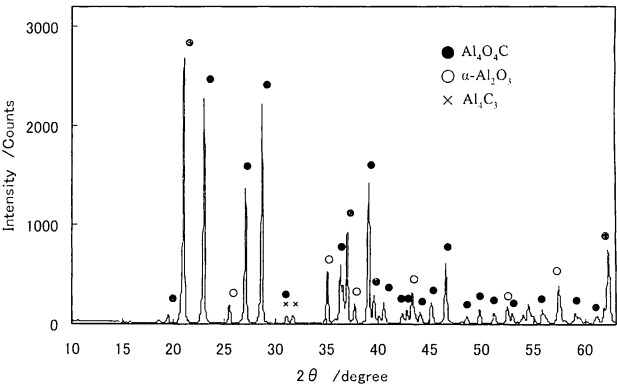


Fig.1 X-ray powder diffraction pattern of synthesized Al₄O₄C.

heat treated mixture obtained by the above procedure was ground in a dry ball mill for 10 hours to a fine powder with a particle size of 50 μm and less. (The average diameter was about 20 μm). Figure 1 shows the X-ray powder diffraction pattern of the synthesized Al₄O₄C.

3. Application of Al₄O₄C to MgO-C Brick

3.1 Preparation of Al₄O₄C-added MgO-C Brick

The effects of Al₄O₄C on the performance of MgO-C brick were evaluated in comparison to those containing metallic Al, the conventional antioxidant, and to those containing no antioxidant. Table 2 shows compositions of the MgO-C test samples. The MgO-C test samples can be divided into two groups with different proportions of MgO and C; namely, a group composed of samples No. 1~No. 4 with 5 mass% C and another group composed of samples No. 5~No. 8 with 15 mass% C. Each group contains a test sample with no antioxidant, one with metallic Al and two with different levels of Al₄O₄C. The contents of elemental Al in samples No. 4 and No. 8 are equal to the metallic Al contents in samples No. 2 and No. 6.

Each mixture was kneaded and shaped with a uniaxial

Effect of Adding Al₄O₄C to Carbon-Containing Refractories

Table 2 Composition of MgO-C samples (mass %)

No.	1	2	3	4	5	6	7	8
Fused MgO - 1 mm	65				60			
- 75 μm	30				25			
Flake graphite - 150 μm	5				15			
Al 30 μm		ex.4				ex.4		
Al ₄ O ₄ C 20 μm			ex.4	ex.6.82			ex.4	ex.6.82
Phenol resin	ex.3				ex.4			
Hexamethylenetetramine	ex.0.3				ex.0.4			

pressing machine under 150 MPa of pressure to form a green body. The green body was heated at 200℃ for 12 hours to form an unburned test sample. The test samples were fired in a reducing atmosphere similar to that in field operations and changes in physical properties including the change in mass were measured. The above mentioned reducing firing procedure was as follows: An unburned test sample was buried in graphite powder and fired in air in an electric furnace at prescribed temperatures between 800℃ and 1500℃ for 3 hours.

The resistance against oxidation was evaluated by measuring the thickness of the oxidized layer when each unburned test sample (ca 25 × 25 × 25 mm) was heated in an electric furnace in air. An unburned test piece was put in the electric furnace, heated up to 1300℃ or 1500℃ at a heating rate of 10℃ per minute, held for 3 hours and naturally cooled in the electric furnace. The thickness of the oxidized layer was measured at the cross section cut at the center of the test piece.

3.2 Results

Figure 2 shows the relation between the change in mass and the heating temperature when the unburned test samples were fired in the reducing atmosphere. The decrease in the mass at 800℃ is due to the thermal decomposition of the phenol resin binder that is almost complete at 800℃, and changes in the mass at temperatures higher than 800℃ are caused by some reaction in the test samples. The decrease in the mass of MgO-C test samples No. 2 and No. 6 with metallic Al and heated at 800℃ are the smallest among the test samples. Specimens 2 and 6 heated to 1000℃ showed significant mass increase from the 800℃ value. The mass of MgO-C test pieces Nos. 3, 4, 7 and 8

with added Al₄O₄C increased from their 800℃ values on heating in the range 1000℃ to 1400℃. This fact indicates that some reaction causing the increase in the mass progresses while MgO-C test samples containing Al₄O₄C are heated in carbon powder.

Figure 3 shows the relation between the apparent porosity and the heating temperature when the unburned test sample was fired in the reducing atmosphere. The increase in apparent porosity from the cured state at 200℃ to 800℃ is due to the thermal decomposition of phenol resin. Both the apparent porosity of test samples No. 1 and No. 5 containing no Al element increase in the temperature range higher than 800℃ as the heating temperature rises. Both the apparent porosity of test samples No. 2 and No. 6 with metallic Al added decreased when the heating temperature was 1000℃. The apparent porosities of all the Al₄O₄C-added test samples heated at temperatures higher than 800℃ were larger than those of test samples containing no Al element.

It is clear that the structure of test samples with added Al₄O₄C was not densified by the reaction that increased its mass because the apparent porosity did not decrease despite the fact that the mass increased on heating in the range from 1000℃ to 1400℃ (see Fig. 2).

Figure 4 shows the oxidation test results for the MgO-C samples. The oxidized thickness of test pieces containing 5% C with no antioxidant or with Al₄O₄C-added was 12.5 mm after heating at 1300℃ or 1400℃. On the other hand, the oxidized thickness of the specimens with 4 mass% Al metal addition was about 2 mm for both heating temperatures. The oxidized thicknesses on the specimens containing 15 mass% C followed

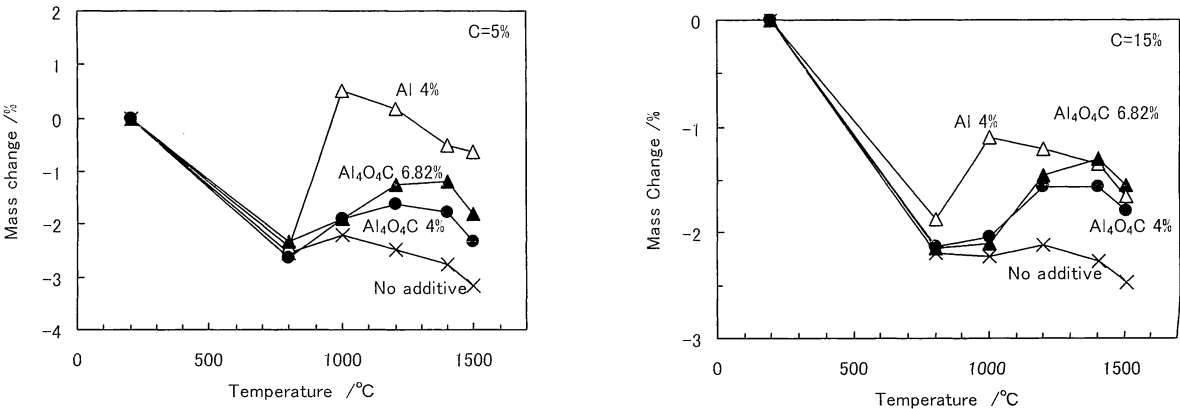


Fig. 2 Relation between mass change and heating temperature in reducing atmosphere of MgO-C unburned test samples.

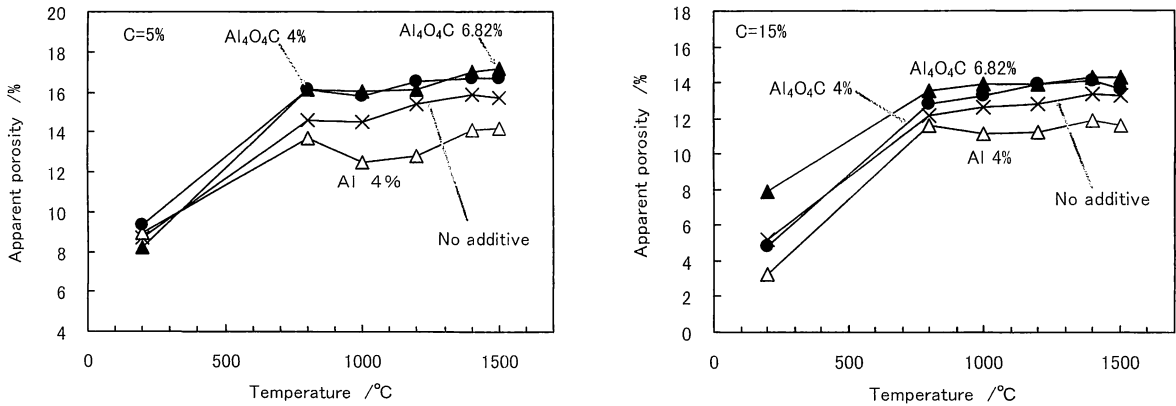


Fig. 3 Relation between apparent porosity and heating temperature of MgO-C unburned test samples.

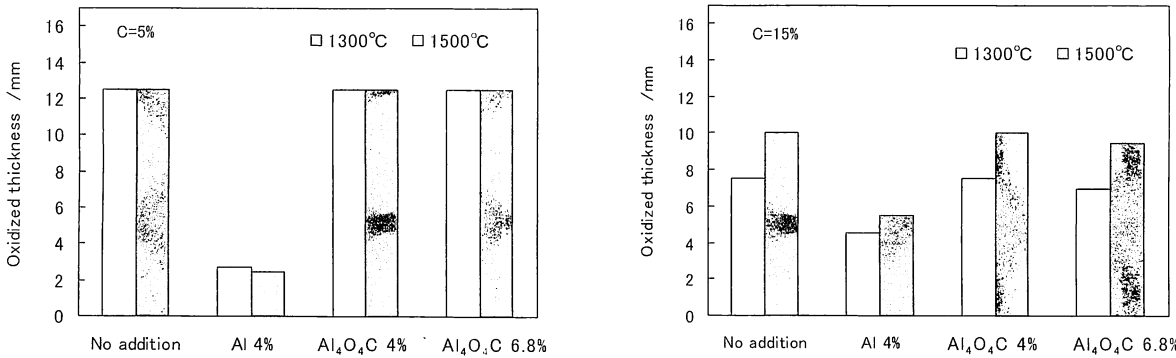


Fig. 4 Oxidized thickness of MgO-C test samples.

a similar trend but were considerably less. Regardless of the difference in the amount of graphite, the oxidation thickness of Al₄O₄C containing samples was larger than that of samples with metallic Al added and equal to that of test samples containing no Al. The results in Fig. 4 show that the addition of even 4 mass% Al as Al₄O₄C has a negligible effect on improving the oxidation resistance and that the addition of Al metal is more effective.

4. Application of Al₄O₄C to Al₂O₃-C Brick

The effect of Al₄O₄C on the oxidation resistance of Al₂O₃-C brick was investigated. A test sample containing a large amount of Al₄O₄C (25 mass%) was prepared because, as mentioned above, 4 mass% was too little to improve the oxidation resistance in MgO-C specimens.

4.1 Water Treatment of Al₄O₄C Powder

Prior to the experiment of adding a large amount of Al₄O₄C, a water treatment of Al₄O₄C powder was carried out to hydrate the slight amount of Al₄C₃ contained in Al₄O₄C, because it is assumed that Al₄C₃ reacts with water to degrade the packing density of Al₂O₃-C brick containing Al₄O₄C

One hundred grams of Al₄O₄C of composition shown in Table 1 was put in a beaker with water, stirred a little and left for one week in room conditions. Figure 5 shows the change in appearance of the sample. The original powder with a pale whitish-yellow-green color changed to a whitish swelled powder. The whitish swelled powder was dried at 110°C for 10 hours and crystal phases were identified by X-ray powder diffraction.

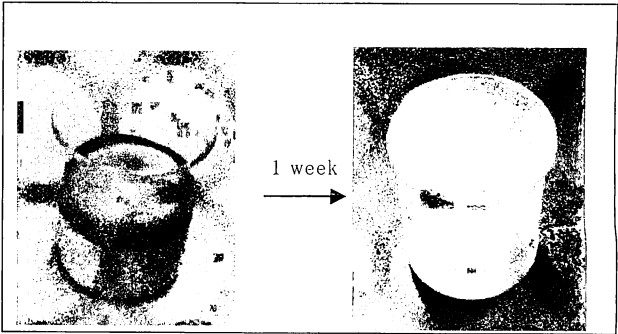


Fig.5 Change in appearance of Al₄O₄C powder by treatment with water.

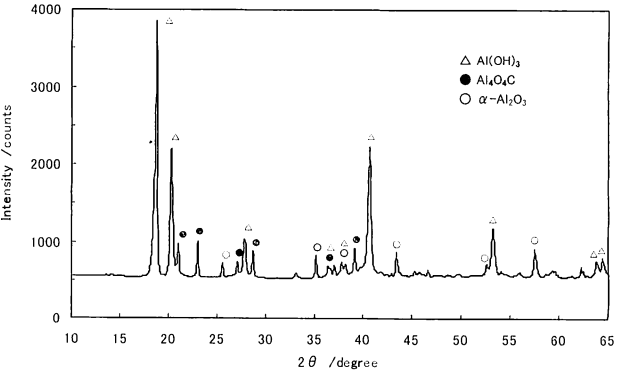


Fig.6 X-ray powder diffraction pattern of swelled Al₄O₄C powder

Figure 6 shows that Al₄O₄C substantially decreased and a large amount of Al(OH)₃ was generated. This fact suggests that it is difficult to apply Al₄O₄C to castable refractories because the

Effect of Adding Al₄O₄C to Carbon-Containing Refractories

beaker test clarified that the hydration of Al₄O₄C progresses at room temperature when Al₄O₄C is put in water for a long time. Therefore, it was decided to use Al₄O₄C shown in Fig. 1 without the water treatment.

4.2 Preparation of Al₄O₄C-added Al₂O₃-C Brick

Table 3 shows the compositions of Al₂O₃-C test samples. In test sample No. 11 the entire amount of 75 μm grain size fused Al₂O₃ in test sample No. 9 was replaced with Al₄O₄C. Each mixture with the compositions shown in Table 3 was kneaded and shaped with a uniaxial pressing machine under 150 MPa pressure to a green body. The green body was heated at 200°C for 12 hours to form an unburned test sample. The unburned test sample was fired in reducing atmosphere equal to an actual operating atmosphere and physical properties were measured. The above mentioned reduction firing procedure was as follows: An unburned test sample was buried in graphite powder and fired in air in an electric furnace at prescribed temperatures of 800°C to 1500°C for 3 hours.

4.3 Results

Figure 7 shows the length and the bulk density of each unburned test sample after curing at 200°C. The length of the test sample No. 11 containing 25 mass% Al₄O₄C was greater than that of samples No. 9 and 10 that did not contain any Al₄O₄C.

Table 3 Composition of Al₂O₃-C samples (mass %)

No.	9	10	11
Fused Al ₂ O ₃ - 1mm	60	60	60
- 75 μm	25	25	
Flake graphite - 150 μm	15		
Al 30 μm		ex.5	
Al ₄ O ₄ C 20 μm			25
Phenol resin	ex.4		
Hexamethylenetetramine	ex.0.4		

Furthermore, the bulk density of No. 11 was smaller than that of Nos. 9 or 10. These facts can be understood from results shown in Figs. 5 and 6. Namely, these facts suggest the possibility that water vapor generated by the thermal hardening reaction of phenol resin hydrated the Al₄O₄C resulting in the swelling of specimen No. 11. It is assumed that hydration swelling of Al₄O₄C added to MgO-C samples also occurred, but swelling of the specimen was not observed because the addition amount was small.

Figure 8 shows the change in the mass with heating when the unburned test samples were fired in reducing atmosphere. The decrease in the mass at 800°C is primarily due to the thermal decomposition of the phenol resin binder that is almost complete at 800°C. Other changes in the mass at temperatures above

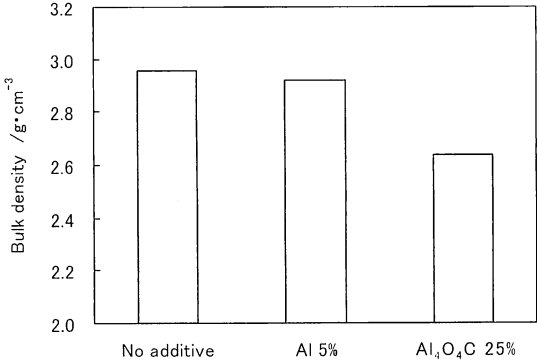
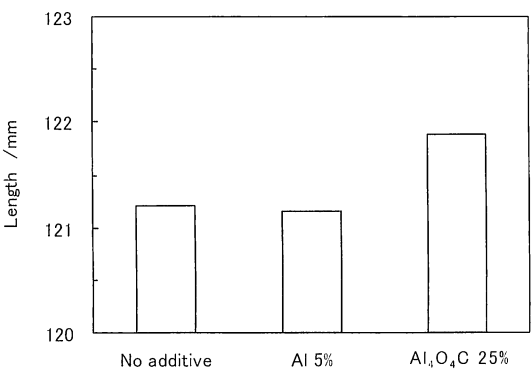


Fig. 7 Length and bulk density of Al₂O₃-C unburned test samples obtained by heating green test samples at 200°C for 12 hours.

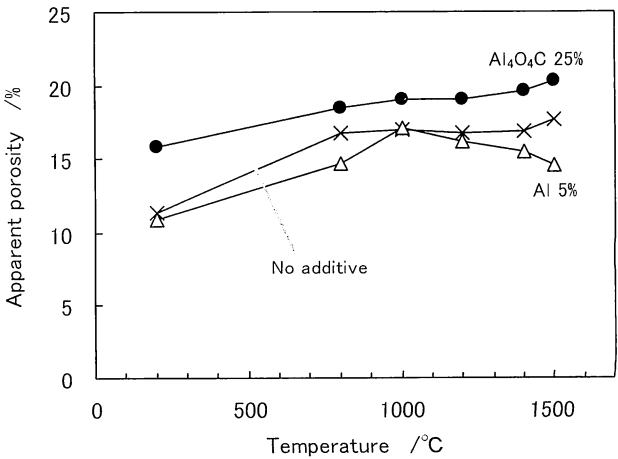
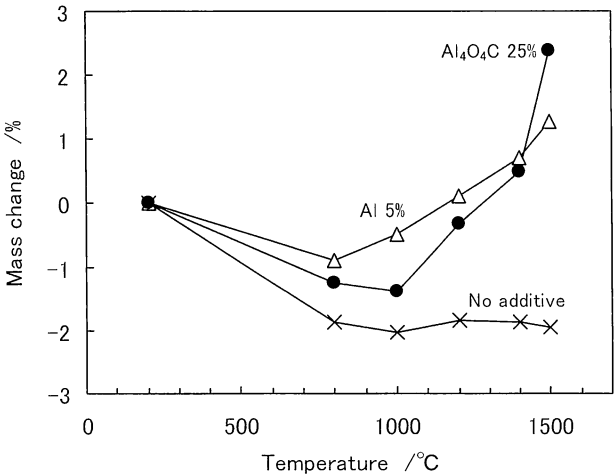


Fig. 8 Relation between relative mass change and heating temperature in reducing atmosphere of Al₂O₃-C test sample.

Fig. 9 Relation between apparent porosity and heating temperature in reducing atmosphere of Al₂O₃-C test sample.

800℃ were caused by some reaction in the test sample. The decrease in the mass of test samples containing $\text{Al}_4\text{O}_4\text{C}$ and that containing metallic Al was smaller than that of the test sample containing no additive, and their mass largely increased as the heating temperature rises. These results again clearly prove that some reaction with a mass gain progresses in the test sample containing $\text{Al}_4\text{O}_4\text{C}$ when it is heated in carbon powder at 1000℃ and higher.

Figure 9 shows the change in the apparent porosity with the heating temperature when the test samples were fired in reducing atmosphere.

The apparent porosity of the test sample No. 10 containing metallic Al decreased in the high temperature range; namely, its structure was densified. On the other hand, the apparent porosity of the test sample No. 11 containing $\text{Al}_4\text{O}_4\text{C}$ did not decrease; namely, a densification effect was not observed. By the way, all values of apparent porosity of the samples containing 25 mass% $\text{Al}_4\text{O}_4\text{C}$ were larger than those of the test sample No. 9 with no additive and No. 10 containing metallic Al.

Figure 10 shows the change in cold crushing strength with firing temperature when $\text{Al}_2\text{O}_3\text{-C}$ test samples were fired in reducing atmosphere. The cold crushing strength of $\text{Al}_2\text{O}_3\text{-C}$ test samples with no addition and with $\text{Al}_4\text{O}_4\text{C}$ -addition were smaller at all firing temperatures than those with metallic Al. However, the cold crushing strength of $\text{Al}_4\text{O}_4\text{C}$ -added $\text{Al}_2\text{O}_3\text{-C}$ test samples tended to increase at firing temperatures higher than 1200℃.

It was clarified that a large amount of $\text{Al}_4\text{O}_4\text{C}$ addition (25%) made the apparent porosity of the $\text{Al}_2\text{O}_3\text{-C}$ body large and its cold crushing strength low. The reasons for this can be considered that water generated while the green body was heated at 200℃ for 12 hours reacted with $\text{Al}_4\text{O}_4\text{C}$ to form hydrates causing swelling and making the apparent porosity large and that the $\text{Al}_4\text{O}_4\text{C}$ did not promote the densification of the $\text{Al}_2\text{O}_3\text{-C}$ fired test sample although the reaction of $\text{Al}_4\text{O}_4\text{C}$ progressed. The present conclusion is that the application of $\text{Al}_4\text{O}_4\text{C}$ to carbon-containing $\text{Al}_2\text{O}_3\text{-C}$ refractories is not effective, because the above mentioned results are the same as those obtained for $\text{Al}_4\text{O}_4\text{C}$ -added MgO-C samples.

5. Discussion

$\text{Al}_4\text{O}_4\text{C}$ added to carbon-containing refractories did not densify their structures, although a reaction of the $\text{Al}_4\text{O}_4\text{C}$ caused an increase in the mass while firing at high temperatures. The authors considered reasons for this behavior because this phenomenon may be important for investigating the application non-oxides to refractories. It is assumed that the reaction of

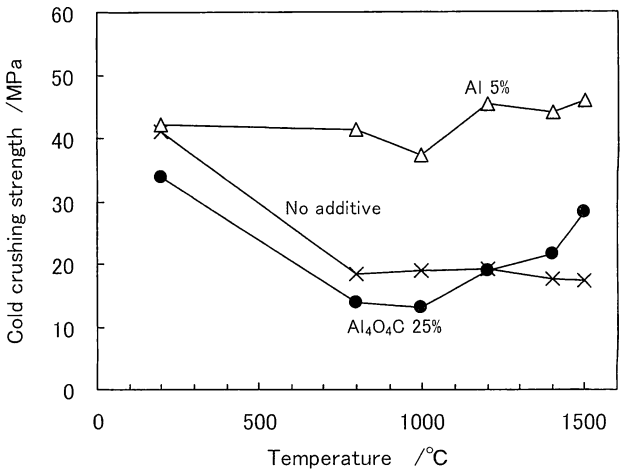
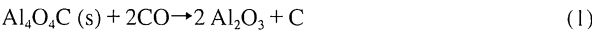


Fig.10 Relation between cold crushing strength and firing temperature in reducing atmosphere of $\text{Al}_2\text{O}_3\text{-C}$ test samples.

$\text{Al}_4\text{O}_4\text{C}$ at high temperatures is expressed by Equation (1)¹⁾ because the inside of a carbon-containing refractory is filled with CO gas at temperatures higher than 1000℃⁵⁾.



Equation (1) makes the weight larger because $\text{Al}_4\text{O}_4\text{C}$ reacts with CO to form Al_2O_3 and C.

Whether the structure of a refractory is densified or not can be determined by calculating the change in volume in Equation (1). The true density of $\text{Al}_4\text{O}_4\text{C}$ powder was determined first because the true density of every material in the reaction is necessary for calculating a volume change. $\text{Al}_4\text{O}_4\text{C}$ used for this investigation was ground to a fine powder, and the true density was measured with the gas volume method. The value obtained was $2.86\text{ g}\cdot\text{cm}^{-3}$. However, $\text{Al}_4\text{O}_4\text{C}$ powder contains some $\alpha\text{-Al}_2\text{O}_3$ and Al_4C_3 as shown in Fig. 1. Supposing the content of $\alpha\text{-Al}_2\text{O}_3$ is 10 mass% and Al_4C_3 is 5 mass%, the measured powder true density was adjusted for these phases and the true density of pure $\text{Al}_4\text{O}_4\text{C}$ was calculated in order to ensure accuracy. The value obtained was $2.76\text{ g}\cdot\text{cm}^{-3}$. Using this value, the change in volume of Equation (1) was calculated to be +10.5%. This value is extremely small in comparison with the change of volume in the reaction of Al with CO (+122.7%) and that of Al_4SiC_4 with CO (+115.9%) as shown in Table 4.

A. Yamaguchi reported that metallic Al in carbon-containing refractories changes to Al_4C_3 and AlN at high temperatures, finally, the reaction shown in Table 4 makes a structure dense⁶⁾. Y. Hoshiyama et al stated that the densification effect of Al_4SiC_4 was large, and proposed the densification mechanism that reaction products deposited in gaps through the vaporization-

Table 4 Calculation results of volume change by reaction

Reaction formula	Volume change※/%
$\text{Al}_4\text{O}_4\text{C(s)} + 2\text{CO(g)} = 2\text{Al}_2\text{O}_3\text{(s)} + 3\text{C(s)}$	+ 10.5
$2\text{Al(l)} + 3\text{CO(g)} = \text{Al}_2\text{O}_3\text{(s)} + 3\text{C(s)}$	+122.7
$\text{Al}_4\text{SiC}_4\text{(s)} + 6\text{CO(g)} = 2\text{Al}_2\text{O}_3\text{(s)} + \text{SiC(s)} + 9\text{C(s)}$	+115.9

※Calculated with following bulk density ($\text{g}\cdot\text{cm}^{-3}$)
 $\text{Al}_4\text{O}_4\text{C} : 2.76 \quad \text{Al}_4\text{SiC}_4 : 3.00 \quad \text{Al}_2\text{O}_3 : 3.99 \quad \text{Al} : 2.50 \quad \text{SiC} : 3.22 \quad \text{C} : 1.60$

Effect of Adding Al_4O_4C to Carbon-Containing Refractories

condensation mechanism causing a large volume expansion⁷⁾. By the way, the calculation of Al_4O_4C reaction states that the sufficient effect for decreasing gaps cannot be obtained although even the reaction of Al_4O_4C with CO increases the volume.

In the case of Equation (1), it is clear that the conditions for making the porosity of refractories small cannot be obtained because of the fact that the increase ratio of the volume is small. Even if products of Equation (1) deposit in gaps through the vaporization-condensation process, the space occupied with Al_4O_4C particles remains as vacancy.

It can be said from the above mentioned discussion that Al_4O_4C has a small densification effect being one of elemental specific properties.

6. Conclusions

Using MgO-C brick and Al_2O_3 -C brick, the effect of Al_4O_4C on the performance of carbon-containing bricks was investigated. The results are as follows.

- (1) The mass of MgO-C brick containing 4~7 mass% of Al_4O_4C increased in the temperature range 1000°C to 1400°C, but the apparent porosity did not decrease.
- (2) The hydration of Al_4O_4C progressed when it was put in water for a long time.
- (3) The mass of Al_2O_3 -C brick containing 25 mass% Al_4O_4C

clearly increased in the temperature range 1000°C to 1400°C, but the apparent porosity did not decrease.

- (4) The change in volume of Al_4O_4C in the high temperature reaction was estimated as + 10.5%.

It can be said that the effect of Al_4O_4C addition is smaller than that of metallic Al, but it has merit that it does not generate Al_4C_3 . Therefore, application techniques taking advantage of this feature should be developed.

References

- 1) S. Zhang, A. Yamaguchi, *J. Ceram. Soc. Japan*, 104 [5] 393-398 (1996)
- 2) Jianli Zhao, Wei Lin, Akira Yamaguchi, Junji Onmyoji and Jialin Sun, *Taikabutsu*, 59 [6] 288-295 (2007)
- 3) J. Zhao, Wei Lin, A. Yamaguchi, J. and J. Sun, *J. Ceram. Soc. Japan*, 115 [10] 654-660 (2007)
- 4) Progress report of FY 2008 MEXT State Subsidy Project, Okayama Ceramics Research Foundation pp. 17-24 (2009.3)
- 5) Akira Yamaguchi, *Taikabutsu*, 35 [7] 365-370 (1983)
- 6) Akira Yamaguchi, *ibid*, 35 [7] 617-622 (1983)
- 7) Yasuhiro Hoshiyama, Akira Yamaguchi and Junji Onmyoji, *ibid*, 61 [10] 548-555 (2009)

Translated from *Taikabutsu* 63 [5] 234-239 (2011)

木質系廃棄物からの炭素の生成と酸化特性

前田朋之, 星山泰宏, 山口明良

一般財団法人岡山セラミックス技術振興財団 〒705-0021 岡山県備前市西片上1406-18

Formation and Oxidation Property of Carbon from Woody Waste

Tomoyuki MAEDA, Yasuhiro HOSHIYAMA and Akira YAMAGUCHI

Okayama Ceramics Research Foundation, 1406-18, Nishikatakami, Bizen-shi, Okayama 705-0021, Japan

キーワード：木材, 炭素, 結晶化, 酸化

1 緒言

日本では、耐火物の主要原料の多くを海外に依存している¹⁾。環境規制の強化、各国における資源確保などの理由から原料を輸入できないあるいは制限される恐れがあり、将来にわたって、安定に確保する必要がある²⁾。

耐火物原料の中でも黒鉛などの炭素は日本での産出はほとんどなく、国外に依存している。他方、岡山県真庭市においてバイオマス利用できる木質系副産物が年間12万t発生しており、うち約8割は木炭、バイオエタノールなどの燃料に利用されているが、残り約2割は利用されないまま廃棄されている。その内訳は木屑や樹皮である。これらを炭化すれば木質系炭素原料として有効利用できる可能性がある。

一般的に木質系から得られる炭素の収率は20%程度といわれている。先述の真庭市の木質系廃棄物約2.4万t/年を炭化すると、単純計算で約5000t/年の炭素が得られることになり、日本全国に拡大して考えれば黒鉛の年間輸入量4.5万tに十分匹敵するだけの量の炭素を得ることも可能と考えられる。

本研究は、耐火物用の炭素原料を国内で調達する方策の一つとして、木質系廃棄物を用いることを試みた。炭素材料の多様な物性はその構造に起因することが言われているため³⁾、ここでは木材由来の炭素の特性を調査し、黒鉛、フェノール樹脂およびピッチから得られた炭素などと比較検討を行った。

2 実験方法

木材試料として杉 (Cedar)、ひのき (Cypress)、広葉樹 (Hardwood) および樹皮 (Bark) を用いた。また、比較材料としてフェノール樹脂、ピッチ (軟化点122℃) も用いた。

杉、ひのき、広葉樹および樹皮を大気中、100℃、3時間で乾燥した。乾燥後の試料を粉碎し、アルゴン雰囲気中で最大1450℃まで加熱して熱重量分析 (TG) を行った。

残炭率は、乾燥後の木材試料を炭素粉末中、800℃、3時間保持の条件で熱処理し、試験前後の重量変化から求めた。フェノール樹脂は、液状のノボラック型に10mass%のヘキサミンを加えたものを大気中、200℃、12時間保持の条件で熱処理して硬化させた後、炭素粉末中で800℃に加熱した。

800℃加熱後の試料をアルゴン雰囲気下で1500および2000℃で熱処理を行った。木材、フェノール樹脂およびピッチからの炭素の結晶性を評価するために、得られた粉末を粉末X線回折法により測定した。グラファイトのピーク強度は、ブロードな回折パターンを差し引いて評価した。

耐酸化性は、TGを用いて、重量減少の開始温度および終了温度の測定から評価された。測定には2000℃で熱処理を行った試料で2 mm程度の大きさのものと、めのう乳鉢により微粉碎したものの2種類の試料について行った。また、比較としてカーボンブラック、鱗状黒鉛、人造黒鉛および土状黒鉛についても測定した。

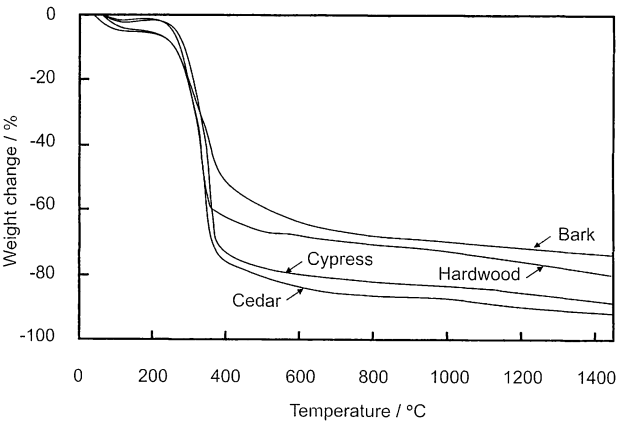


Fig.1 Weight change of wood.

第71回原料専門委員会発表
投稿責任者：前田朋之

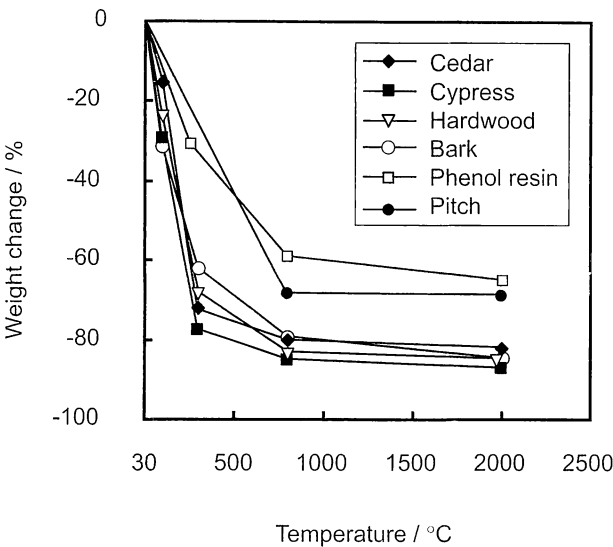


Fig.2 Weight change of wood, pitch and phenol resin.

3 結果および考察

図 1 にアルゴン雰囲気中における木材試料の熱重量変化を示す。約300℃で重量が大きく減少し、その後徐々に減少した。図 2 に各処理温度における積算の重量変化を示す。木材において2000℃加熱での炭素の収率が最も高いのは杉で17.7%，最も低いのはひのきで13.1%であった。また、ピッチは31.2%，フェノール樹脂は35.7%であり、木材の収率はピッチおよびフェノール樹脂と比較して低い結果となった。

図 3 および図 4 に1500℃および2000℃での炭化後の木材のX線回折パターンを示す。熱処理温度1500℃では全ての木材でブロードな回折線が観察され、ほとんど結晶化していないことがわかった。一方、熱処理温度が2000℃では全ての木材でグラファイトのピークが観察された。グラファイトのピーク強度は杉、ひのきおよび広葉樹は同程度であ

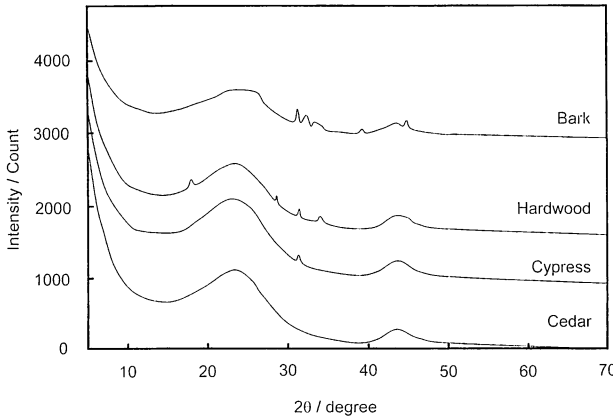


Fig.3 XRD patterns of carbonized wood after heating at 1500℃ .

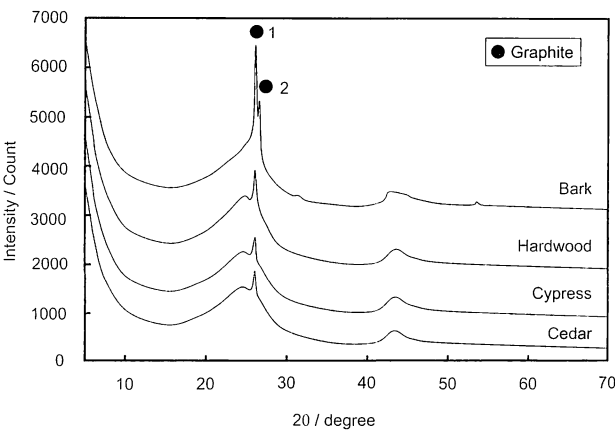


Fig.4 XRD patterns of carbonized wood after heating at 2000℃ .

Table 1 XRD intensity of carbonized wood, phenol resin and pitch

Sample	Peak intensity after heating at 1500°C(2θ=26.5°)			Peak intensity after heating at 2000°C(2θ=26.5°)		
	Total	Broad	Sharp	Total	Broad	Sharp
Cedar	60	60	0	601	301	300
Cypress	84	84	0	618	337	281
Hardwood	99	99	0	839	411	428
Bark	181	181	0	1:1722 2:1006	1:432 2:341	1:1290 2:665
Phenol resin	300	300	0	387	387	0
Pitch	5615	0	5615	10569	0	10569

るのに対し、樹皮は他より高く、結晶化しやすいことがわかった（表 1）。また、樹皮において 2 種類の炭素の回折ピーク（d=0.343nm, d=0.337nm）が確認された。

図 5 および図 6 に炭化後のフェノール樹脂およびピッチのX線回折パターンを示す。フェノール樹脂は熱処理温度に関わらずブロードな回折線、ピッチは1500℃からグラファイトのピークが観察された。一般的にピッチの炭化はメ

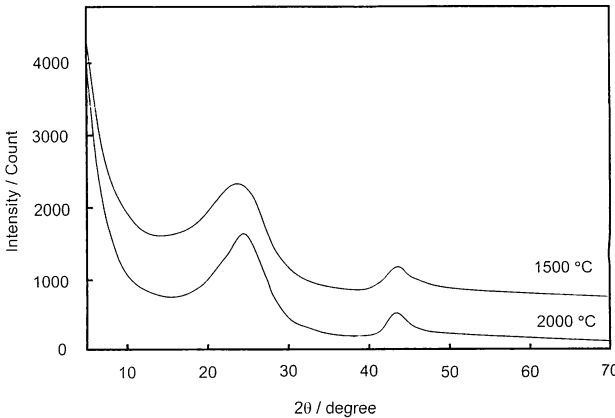


Fig.5 XRD patterns of carbonized phenol resin.

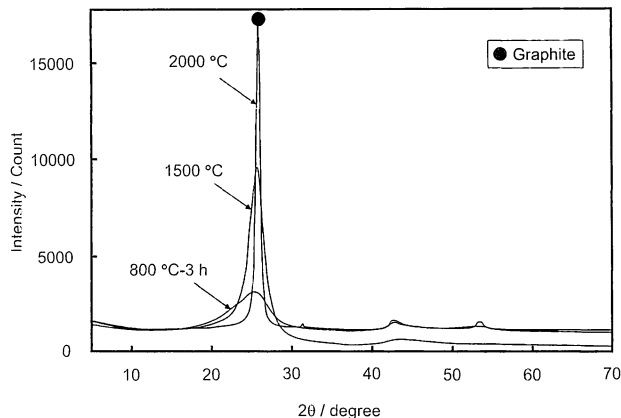


Fig.6 XRD patterns of carbonized pitch.

ソフェーズ相の生成により黒鉛組織が発達しやすい液相炭化（易黒鉛化性炭素）であり、フェノール樹脂の炭化は液相を介さず、黒鉛組織が発達しにくい固相炭化（難黒鉛化性炭素）であると言われている³⁻⁵⁾。杉、ひのきおよび広葉樹の回折線はフェノール樹脂と似て炭素の結晶性が低いことから、大部分が固相炭化によって炭化が進んでいるものと思われる。一方で、樹皮は他の木材と比較して結晶性が高いことから、ピッチのような液相炭化も一部で起こっている可能性が考えられる。

図7に処理前の木材の微構造を示す。杉、ひのきは一方方向に縦長の細胞からなる管状組織（師管あるいは道管）、広葉樹においては部分的に方向が違う管状組織が観察された。また、樹皮は整列していない構造であった。図8に炭化後の微構造を示す。図7と図8を比較すると木材の炭化部は細胞壁であると考えられ、微構造は多孔質であった。杉およびひのきは数μm程度の薄い炭素、広葉樹および樹皮は数10μm程度の緻密な炭素が得られ、ガラス状組織に観察された。

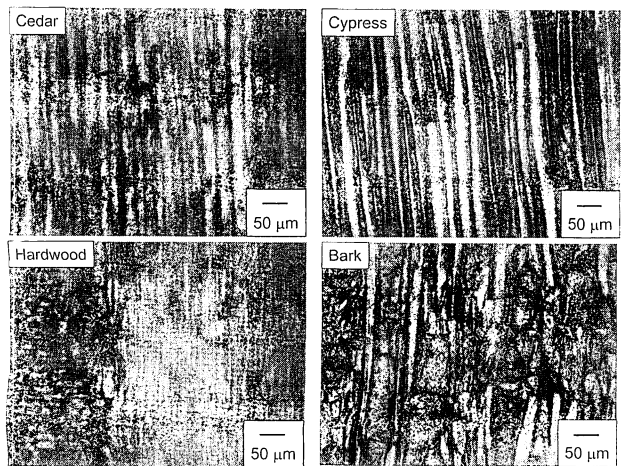


Fig.7 Microphotographs of wood.

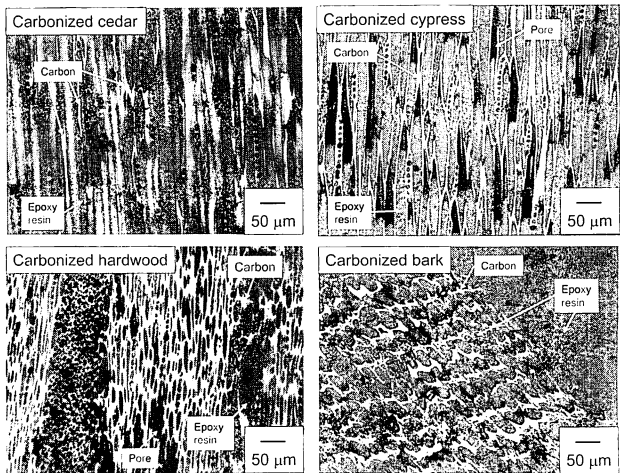


Fig.8 Microphotographs of carbonized wood after heating at 2000°C.

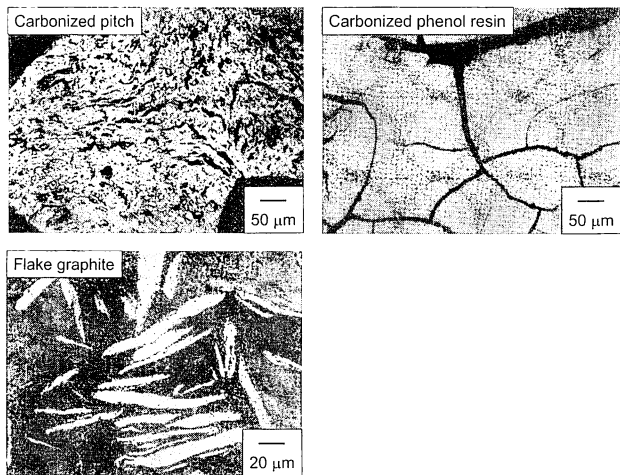


Fig.9 Microphotographs of carbonized pitch, phenol resin, and flake graphite.

図9に炭化後のピッチ、フェノール樹脂および鱗状黒鉛の微構造を示す。炭化後のピッチはメソフェーズ相が生成・合体して炭化が進むことによる流れ組織、フェノール樹脂はガラス状組織、結晶質の鱗状黒鉛では層状構造が発達している様子が観察された。木材由来の炭素の微構造はフェノール樹脂のようなガラス状組織であり、粉末X線回折の結果同様、微構造からもフェノール樹脂と同じ固相炭化により炭化が進んでいると推測される。

図10および図11に種々の炭素の大気中における熱重量変化を示す。図10は2 mm程度の大きさの試料、図11は粉末状の試料の測定結果である。酸化開始および終了温度はTG曲線の接線の交点により算出し、その結果を表2に示す。木材から得られた炭素は約550℃で酸化が始まり、700℃までに全て反応し、木材種における大きな差は見られなかった。また、粉末状と固形状との耐酸化性を比較すると固形状が高温側へシフトしており炭素の耐酸化性には粒径

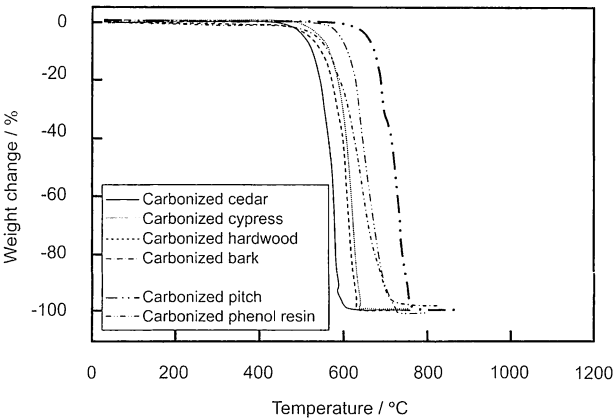


Fig.10 Weight change of various bulk carbon.

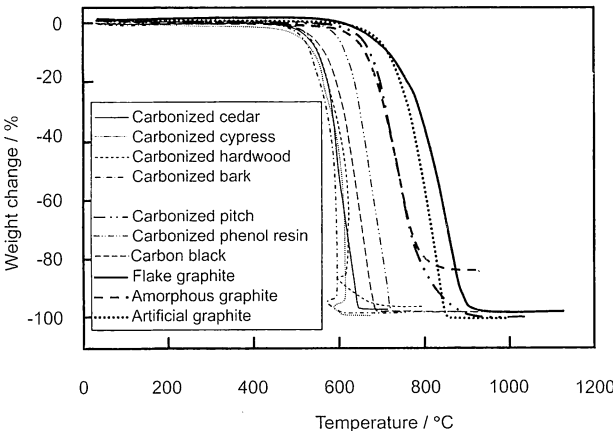


Fig.11 Weight change of various carbon.

Table 2 Oxidation temperature and maxim weight change of various carbons

Sample	Starting temperature of oxidation / °C		End temperature of oxidation/ °C		Weight change / %	
	Powder	Bulk	Powder	Bulk	Powder	Bulk
Cedar	560	534	643	589	-97.8	-98.8
Cypress	538	583	606	641	-99.5	-99.2
Hardwood	548	566	682	630	-96.7	-99.3
Bark	536	572	599	706	-98.4	-97.8
Pitch	672	677	761	761	-100	-98.9
Phenol resin	616	617	729	729	-98.1	-100
Carbon black	581		681		-98.0	
Flake graphite	745		894		-98.1	
Amorphous graphite	671		784		-84.3	
Artificial graphite	732		843		-100	

が影響を与えることがわかった。なお、木材のTG曲線において酸化終了付近の温度でノイズが見られた。これは酸化時に発生する熱量が他の炭素よりも大きく測定温度に影響を与えたためである。

結晶性の高い炭素（ピッチから得られた炭素、鱗状黒鉛、人造黒鉛および土状黒鉛）と結晶性の低い炭素（フェノール樹脂から得られた炭素およびカーボンブラック）との酸化開始・終了温度を比較すると、結晶性が高い炭素は高温側であり、耐酸化性と結晶性には関係があることが推察できる。また、結晶性の低い炭素（図中の細線）の中でも木材由来の炭素の酸化開始・終了温度は低温側であり、木炭の耐酸化性は低いといえる。なお、木材由来の炭素における重量減少率は約100%であることから灰分が少ない高純度の炭素が得られると考えられる。

4 まとめ

杉、ひのき、広葉樹および樹皮を用いて、木材から得られる炭素の特性を調査した結果、次の知見を得た。

- (1) 木材はアルゴン雰囲気中において約300℃で重量が大きく減少し、その後徐々に減少する。
- (2) 木材からの炭素の収率はピッチおよびフェノールと比較して低い。
- (3) 2000℃で熱処理した杉、ひのきおよび広葉樹のグラフアイトのピーク強度は同程度であるのに対し、樹皮は他より高く、結晶化しやすい。
- (4) 木材から得られた炭素の微構造は多孔質であり、杉およびひのきは数μm程度の薄い炭素、広葉樹および樹皮は数10μm程度の緻密な炭素が得られ、ガラス状組織に観察された。

- (5) アルゴン雰囲気中、2000℃の熱処理を行った木材は約550℃で酸化が始まり、700℃までに全て反応した。他の炭素材料の酸化挙動と比較すると低温から酸化が始まり、酸化終了温度も低いことから耐酸化性は低いと言える。

文献

- 1) 高橋忠明：耐火物, 57 [4] 169-178 (2005).
- 2) 桑野清吾：耐火物, 57 [4] 184-190 (2005).
- 3) 持田 勲, 光来要三：九州大学機能物質化学研究所報告, 4 [2] 81-88 (1990).
- 4) 船引恭平, 中村昌之, 釣谷雅明：耐火物, 33 [2] 64-80 (1981).
- 5) 岡本寛己, 藤井謙治, 池田文恵：耐火物57 [5] 252-261 (2005).

CaO-Cr₂O₃-Al₂O₃系組成物における6価クロム化合物の生成とその抑制

前田朋之, 山口明良, 星山泰宏, 水原詞治*, 占部武生*

一般財団法人岡山セラミックス技術振興財団 〒705-0021 岡山県備前市西片上1406-18

Precipitation and Inhibition of Cr⁶⁺ Compound in the CaO-Cr₂O₃-Al₂O₃ System

Tomoyuki MAEDA, Akira YAMAGUCHI, Yasuhiro HOSHIYAMA, Shinji MIZUHARA*, Takeo URABE*

Okayama Ceramics Research Foundation, 1406-18, Nishikatakami, Bizen, Okayama 705-0021

Abstract : The formation of toxic Cr⁶⁺ compounds from chrome compounds are promoted in an oxidation atmosphere below 1273K under the existence in alkaline and/or CaO component, and further even in the case of elevate temperature under the coexistence with Al₂O₃. In this paper, the precipitation and inhibition of Cr⁶⁺ compound were studied in the CaO-Cr₂O₃-Al₂O₃ system. The mass ratio of CaO/Cr₂O₃/Al₂O₃ components and CaO/Cr₂O₃/Al₂O₃/Additive components were adjusted to 1/3/0 - 1/3/3 and 1/3/1/1, respectively. V₂O₅, SiO₂, Ca(PO₃)₂, SnO₂ and ZrO₂ were selected as additives. Ca₄Al₆Cr⁽⁶⁺⁾O₁₆ identified in all the CaO-Cr₂O₃-Al₂O₃ system at 1723K. On the other hand, the precipitation of Cr⁶⁺ compounds were inhibited by addition of V₂O₅, SiO₂, Ca(PO₃)₂ and SnO₂.

Key words : Ca₄Al₆CrO₁₆, CaCrO₄, Hexavalent chromium compounds, inhibition, chrome refractory

要 旨 : クロム化合物はアルカリやCaOが存在すると1273K以下の酸化雰囲気中において有害なCr⁶⁺化合物を生成する。更にAl₂O₃が添加されると高温領域においてもCr⁶⁺化合物が生成する。ここでは、CaO-Cr₂O₃-Al₂O₃系組成物における6価クロム化合物の生成とその抑制について研究した。CaO : Cr₂O₃ : Al₂O₃系組成物およびCaO : Cr₂O₃ : Al₂O₃ : 添加剤系組成物の重量比は1 : 3 : 0 - 1 : 3 : 3および1 : 3 : 1 : 1に調整した。添加剤にはV₂O₅, SiO₂, Ca(PO₃)₂, SnO₂およびZrO₂を用いた。全てのCaO-Cr₂O₃-Al₂O₃系組成物でCa₄Al₆CrO₁₆が同定された。また、V₂O₅, SiO₂, Ca(PO₃)₂およびSnO₂の添加は6価クロム化合物の生成を抑制した。

キーワード : Ca₄Al₆CrO₁₆, CaCrO₄, 6価クロム化合物, 抑制, クロム含有耐火物

1 緒言

廃棄物溶融炉で発生するスラグは、CaO/SiO₂比が0.5-1.0と低く、アルカリを多く含む¹⁾。そのため、溶融炉用耐火物には優れた耐スラグ性が要求され、酸化雰囲気の中ではCr₂O₃-Al₂O₃系などのクロム含有耐火物が使用される場合がある^{2,3)}。耐火物中のCr₂O₃は、①炉内が酸化雰囲気、②アルカリが共存、③温度が1473K以下、という条件が重なる場合に人体に有害な6価クロム化合物を生成し易い⁴⁻⁷⁾。この問題を解決するためにクロムフリー耐火物の適応研究がおこなわれているが、クロム含有耐火物と同等な耐食性のあるクロムフリー耐火物は開発されておらず、現在では低クロム含有耐火物の適用や酸化物添加などによる6価クロム化合物の生成抑制がなされている⁸⁻¹²⁾。

CaO-Cr₂O₃系組成物中に生成する6価クロム化合物は、Cr₂O₃含有量が50mol%以上では1346K以下、50mol%以下では1049K以下でCaCr⁽⁶⁺⁾O₄として生成することが知られており、その生成は、CaOとCr₂O₃との結合を防止するSiO₂やTiO₂等の酸化物添加や、還元雰囲気中での熱処理などにより、抑制可能であることが報告されている¹³⁻¹⁵⁾。

実際に使用されている耐火物組成を考慮すると、CaO-Cr₂O₃-Al₂O₃の3成分系で議論されるべきであると思われる。しかし、現在報告されている3成分系での6価クロム化合物は、①1473-1673KにおいてCa₄Al₆Cr⁽⁶⁺⁾O₁₆が生成する、②Ca₄Al₆Cr⁽⁶⁺⁾O₁₆を中心とした簡易なCaO-CaCrO₄-Al₂O₃系相平衡状態図が図示されている程度であり、詳細な報告は少ない¹⁶⁾。

これまで著者は、CaO-Cr₂O₃-Al₂O₃系において大気中での6価クロム化合物の生成について研究を行い、①1373K以下でCaCr⁽⁶⁺⁾O₄が生成すること、②1373K以上でCa₄Al₆Cr⁽⁶⁺⁾O₁₆が生成すること、③Ca₄Al₆CrO₁₆が使用後耐火物中にも存在していることを明らかにした^{17,18)}。また、Ca₄Al₆Cr⁽⁶⁺⁾O₁₆の性質として、水への溶出速度がCaCr⁽⁶⁺⁾O₄と比較して遅いことや、熱的に安定な化合物であり、温度

平成25年9月4日受付、平成25年12月10日受理
投稿責任者：前田朋之

* 龍谷大学理工学部環境ソリューション学科
〒520-2194 滋賀県大津市瀬田大江町横谷1-5

前田朋之他 CaO-Cr₂O₃-Al₂O₃系組成物における6価クロム化合物の生成とその抑制

変化によってCr⁶⁺→Cr³⁺の価数変化が起こらないことも明らかにした¹⁹⁾。

現在のクロム含有耐火物では環境負荷低減のため低クロム-アルミナ質耐火物が使用されていることや、使用後耐火物中にもCa₄Al₆Cr⁽⁶⁺⁾O₁₆が確認されたことを考慮すると、Al₂O₃含有量とCa₄Al₆Cr⁽⁶⁺⁾O₁₆生成量との関係、およびCa₄Al₆Cr⁽⁶⁺⁾O₁₆の生成抑制方法を検討することは重要であると考えられる。そこで本研究では、CaO-Cr₂O₃-Al₂O₃系組成物において、Al₂O₃量の変化に伴うCa₄Al₆Cr⁽⁶⁺⁾O₁₆生成への影響、および他成分添加による6価クロム化合物の生成抑制効果について検討を行った。

2 実験方法

CaCr⁽³⁺⁾₂O₄の理論組成 (CaO : Cr₂O₃ = 56 : 152/重量比) 付近である重量比CaO : Cr₂O₃ = 1 : 3を基準にして、CaO : Cr₂O₃ : Al₂O₃ = 1 : 3 : 0.1 : 3 : 3の混合粉末、およびCaO : Cr₂O₃ : Al₂O₃ : 添加剤 = 1 : 3 : 1 : 1の混合粉末を作製した。添加剤には、SiO₂, ZrO₂, V₂O₃, SnO₂, Ca(PO₃)₂を用いた。

配合した粉末はエタノールを用いて10vol%サスペンションにし、マグネティックスターラーにより24時間攪拌した。その後、473Kで攪拌しながらエタノールを蒸発させた。攪拌混合した粉末を20MPaで成形し、1723K、15分間、大気中で熱処理した。冷却は液体窒素中へ投入する急冷を行った。熱処理後の各試料における生成鉱物相は粉末X線回折法により同定し、6価クロム化合物生成の有無を確認した。また、Cr₂O₃へのAl₂O₃の固溶量は、Cr₂O₃とAl₂O₃とが全率固溶することから、(1)式を用いて算出した。

$d_{ss} = d_{Cr} \cdot [Cr_2O_3] + d_{Al} \cdot [Al_2O_3]$ (1)
ここで、d_{ss}はCr₂O₃-Al₂O₃固溶体の(300)面間距離、d_{Cr}はCr₂O₃の(300)面間距離、d_{Al}はα-Al₂O₃の(300)面間距離、[Cr₂O₃] および [Al₂O₃] は固溶体中における各成分のmol分率を示す。

3 結果

表1に混合割合と1723K熱処理後の鉱物相、図1に熱処理後の回折パターンを示す。CaO-Cr₂O₃系ではCaCr⁽³⁺⁾₂O₄が、CaO-Cr₂O₃-Al₂O₃系ではCa₄Al₆Cr⁽⁶⁺⁾O₁₆が主鉱物相として同定された。その他の鉱物相として、Al₂O₃-Cr₂O₃固溶体や、冷却過程で6価クロム化合物へと変化するCaCr⁽³⁺⁾₂O₄が生成していた。また、Cr₂O₃の回折線はAl₂O₃含有量の増加につれて高角度側にシフトしており、(1)式より概算するとCr₂O₃に対するAl₂O₃の固溶量が増加することがわかった。

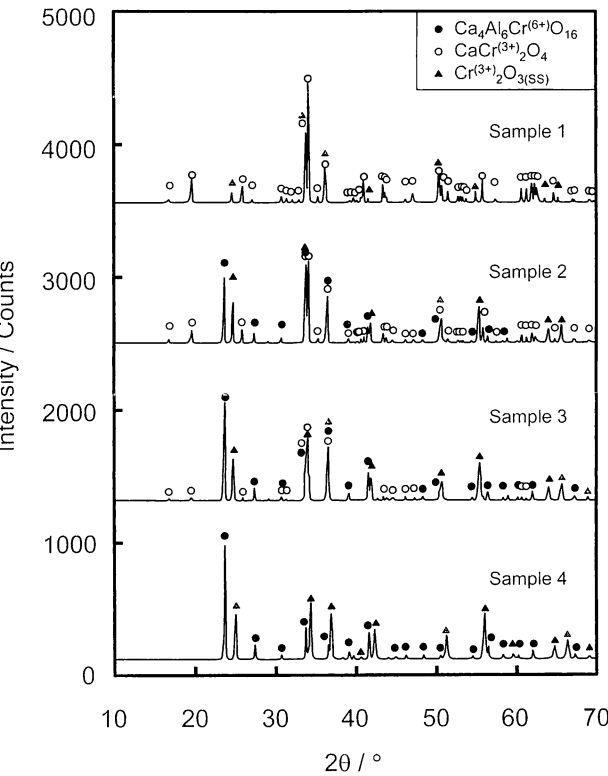


Fig. 1 XRD patterns of the CaO-Cr₂O₃-Al₂O₃ system after heating at 1723K for 15 min in air.

Table 1 Composition of samples and mineral phases after heating at 1723K for 15 min in air

Sample No.	Composition of starting mixture (mass ratio)			Mineral phase
	CaO	Cr ₂ O ₃	Al ₂ O ₃	
1	1	3	0	CaCr ⁽³⁺⁾ ₂ O ₄ , Cr ⁽³⁺⁾ ₂ O ₃
2	1	3	1	Ca ₄ Al ₆ Cr ⁽⁶⁺⁾ O ₁₆ , CaCr ⁽³⁺⁾ ₂ O ₄ , Cr ⁽³⁺⁾ ₂ O ₃
3	1	3	2	Ca ₄ Al ₆ Cr ⁽⁶⁺⁾ O ₁₆ , CaCr ⁽³⁺⁾ ₂ O ₄ , (Al _{0.25} Cr ⁽³⁺⁾ _{0.75}) ₂ O ₃
4	1	3	3	Ca ₄ Al ₆ Cr ⁽⁶⁺⁾ O ₁₆ , (Al _{0.57} Cr ⁽³⁺⁾ _{0.43}) ₂ O ₃

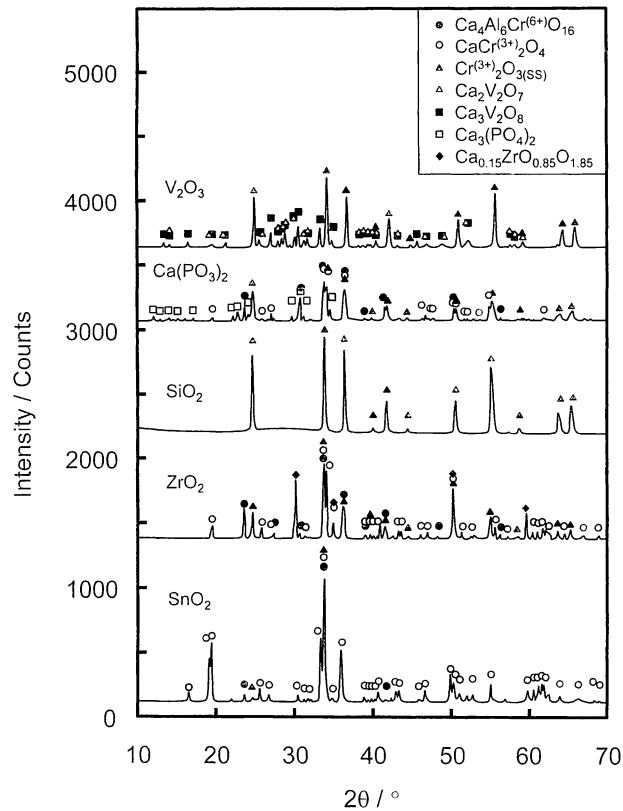


Fig. 2 XRD patterns of the CaO-Cr₂O₃-Al₂O₃-additive system after heating at 1723K for 15 min in air.

図2および表2に、CaO-Cr₂O₃-Al₂O₃-添加剤系の1723K、15分大気圧加熱後の回折パターンおよび鉱物相を示す。また、図3にCaO-Cr₂O₃-Al₂O₃-SiO₂系の熱処理後の回折パターンを拡大して示す。V₂O₅およびSiO₂の添加では、Ca₄Al₆Cr⁽⁶⁺⁾O₁₆が全く生成しておらず、6価クロム化合物の生成抑制効果が非常に高いことが明らかとなった。SiO₂添加では2θ = 30°付近にブロードな回折線が観察され、非晶質相が形成されていることが確認された(図3)。Ca(PO₃)₂添加ではCr₂O₃およびCa₄Al₆Cr⁽⁶⁺⁾O₁₆が、SnO₂添加ではCr₂O₃、CaCr⁽³⁺⁾₂O₄およびCa₄Al₆Cr⁽⁶⁺⁾O₁₆が生成し

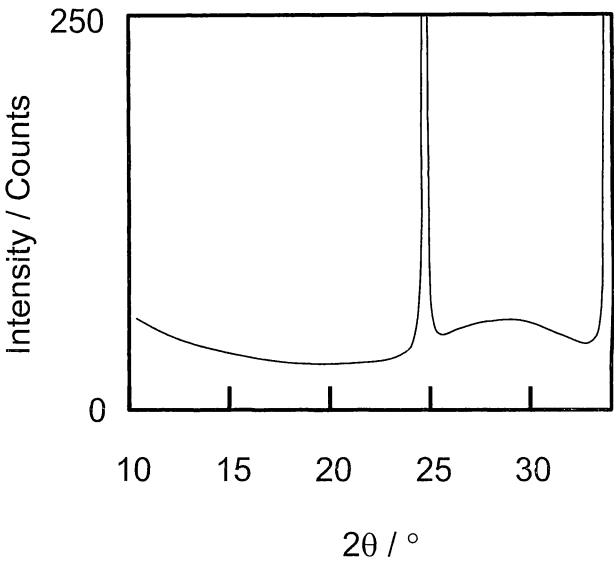


Fig. 3 XRD pattern of the CaO-Cr₂O₃-Al₂O₃-SiO₂ system after heating at 1723K for 15 min in air.

ていたが、両試料におけるCa₄Al₆Cr⁽⁶⁺⁾O₁₆の生成量は少なく、6価クロム化合物の生成抑制効果が高いことがわかった。一方、ZrO₂添加では、CaOとの化合物が同定されたものの、Ca₄Al₆Cr⁽⁶⁺⁾O₁₆が比較的大きなピークで認められ、他の添加剤と比較して6価クロム化合物の生成抑制効果が低いことがわかった。

4 考察

図1より、CaO-Cr₂O₃系にAl₂O₃が共存するといずれのAl₂O₃含有量でも熱処理時間は15分と短時間であるにもかかわらずCa₄Al₆Cr⁽⁶⁺⁾O₁₆が同定され、Ca₄Al₆Cr⁽⁶⁺⁾O₁₆は生成しやすい鉱物相であると言える。また既報において、CaO-Cr₂O₃-Al₂O₃系で、773-1373Kの温度域でCaCr⁽⁶⁺⁾O₄が生成し、1373K以上ではCa₄Al₆Cr⁽⁶⁺⁾O₁₆が生成すること、および生成したCa₄Al₆Cr⁽⁶⁺⁾O₁₆は熱変動により価数変化しない6価クロム化合物であることが明らかにされている^{17,18)}。これらのことから、CaO-Cr₂O₃-Al₂O₃系組成物は773K以上

Table 2 Mineral phases of the CaO-Cr₂O₃-Al₂O₃-additive system after heating at 1723K for 15 min in air

Additive	Mineral phase
V ₂ O ₅	(Al _{0.35} ,Cr ⁽³⁺⁾ _{0.65}) ₂ O ₃ , Ca ₂ V ₂ O ₇ , Ca ₃ V ₂ O ₈
Ca(PO ₃) ₂	Ca ₄ Al ₆ Cr ⁽⁶⁺⁾ O ₁₆ , CaCr ⁽³⁺⁾ ₂ O ₄ , (Al _{0.19} ,Cr ⁽³⁺⁾ _{0.71}) ₂ O ₃ , Ca ₃ (PO ₄) ₂
SiO ₂	(Al _{0.14} ,Cr ⁽³⁺⁾ _{0.86}) ₂ O ₃ , Amorphous
ZrO ₂	Ca ₄ Al ₆ Cr ⁽⁶⁺⁾ O ₁₆ , CaCr ⁽³⁺⁾ ₂ O ₄ , (Al _{0.12} ,Cr ⁽³⁺⁾ _{0.88}) ₂ O ₃ , Ca _{0.15} Zr _{0.85} O _{1.85}
SnO ₂	Ca ₄ Al ₆ Cr ⁽⁶⁺⁾ O ₁₆ , CaCr ⁽³⁺⁾ ₂ O ₄ , (Al _{0.10} ,Cr ⁽³⁺⁾ _{0.90}) ₂ O ₃

前田朋之他 CaO-Cr₂O₃-Al₂O₃系組成物における 6 価クロム化合物の生成とその抑制

で加熱すると幅広い組成領域且つ、広範囲の温度域で 6 価クロム化合物が生成すると言える。

一方、Ca₄Al₆Cr⁽⁶⁺⁾O₁₆以外の 6 価クロム化合物は同定されなかったが、CaCr⁽³⁺⁾₂O₄が同定された組成がある。CaCr⁽³⁺⁾₂O₄は1373K以上の高温域では 3 価クロム化合物であるが、773-1373Kに長時間さらされるとCaCr⁽⁶⁺⁾O₄へ相変化するため、注意すべきクロム化合物である。図4に Al₂O₃含有量に対するCaCr⁽³⁺⁾₂O₄およびCa₄Al₆Cr⁽⁶⁺⁾O₁₆の回折強度の変化を示す。Al₂O₃含有量の増加に併ってCaCr⁽³⁺⁾₂O₄は減少し、逆にCa₄Al₆Cr⁽⁶⁺⁾O₁₆は増加しており、相関性が認められる。この相関性と、CaO-Cr₂O₃-Al₂O₃系組成物中では1373K以下でCaCr⁽⁶⁺⁾O₄が生成し、1373K以

上ではCa₄Al₆Cr⁽⁶⁺⁾O₁₆（理論組成比 = CaO : Cr₂O₃ : Al₂O₃ ≒ 1 : 0.3 : 1.4/重量比）が生成するという既報^{17,18)}より、CaO-Cr₂O₃-Al₂O₃系では図5に示す反応が起こっていると考えられる。まず、773-1373Kに加熱されるとCaOとCr₂O₃との反応でCaCr⁽⁶⁺⁾O₄が生成し、1373K以上になるとCaCr⁽⁶⁺⁾O₄とAl₂O₃との反応でCa₄Al₆Cr⁽⁶⁺⁾O₁₆が生成する。その他の鉱物相はAl₂O₃量/CaO量 = 1.4を境に異なっており、1.4以下の場合、CaOとCr₂O₃との反応によるCaO-Cr₂O₃系化合物が、1.4以上ではAl₂O₃とCr₂O₃との反応によるCr₂O₃(ss)が生成する。

次に、CaO-Cr₂O₃-Al₂O₃系における 6 価クロム化合物の生成抑制について考察する。CaO-Cr₂O₃系組成物における 6 価クロム化合物の生成抑制には、CaOと優先的に反応するSiO₂を添加し、CaCr⁽³⁺⁾₂O₄ + SiO₂ = Ca₂SiO₄ + Cr₂O₃の反応を起こすことにより、CaCr⁽³⁺⁾₂O₄量を減少させ、その結果としてCaCr⁽⁶⁺⁾O₄の生成を抑制させる方法がある¹³⁾。前述のように、CaO-Cr₂O₃-Al₂O₃系で生成する 6 価クロム化合物はCa₄Al₆Cr⁽⁶⁺⁾O₁₆とCaCr⁽⁶⁺⁾O₄であり、いずれもCaOの化合物であることから、優先的にCaOと化合物を形成する酸化物を添加することは有効であると推測される。

図2より、抑制効果が高かった添加剤はSiO₂、V₂O₃、Ca(PO₃)₂、SnO₂であり、その中でCaOと反応物を形成しているのはSiO₂、V₂O₃、Ca(PO₃)₂であった。これら3種の添加において、CaOが添加剤と反応することにより 6 価クロム化合物の生成を抑制したことをより詳細に確認するために、973K、1373Kでの鉱物相の変化も検討した。

図6-8に、各添加剤における973Kおよび1373Kでの熱処理後の回折パターンを示す。まずV₂O₃添加では、図6の結果より973K、1373Kにおいても 6 価クロム化合物は同定されなかった。バナジウムの化合物としては、CaV₂O₆、Ca₂V₂O₇およびCa₃V₂O₈が同定され、低温からCaOと化合

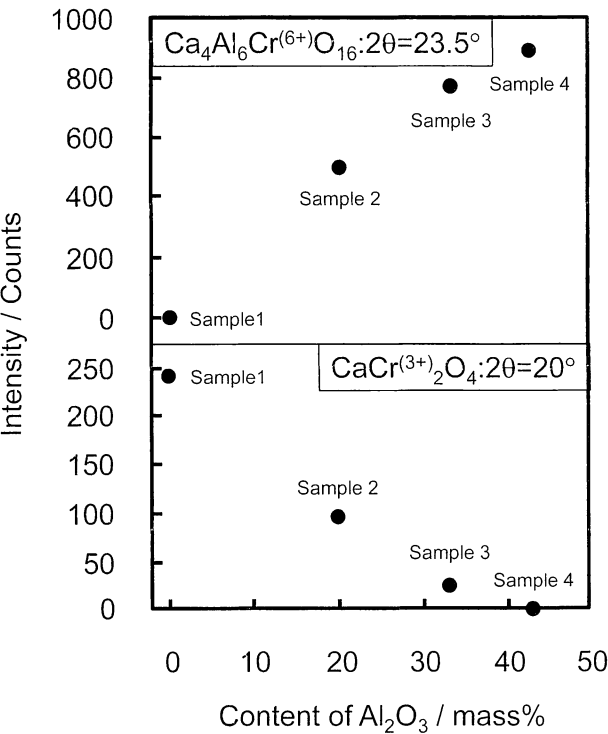


Fig. 4 Relationship between content of Al₂O₃ and XRD intensity of chromium compounds.

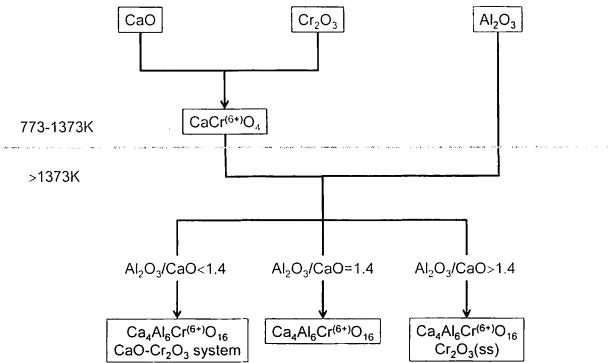


Fig. 5 Reaction of chromium compound in the CaO-Cr₂O₃-Al₂O₃ system.

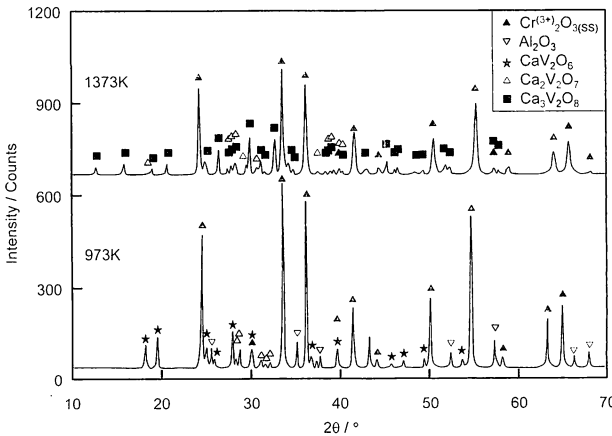


Fig. 6 XRD patterns of the CaO-Cr₂O₃-Al₂O₃-V₂O₃ system after heating at 973-1373K for 15 min in air.

物を形成しており、広い温度域で優れた6価クロム化合物の生成抑制剤になると言える。次にCa(PO₃)₂添加に関して、図7より973KでCaCr⁽⁶⁺⁾O₄が、1373KではわずかにCa₄Al₆Cr⁽⁶⁺⁾O₁₆が同定された。添加したCa(PO₃)₂は、973Kでは変化せずCa(PO₃)₂として、1373KではCa₃(PO₄)₂として同定された。これより、Ca(PO₃)₂は1373K以上でCaOと優先的に反応し、6価クロム化合物の生成抑制剤となっていることが言える。

SiO₂添加に関して、図8より添加したSiO₂は973K、1373KではCaOと反応しておらず、6価クロム化合物も検出された。これより、SiO₂添加により6価クロム化合物の生成抑制を行うには1723K程度の熱処理が必要であると考えられる。また、図3より1723Kでは非晶質相が確認されていることから、SiO₂添加による6価クロム化合物の生成抑制は、SiO₂とCaOとの反応の結果によるものであると考

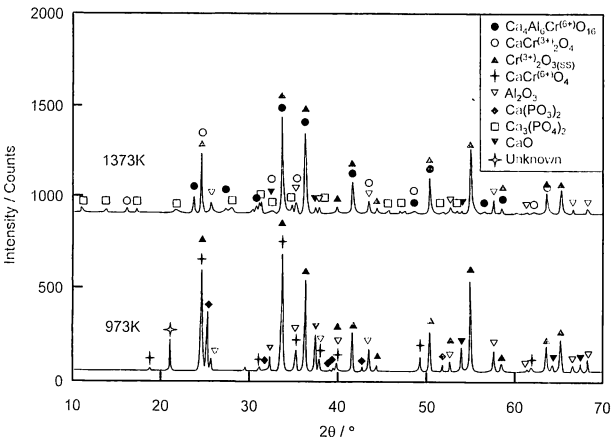


Fig. 7 XRD patterns of the CaO-Cr₂O₃-Al₂O₃-Ca(PO₃)₂ system after heating at 973-1373K for 15 min in air.

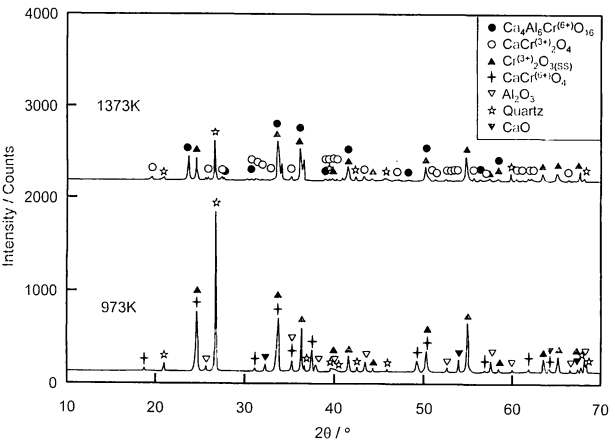


Fig. 8 XRD patterns of the CaO-Cr₂O₃-Al₂O₃-SiO₂ system after heating at 973-1373K for 15 min in air.

えられる。坂井らも実炉スラグにおいて、1673K以上の熱処理を行うと6価クロムは溶出しなことを報告しており¹⁴⁾、SiO₂を用いる場合には、高温熱処理を行って、SiO₂とCaOとの反応を促進する必要があると考えられる。このように、各添加剤で6価クロム化合物に対する生成抑制効果が見られる温度範囲は異なっているが、CaOと優先的に反応させることでCaO-Cr₂O₃-Al₂O₃系組成物中の6価クロム化合物の生成抑制は可能であると言える。

ZrO₂添加においては、図2に示すようにCaOとZrO₂との化合物であるCa_{0.15}Zr_{0.85}O_{1.85}が生成する一方で、6価クロム化合物も生成していた。添加したZrO₂がCaOと化合物を形成しているにも関わらず6価クロム化合物の生成抑制効果が低い理由として、反応したCaO量が少なかったことが考えられる。確認のために、V₂O₃からCa₃V₂O₈、Ca(PO₃)₂からCa₃(PO₄)₂、ZrO₂からCa_{0.15}Zr_{0.85}O_{1.85}が生成する場合の、添加剤1gと反応するCaO量を算出した結果、V₂O₃は1.12g、Ca(PO₃)₂は0.57g、ZrO₂は0.08gとなり、計算上からもZrO₂は6価クロム化合物の生成抑制剤として効果が低いことがわかる。

一方、SnO₂添加では、以下のように他の添加剤とは異なった現象が見られた。SnO₂添加では、CaCr⁽³⁺⁾₂O₄および低い回折強度のCa₄Al₆Cr⁽⁶⁺⁾O₁₆が同定された(図2)。CaCr⁽³⁺⁾₂O₄はAl₂O₃含有量が少ない場合に生成しやすいことから(図4)、添加したSnO₂はCaOではなくAl₂O₃と反応したことが推測される。しかし、図2ではSnO₂-Al₂O₃系化合物は同定されておらず、図9のAl₂O₃-SnO₂系相平衡状態²⁰⁾からもSnO₂とAl₂O₃は化合物を形成しないことが示されている。SnO₂およびAl₂O₃が同定されない理由として、SiO₂添加時と同様でSnO₂およびAl₂O₃を含む多元系のガラ

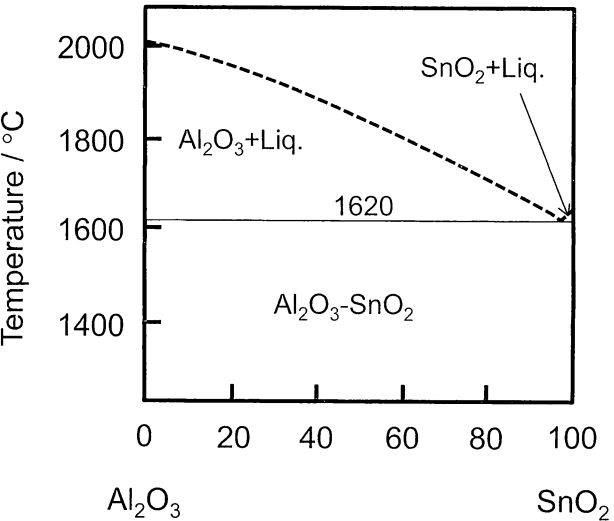


Fig. 9 The phase equilibrium diagram of the Al₂O₃-SnO₂ system²⁰⁾.

前田朋之他 CaO-Cr₂O₃-Al₂O₃系組成物における6価クロム化合物の生成とその抑制

ス相を形成していることも可能性の一つとして考えられる。そこで、SnO₂添加の効果をより明確にするために、徐冷を行い、結晶化を試みた。図10に徐冷後の回折パターンおよび、図11にSnO₂添加時および試料1で生成したCaCr⁽³⁺⁾₂O₄の回折ピークを拡大して示す。図10より、徐冷を行っても多元系化合物は同定されなかった。このことから、1723Kではガラス相は形成していないと推測される。その他にも、徐冷を行ってもCaCr⁽³⁺⁾₂O₄からCaCr⁽⁶⁺⁾₂O₄への相変化も認められないことから、SnO₂は6価クロム化合物の生成抑制効果が高いと言える。また図11より、SnO₂添加時で同定されたCaCr⁽³⁺⁾₂O₄の回折ピークが試料1で同定されたCaCr⁽³⁺⁾₂O₄の回折ピークと比較して低角度側へシフトしている。CaCr⁽³⁺⁾₂O₄の回折ピークのシフトはSnO₂添加時のみで観察されており、SnO₂がCaCr⁽³⁺⁾₂O₄へ固溶した可能性が高いと推測される。これより、SnO₂添加で6価クロム化合物の生成抑制効果が高かった理由と

して、固溶によりCaCr⁽³⁺⁾₂O₄の格子間距離を変化させることで、CaCr₂O₄への相変化を抑制したことが考えられる。一方、Al₂O₃については、本研究で明らかにすることができなかったが、Cr₂O₃とAl₂O₃は固溶体を容易に形成することから、Al₂O₃もCaCr⁽³⁺⁾₂O₄へ固溶している可能性があると思われる。

以上より、CaO-Cr₂O₃-Al₂O₃系組成物における6価クロム化合物の生成は、CaOと優先的に反応する酸化物を添加することで抑制可能である。その他にも、固溶により格子間距離を変化させることでも抑制が可能であると考えられる。

5 まとめ

CaO-Cr₂O₃-Al₂O₃系組成物中のAl₂O₃含有量の変化に伴うCa₄Al₆Cr⁽⁶⁺⁾O₁₆生成の有無、および他成分添加による6価クロム化合物の生成抑制について検討を行った結果、次の知見を得た。

- (1) Al₂O₃が共存すると量比によらずCa₄Al₆Cr⁽⁶⁺⁾O₁₆が生成し、Al₂O₃含有量が多いほどその生成量が增大する。Al₂O₃量が少ない場合は、CaCr⁽³⁺⁾₂O₄の生成量が多くなる。
- (2) Ca₄Al₆Cr⁽⁶⁺⁾O₁₆に伴って生成する副鉱物相は、Al₂O₃/CaO比が1.4以下の場合にはCaCr⁽³⁺⁾₂O₄が生成し、1.4以上の場合にはCr₂O₃-Al₂O₃固溶体が生成する。
- (3) V₂O₅、Ca(PO₃)₂およびSiO₂を添加すると、CaOと優先的に反応して6価クロム化合物の生成を抑制した。
- (4) SnO₂添加では、CaCr⁽³⁺⁾₂O₄へ固溶することで、Ca₄Al₆Cr⁽⁶⁺⁾O₁₆やCaCr⁽⁶⁺⁾₂O₄への相変化を抑制するとみられる。

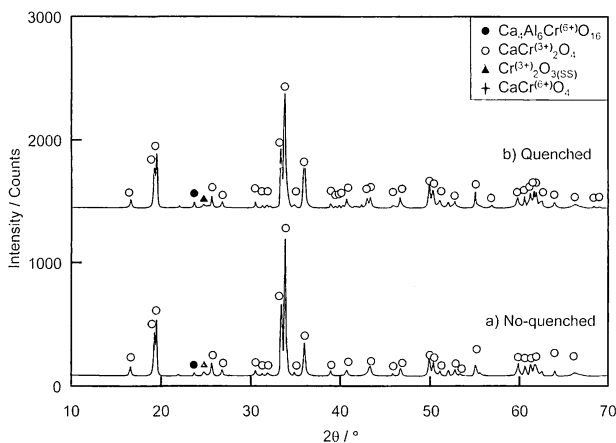


Fig. 10 XRD patterns of the CaO-Cr₂O₃-Al₂O₃-SnO₂ system after heating at 1723K for 15 min in air; (a) no quenched, and (b) quenched by liquid nitrogen.

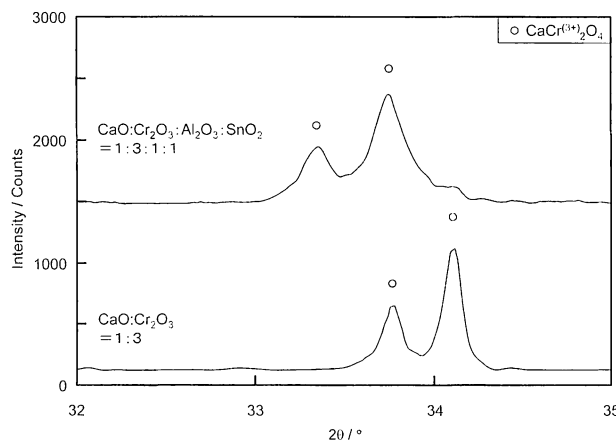


Fig. 11 The low angle shift of XRD pattern of CaCr₂O₄.

文献

- 1) 津田秀行, 北沢 浩, 鈴木 孝: 耐火物, 60 [5] 231-237 (2008).
- 2) 占部武生: 廃棄物学会誌, 18 [5] 292-303 (2007).
- 3) 大河 誠, 蘇 芳充, 梶田吉晴, 太田滋俊: 耐火物, 51 [5] 297-302 (1999).
- 4) 岡本公男: 耐火物, 55 [4] 168-173 (2003).
- 5) 山口明良: 廃棄物学会誌, 13 [1] 47-53 (2002).
- 6) 山口明良: 耐火物, 57 [6] 316-320 (2005).
- 7) 水原詞治, 占部武生: 耐火物, 61 [8] 385-392 (2009).
- 8) 茂田純一, 田中邦彦, 北村伸一: 耐火物, 59 [3] 117 (2007).
- 9) 津田秀行, 北沢 浩, 末川幸弘, 村上海一: 耐火物, 59 [4] 181-187 (2007).
- 10) 尾花豊康, 土成昭弘: 耐火物, 58 [8] 423-428 (2006).
- 11) 原口純一, Zhe Wang, 林 幹基, 有吉騎三郎: 耐火物,

55 [4] 174-182 (2003).

12) 中野裕貴枝, 尾関文仁, 土屋芳樹, 水野好明, 小塚永生: 耐火物, 55 [11] 514-523 (2003).

13) 山口明良: クロム系材料－現状と今後－, 岡山セラミックス技術振興財団 (2005) pp.139-144.

14) 坂井義広, 矢部幸彦, 高橋正光, 飯塚 淳, 柴田悦朗, 中村 崇: Journal of MMIJ, vol.127 714-718 (2011).

15) J. P. R. DreVillers, J. Mathias and A. Muan : Trans.-Inst.Min.Metall., Sect.C, 96, C55-C62 (1987).

16) D. Peters and F. A. Hummel : Cem. Concr. Res., 9 [2] 259-268 (1979).

17) 水原詞治, 占部武生, 山口明良, 前田朋之: 廃棄物資源循環学会誌論文誌, 21 [5] 170-177 (2010).

18) 水原詞治, 占部武生, 山口明良, 前田朋之: 廃棄物資源循環学会誌論文誌, 23 [2] 77-84 (2012).

19) 水原詞治, 占部武生, 山口明良, 前田朋之: 耐火物, 65 [5] 199-204 (2013).

20) V. J. Barczak and R. H. Insley : J. Am. Ceram. Soc., 45 [3] 144 (1962).

各種炭素源をもちいたAl-Zr-C系化合物の合成とその酸化挙動

西川智洋, 前田朋之, 星山泰宏, 高長茂幸

一般財団法人 岡山セラミックス技術振興財団 〒705-0021 岡山県備前市西片上1406-18

Synthesis of Al-Zr-C System Compounds by Using Several Kinds of Carbon Sources and Oxidation Behavior of their Compounds

Tomohiro NISHIKAWA, Tomoyuki MAEDA, Yasuhiro HOSHIYAMA and Shigeyuki TAKANAGA

Okayama Ceramics Research Foundation, 1406-18 Nishikatakami, Bizen, Okayama, 705-0021, Japan

Abstract : Al-Zr-C system compounds were synthesized by using three types of carbons : ligneous carbon, carbon black and flake graphite. Mineral compositions of Al-Zr-C system compounds from ligneous carbon and carbon black were $Zr_2Al_3C_5$ and $Zr_3Al_3C_5$. Heating treatment of as-synthesized compounds from room temperature to 1300°C with a constant temperature-programmed rate in O_2/Ar led to formations of zirconia and alumina. Analyses of exhaust gases during the oxidation process of the compounds revealed remaining of a carbon component in carbides until 1100°C.

Key words : Al-Zr-C system, ligneous carbon, carbon black, flake graphite, oxidation

要 旨 : 3種類の炭素源をもちいたAl-Zr-C系化合物の合成について検討した。木質炭素およびカーボンブラックから合成されたAl-Zr-C系化合物の組成は $Zr_2Al_3C_5$ および $Zr_3Al_3C_5$ であった。合成されたAl-Zr-C系化合物をアルゴン/酸素混合雰囲気、一定昇温速度で室温から1300°Cまで加熱すると、ジルコニアおよびアルミナへ変化した。酸化過程の排ガス解析によってAl-Zr-C系化合物は炭素成分を1100°Cまで保持することがわかった。

1 はじめに

炭素含有耐火物に添加されてきた物質はアルミニウム、シリコンあるいはマグネシウムなどの単体やそれらの合金である¹⁾。また、炭化ホウ素などの炭化物も含まれる。このような添加剤は、酸化防止効果だけでなく、緻密化や熱間強度の増加あるいは表面保護層の形成など耐火物の使用中に起こることが期待される^{2,3)}。一方、2種類の金属をふくむ炭化物(複合炭化物)を添加剤として機能するとき、その酸化反応が逐次的に起こる形態が示されており、複合炭化物は新たな添加剤として提案されている⁴⁾。使用中に添加剤自身が変質あるいは耐火物基材との反応によって、耐火物の組織に必要とする機能性の補填あるいは増強することは、耐火物の付加性能を高めるキーポイントと考える。近年ではアルミニウムとシリコンの炭化物のひとつである Al_4SiC_4 は、添加剤としてもっとも研究例⁵⁻⁸⁾が多い化合物であり、使用中において耐火物組織の緻密化が報告されている⁹⁾。

耐火物の構成要素に応用可能な元素は限られており、炭素含有化合物に使用可能な元素はさらに絞られる。そのような元素の炭化物は、上述した諸特性に有効な添加剤としての可能性が見込める。しかしながら、炭化物の合成例が少ないことや、それを耐火物へ応用することによって生じる挙動の多くは調べられていない。したがって、基本的な

知見も少ないのが現状である。

新たな添加剤を模索するために、アルミニウムとジルコニウムの複合炭化物に注目した。この炭化物は自身の酸化後もアルミナあるいはジルコニアへ変質するため、高温での使用環境に耐えることができる。また化合物の結晶構造中のAl-CおよびZr-C結合は高いエネルギーをもち機械的な強さが期待される構造材料として望ましい。Al-Zr-C系の化合物はこれまで $AlZrC_2$ あるいは $Zr_2Al_3C_5$ の合成が報告されている¹⁰⁻¹²⁾。本報ではアルミニウム、ジルコニウムの各単体をもちい、炭素源に廃木材の樹皮を1000°Cで炭化処理した樹皮(以下、木質炭素と表記する)、カーボンブラックおよび鱗状黒鉛からAl-Zr-C系化合物の合成を試みた。木質炭素がもつ炭化物の合成に対する有用性は、第72回原料専門委員会にて Al_4SiC_4 を例として報告した¹³⁾。Al-Zr-C系化合物の合成に対しても木質炭素の適用性が十分にあり得る。また、このようなAl-Zr-C系化合物の酸化挙動を調査した報告はなく、本研究はそのはじめての例である。

2 実験方法

金属アルミニウム(99.3%, -75μm, 東洋アルミニウム)をそのまま使用した。金属ジルコニウム(98%, 和光純薬)

平成25年11月20日受付, 平成26年3月20日受理
投稿責任者: 西川智洋

Table 1 Molar ratio and mass percent of ingredients for a synthesis of Al-Zr-C compounds.

Ingredients	Molar ratio / mol	Mass / %
Aluminum	1.00	18.97
Zirconium	1.00	64.14
Carbon	2.00	16.89

は保存に使用された水を除去して、40℃で3時間真空乾燥させて使用した。炭素源には木質炭素(炭素含有量約88%)に加えて、カーボンブラック(99%以上、算術平均粒子径25nm、東海カーボン)、鱗状黒鉛(98%、-75μm、丸豊鑄材)の3種類を選択した。

Al-Zr-C系化合物として、Leela-AdisornらがAlZrC₂およびZr₂Al₃C₅の合成を報告している¹⁰⁻¹²⁾。各出発原料の単体をもちいた報告がなく、各原料の混合比は表1に示すようにAl:Zr:Cの比が1:1:2のモル比とした。各原料を秤量したあと乳鉢で混合した。混合物を黒鉛るつぽに装填してアルゴン雰囲気下、1700℃(昇温速度:10℃・min⁻¹)で5時間加熱した。炉を自然冷却して合成粉体を得た。合成粉体のX線回折(RINT2200, Rigaku Corp.)パターンを2θ=10-70°の範囲、スキャンスピード2°・min⁻¹で測定して鉱物組成を同定した。合成粒子を試料台に載せた粘着カーボンシート上に固定し、加速電圧15kVの電界放出型走査電子顕微鏡(JSM-6340F, JEOL, Ltd.)で形態を観察した。合成粒子の真密度はピクノメーター(Multi pycnometer, Quantachrome Corp.)でヘリウムガス置換により測定した。

合成粉体の酸化挙動を10℃・min⁻¹の昇温速度で200ml・min⁻¹の空気雰囲気あるいは656ml・min⁻¹のアルゴン/酸素混合雰囲気下の熱重量示差熱計(EXSTAR TG/DTA6000, Seiko Instruments Inc.)をもちいて記録した。熱重量示差熱分析の際、発生したガス種を四重極型質量分析計(REGA, ULVAC Inc.)で分析した。合成粉体をアルミナるつぽに入れて700℃、900℃、1000℃、1100℃、1300℃の各温度まで10℃・min⁻¹で加熱し、所定温度に到達後、ただちに液体窒素温度の鉄製るつぽに投入して急冷させた。急冷した各粉体のX線回折パターンを同上条件で測定した。

3 結果および考察

3・1 Al-Zr-C系化合物の合成におよぼす炭素源の影響

図1 (a), (b), (c) に各種炭素源をもちいて合成したAl-Zr-C系化合物のX線回折パターンをそれぞれ示す。(a), (b) からわかるように回折ピークはZr₃Al₃C₅およびZr₂Al₃C₅に帰属され、これらの複合炭化物が合成された。各パターンの2θ=32.3°に現れたZr₃Al₃C₅の最強線と2θ=33.5°に現れたZr₂Al₃C₅のそれを比較すると、前者の強度が

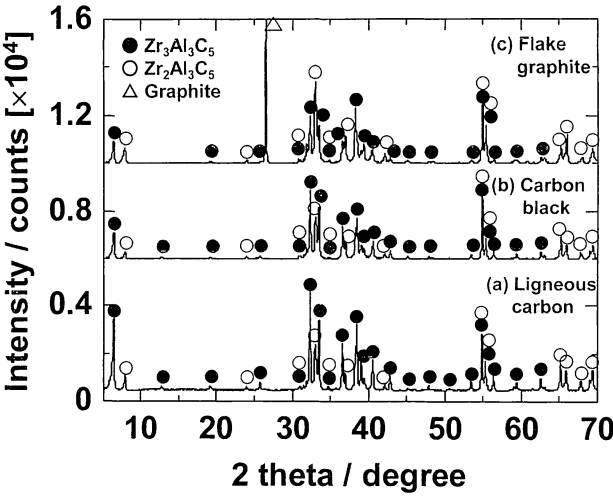


Fig. 1 X-ray diffraction patterns of Al-Zr-C system compounds from various carbons; (a) ligneous carbon, (b) carbon black and (c) flake graphite.

高かった。炭素源が木質炭素およびカーボンブラックにかかわらず、主相はZr₃Al₃C₅であった。木質炭素をもちいて合成は2回実施し、同様の再現性を確かめた。合成される2種類の複合炭化物を厳密に作り分けることは原料の配合比率の最適化によって可能である。

(c) に示すように鱗状黒鉛をもちいると2種類の複合炭化物のピークとともに、2θ=26.5°に黒鉛のピークが鋭く現れた。使用した炭素源を比較すると、鱗状黒鉛が合成後に残留し、その一方で木質炭素やカーボンブラックは仕込んだ原料がすべて合成反応に消費されたと考えられる。鱗状黒鉛が炭素源の場合、合成反応が完結しにくいことが予想される。非晶質炭素である木質炭素やカーボンブラックは反応性が高く、鱗状黒鉛は反応性が低いことが要因であろう。しかしながら、鱗状黒鉛を炭素源としても残留成分にアルミニウムやジルコニウムあるいはそれらの合金は認められなかった。この点について現在十分に説明できない。電子線回折法などから残留した黒鉛粒子の配向などさらに踏み込んだ考察を検討中である。

合成したAl-Zr-C系化合物粒子の表面形態を電界放出型走査電子顕微鏡で観察した。その像を図2にまとめて示す。SEM像からわかるように、木質炭素から合成されたAl-Zr-C系化合物は10μm程度の凝集体であった。一次粒子は直径2-3μm、厚さ500nm程度の板状である。カーボンブラックをもちいると粒子の各形状は木質炭素のときよりも約半分の大きさであった。とくに粒子は非常に小さい薄片状に合成された。Al₄SiC₄の合成¹³⁾でも報告したように、非晶質炭素の使用によって合成粒子の板状化が本報においても認められた。木質炭素およびカーボンブラックから合成したAl-Zr-C系粒子の真密度はそれぞれ4.69g・cm⁻³,

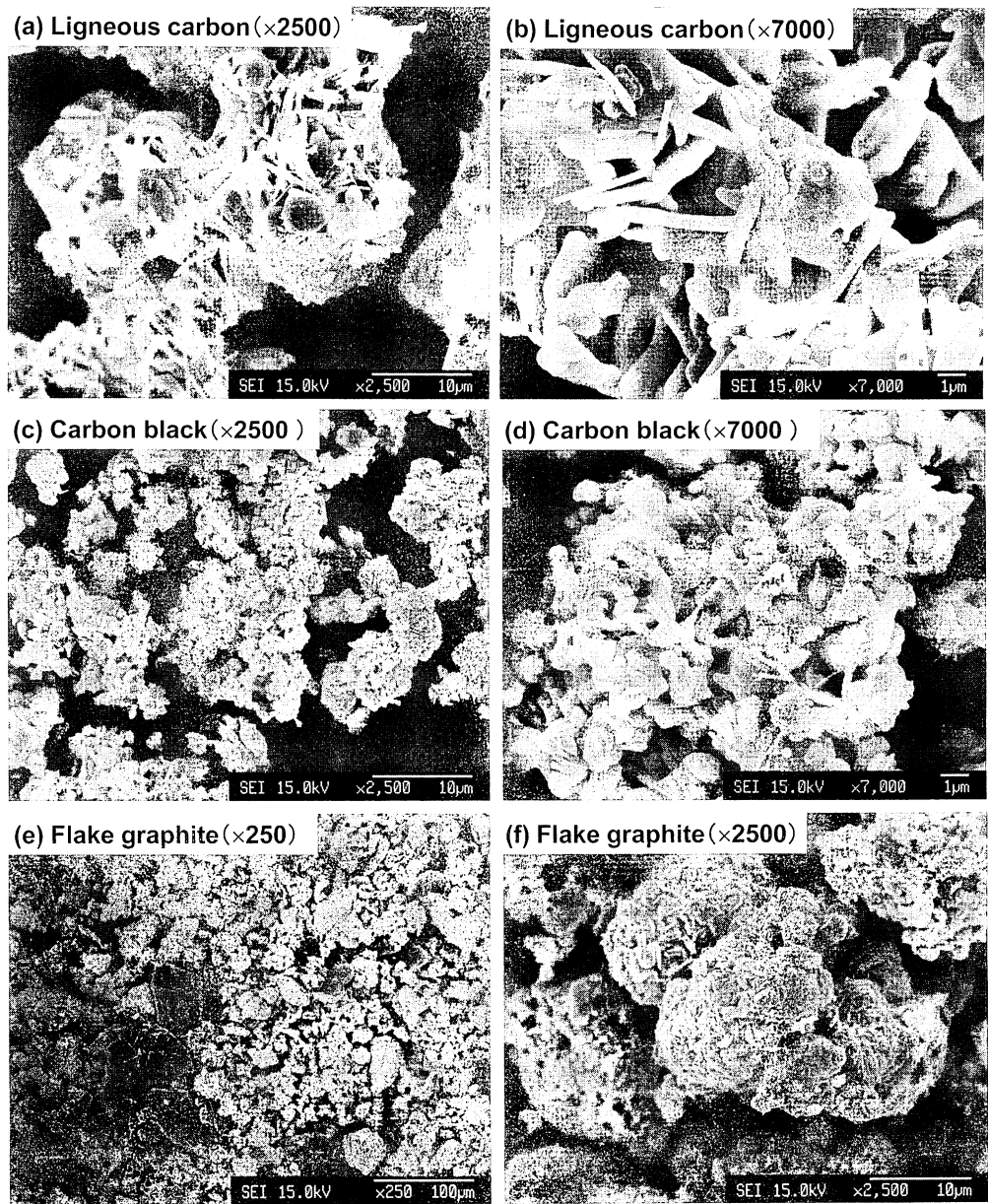


Fig. 2 Scanning electron microscope images of Al-Zr-C system particles synthesized by using ligneous carbon, carbon black and flake graphite.

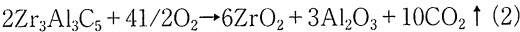
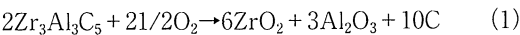
4.48g・cm⁻³であり、木質炭素をもちいることによって合成されるAl-Zr-C系化合物の板状化を促進させ、結晶構造を発達させたと思われる。一方で、鱗状黒鉛をもちいるとSEM像において残留した黒鉛がはっきりと観察され、X線回折の結果が裏付けられた。

3・2 Al-Zr-C系化合物の酸化挙動

合成したAl-Zr-C系粒子の熱重量示差熱分析（TG-DTA）の結果を図3に示す。(a)の合成粒子は炭素源に木質炭素、(b)の合成粒子は炭素源にカーボンブラックを選択したものである。鱗状黒鉛から合成した粒子は炭素を残留するためTG-DTAの比較対象から除外した。図3において各過程をi→vで追跡した曲線は熱重量（TG）、I→Vで追跡した

曲線は示差熱（DTA）曲線を表す。

図3（a, b）のTG曲線に注目すると、重量が増加しはじめる点iの（酸化開始）温度は400℃近傍であった。カーボンブラックのそれは300℃近傍であった。点iiは酸化加速温度であり、木質炭素で550℃付近、カーボンブラックで500℃付近であった。極大点iiiにおける重量増加率は木質炭素で36.6％、カーボンブラックで35.9％であった。TG曲線の極大点は理論値を10％上回った。



酸化反応過程においてZr₃Al₃C₅の全炭素が消失しない場合、式（1）が仮定される。この反応式にしたがって酸化

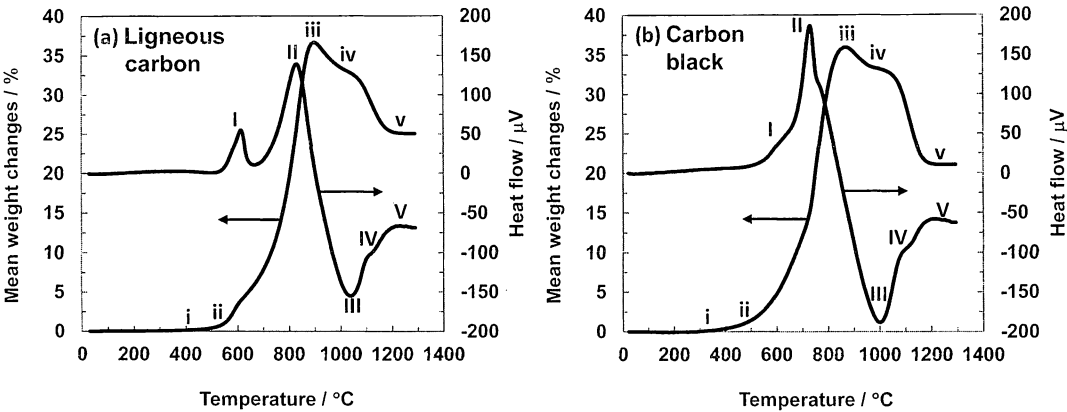


Fig. 3 Thermo gravimetric and differential thermal analyses of Al-Zr-C system particles synthesized by using (a) ligneous carbon and (b) carbon black.

が進行すれば、重量増加率は40%と計算される。TG曲線の極大点である35-36%はこれに近い。炭素成分は炭素の残留のほかに、酸炭化物あるいはオキシ炭酸塩などの前駆体となる非晶質化合物の形成によって保持されていると予測している。TG曲線はiiiからv（900～1300℃）の範囲において10～15%の重量減少を示した。点vにおける重量増加率は木質炭素から合成した粒子が25%、カーボンブラックから合成した粒子が21%で一定となった。 $Zr_3Al_3C_5$ の完全酸化を理論的に考えると、増加する重量は式（2）から約26%と見積もられる。1300℃に達して式（2）から見積もられる理論的な重量増加率に対応したことがわかった。

前述した同過程のDTA曲線を見ると、Iを經由してIIまで発熱反応による大きなピークが出現した。したがって、この過程では酸化反応が進行している。II→IIIのDTA曲線は急峻な下降を示した。この要因は900℃までに発熱ピークが終息したことと、900℃以上で吸熱ピークの出現したことが組み合わさったためと考えられる。吸熱ピークの要因は残存する炭素成分をもつ化合物の相転移によるものと推測している。III→Vは発熱ピークが出現した。この現象は保持された炭素成分の酸化消失によって引き起こされたことが予測される。前述したように、重量減少分に相当する炭素成分を保持している可能性が高く、酸化反応によって炭化物から酸化物へ変化する過程で相変化を起こしていると思われる。

つぎに、木質炭素から合成した粒子を空气中で加熱し、以下の各温度（700℃、900℃、1000℃、1100℃、1300℃）で急冷することによって酸化反応過程の結晶相を確かめた。酸化前および加熱急冷後の各粒子のX線回折パターンを図4に示した。（a）は図1（a）に示した合成粉体のパターンを再掲した。図4（b）に示す700℃では主相がAl-

Zr-C系化合物であるが、わずかに ZrO_2 の生成が認められた。図4（c）に示す900℃でAl-Zr-C系化合物のピークは消失し、 ZrO_2 の生成が顕在した。 ZrO_2 のピークはいずれもブロードで結晶性の低い状態であることが示唆される。900℃は ZrO_2 が単斜晶から正方晶へ転移する温度であり、単斜晶と正方晶の2つのピークが出現した。図4（d, e）に示す1000℃および1100℃で新たに出現したピークはなく、正方晶 ZrO_2 のピーク強度のみが増加した。残存する炭素成分による酸炭化物あるいはオキシ炭酸塩などの酸化過程の中間体の結晶相を、酸化過程で急冷することによって明らかにできることを期待したが、酸化過程で形成された結晶相は ZrO_2 のみであった。図4（f）の1300℃では各ピークが鋭くなり、 ZrO_2 の結晶性が高くなったことがわかる。1300℃で単斜晶 ZrO_2 のピーク強度が増加する特異な現象が起きた。通常1300℃では正方晶あるいは立方晶へ転移することが一般的に知られている¹⁴⁾。この挙動はそれに対応せず、本研究の炭化物を酸化して生成させた ZrO_2 は高温でも単斜晶系を保持する可能性を示した。一方、アルミニウム成分の酸化物は図4（f）に示すように $\theta-Al_2O_3$ であった。 $\theta-Al_2O_3$ から $\alpha-Al_2O_3$ への転移温度は約1200℃であることが知られており^{15,16)}、1300℃の急冷処理によって Al_2O_3 の生成が認められた。式（2）示したAl-Zr-C系化合物の完全酸化反応は1300℃においてほぼ終了したことが考えられる。これは図3（a）のTG曲線が1200℃から1300℃までの温度域でほぼ平坦になったことから支持できる。

つぎに、熱重量分析の過程で発生したガスを質量分析計で測定したTG-MASSを図5に示す。測定はキャリアガス（アルゴン）に酸素を4：1で混合した雰囲気ガスを使用した。質量分析によって発生したガスは CO_2 とCOのみであった。図5（b）に示すようにCOも CO_2 の発生と同じ温度

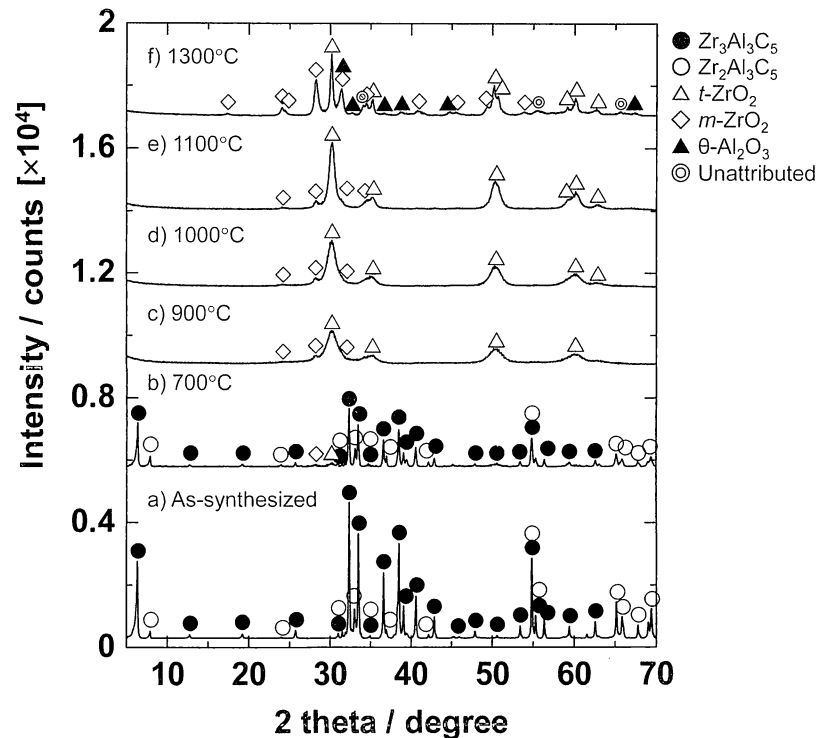


Fig. 4 X-ray diffraction patterns of (a) as-synthesized Al-Zr-C system particles by using ligneous carbon, and quenched particles at (b) 700°C, (c) 900°C, (d) 1000°C, (e) 1100°C and (f) 1300°C in air.

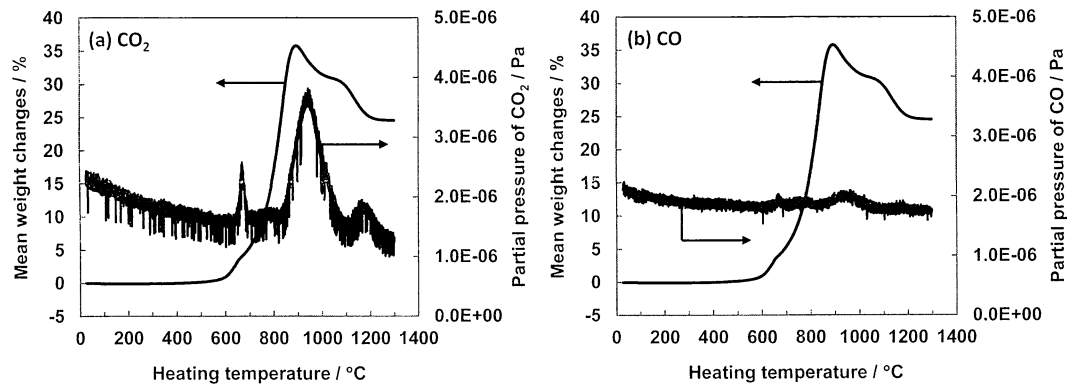


Fig. 5 Thermo gravimetric and combustion gas analyses of (a) CO₂ and (b) CO from Al-Zr-C system particles synthesized by using ligneous carbon.

域においてわずかに検出された。COの発生はサンプル量あるいは雰囲気の影響を受けた不完全な酸化と推察し、CO₂に注目して考察を行った。図5 (a) に示すように、CO₂分圧曲線のピークがTG曲線の増加に対応する600～700℃、800～1100℃、1100～1300℃の各温度域に現れた。600～700℃のピークはAl-Zr-C系化合物粒子の部分酸化によって現れたと考えられる。これは図4 (b) からわかるようにZrO₂の生成が認められたことから裏付けられる。800～1100℃に現れたピーク面積は、600～700℃のそれよりも3.6倍大きく、発生したCO₂は合成した化合物の酸化燃

焼で発生するよりも多く排出されたと推察する。800～1100℃のTG曲線は、800～900℃の範囲で重量増加、その後900～1100℃の範囲で重量減少となり、2つの過程が含まれる。前者の温度域で発生したCO₂はAl-Zr-C系化合物の燃焼に由来し、後者の温度域で発生したCO₂は試料中に残留した炭素成分の燃焼に起因すると思われる。さらに、1100～1300℃の範囲で検出されたCO₂も残留炭素成分の燃焼によって発生し、同じ温度域におけるTG曲線を減少させたと考えられる。図3 (a) に示す900～1300℃におけるDTA曲線の発熱過程は残留炭素の燃焼を示唆するも

のであり、同温度域において炭素成分が残存する考察を支持することができる。

4 まとめ

新たな複合炭化物原料となるAl-Zr-C系粒子の合成を試みた。この合成に対する出発原料のうちのひとつである炭素源について評価した。本研究で得られた結果をつぎにまとめた。

- (1) Al-Zr-C系化合物の合成に使用する炭素源は、炭化した樹皮（木質炭素）のほかカーボンブラックの使用が可能である。
- (2) 本研究で合成されたAl-Zr-C系化合物の鉱物組成は $\text{Zr}_3\text{Al}_3\text{C}_5$ および $\text{Zr}_2\text{Al}_3\text{C}_5$ である。
- (3) 炭素源に鱗状黒鉛を使用すると、鱗状黒鉛とAl-Zr-C系化合物のコンポジット粉体が得られる。
- (4) 木質炭素から合成されたAl-Zr-C系化合物の酸化は、 $10^\circ\text{C} \cdot \text{min}^{-1}$ の条件において 500°C 近傍で酸化が開始される。また、 1300°C まで炭素成分を保持したまま酸化が進行する。
- (5) Al-Zr-C系化合物の酸化によって生成する ZrO_2 は 1300°C で正方晶と単斜晶が共存する。
- (6) Al-Zr-C系化合物の酸化によって生成する Al_2O_3 は 1300°C で θ 相となる。

文献

- 1) A. Yamaguchi : J. Tech. Assoc. Refract. Jpn., 30, 282-286 (2010).
- 2) 山口明良 : “炭素含有耐火物—原料から用途・課題まで—”, 岡山セラミックス技術振興財団, pp. 62, (2006).
- 3) Y. Hoshiyama and A. Yamaguchi : Proceedings of Unified International Technical Conference on Refractories 2011, 2-B2-17 (2011).
- 4) Shaowei Zhang and A. Yamaguchi : J. Ceram. Soc. Jpn., 103, 235-239, (1995).
- 5) K. Inoue, A. Yamaguchi and S. Hashimoto : J. Ceram. Soc. Jpn., 110, 1010-1015, (2002).
- 6) K. Inoue, S. Mori, and A. Yamaguchi : J. Ceram. Soc. Jpn., 111, 126-132, (2003).
- 7) Jin-Seok Lee, Sea-Hoon Lee, T. Nishimura and H. Tanaka : J. Ceram. Soc. Jpn., 116, 717-721, (2008).
- 8) O. Yamamoto, M. Ohtani and T. Sasamoto : J. Mater. Res., 17, 774-778, (2002).
- 9) 星山泰宏 : セラミックス岡山, 21-2, 2-3, (2013).
- 10) U. Leela-Adisorn, S.-M. Choi, N. Tera, T. Takeuchi, S. Hashimoto, S. Honda, H. Awaji, K. Hayakawa and A. Yamaguchi : J. Ceram. Soc. Jpn., 113, 188-190, (2005).
- 11) U. Leela-Adisorn and A. Yamaguchi : Key Engineering Materials, 280-283, 1379-1384, (2005).
- 12) U. Leela-Adisorn, S.-M. Choi, N. Tera, T. Takeuchi, S. Hashimoto, S. Honda, H. Awaji, K. Hayakawa and A. Yamaguchi : Key Engineering Materials, 317-318, 27-30, (2006).
- 13) 西川智洋, 前田朋之, 星山泰宏, 山口明良 : 第72回原料専門委員会報告集, 耐火物技術協会, pp. 75-81, (2012).
- 14) 日本セラミックス協会編, “セラミック工学ハンドブック第2版”, p. 1148 (2002).
- 15) 日本セラミックス協会編, “セラミック工学ハンドブック第2版”, p. 81 (2002).
- 16) 山田興一 : 軽金属学会, 31, 583-589, (1982).

$\text{Al}_2\text{O}_3\text{-Al}_4\text{SiC}_4\text{-C}$ 材質の高温における緻密化

星山泰宏, 高長茂幸

一般財団法人 岡山セラミックス技術振興財団 〒705-0021 岡山県備前市西片上1406-18

Densification of $\text{Al}_2\text{O}_3\text{-Al}_4\text{SiC}_4\text{-C}$ Brick at High Temperature

Yasuhiro HOSHIYAMA, Shigeyuki TAKANAGA

Okayama Ceramics Research Foundation, 1406-18, Nishikutakami, Bizen, Okayama 705-0021

キーワード: Al_4SiC_4 , $\text{Al}_2\text{O}_3\text{-C}$, 緻密化

1 緒言

Al-Si-C 系には Al_4SiC_4 , $\text{Al}_4\text{Si}_2\text{C}_5$, $\text{Al}_4\text{Si}_4\text{C}_7$, $\text{Al}_4\text{Si}_3\text{C}_6$, Al_8SiC_7 の組成を有する化合物が存在するが, その中でも Al_4SiC_4 は広い温度域で安定であり, 融点も 2037°C と比較的高く, 耐水和性にも優れるなど, 耐火物原料として有望と考えられている^{1,2)}。これまでの検討によって, MgO-C 質あるいは $\text{Al}_2\text{O}_3\text{-C}$ 質耐火物に Al_4SiC_4 を添加すると, 図1,

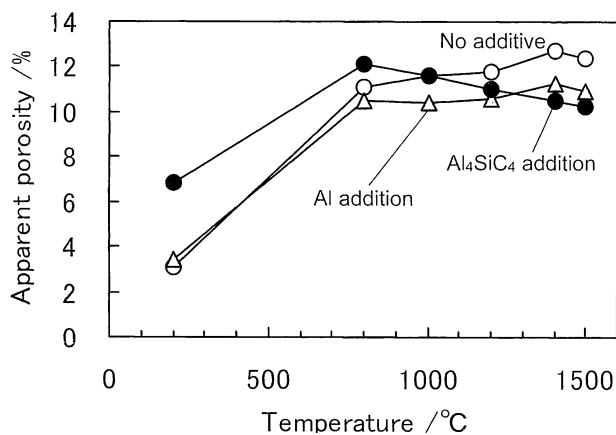


Fig. 1 Densification effect of Al_4SiC_4 added to MgO-C brick³⁾.

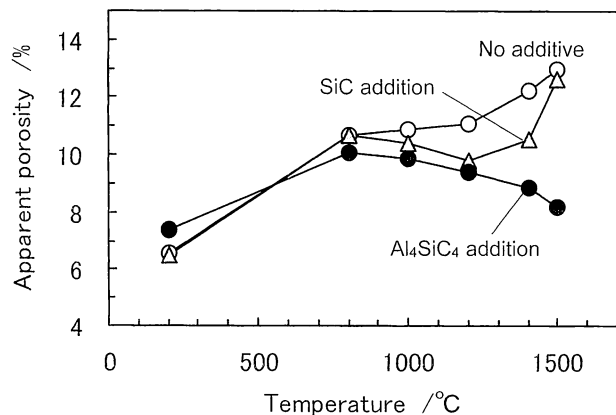
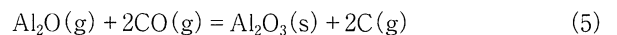
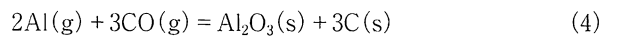
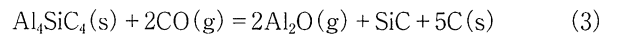
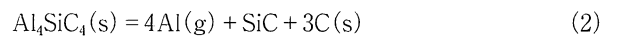
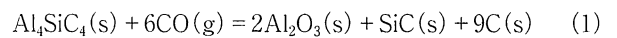


Fig. 2 Densification effect of Al_4SiC_4 added to $\text{Al}_2\text{O}_3\text{-C}$ brick⁴⁾.

図2に示すように高温下で気孔率が低下し, その緻密化効果は金属AlやSiCを添加した場合よりも大きくなる^{3,4)}。これらの緻密化効果は, 高温下で Al_4SiC_4 からAlを含むガスが発生して耐火物組織中の空隙に拡散し, CO ガスと反応して再び Al_2O_3 と炭素として凝縮する蒸発凝縮反応によってもたらされると推定され, 図3に示すような反応機構モデルを提唱している⁵⁾。その全反応式は(1)式で表され, その素反応に相当する蒸発および凝縮の反応式は(2)~(5)式で与えられる⁵⁾。



本研究では, この Al_4SiC_4 の緻密化効果をより積極的に利用することを考え, $\text{Al}_2\text{O}_3\text{-C}$ 質耐火物に Al_4SiC_4 粉末を多量に配合することによって, 高温下で気孔の少ない緻密な

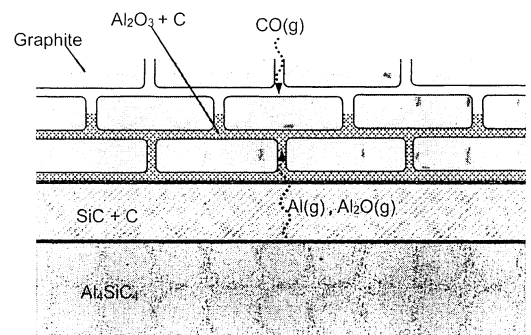


Fig. 3 Schematic model of reaction mechanism of Al_4SiC_4 in carbon containing refractory at high temperature⁵⁾.

平成26年3月18日受付, 平成26年4月14日受理
投稿責任者: 星山泰宏

耐火物組織を形成させる手法について検討を行った。

2 実験方法

Al₄SiC₄粉末は、金属Al粉末（-200M）、Si粉末（-325M）、鱗状黒鉛（-100M, 99%）を原料として作製した。理論組成に配合したものをボールミルで10h乾式混合し、得られた粉末を黒鉛るつぼ中、Ar雰囲気下で1700℃-5hの焼成を行う方法で合成した。焼成後の粉末を再びボールミルで10h乾式粉碎して20μm以下（平均約8μm）の粒度とし、供試原料とした。粉末X線回折で確認した合成粉末の結晶相はほぼAl₄SiC₄の単相で、ごくわずかに黒鉛を随伴していた。

表1に作成したAl₂O₃-Al₄SiC₄-C試料の構成内容を示す。比較用として炭化物無添加のものと、Al₂O₃微粉の全量25%をAl₄SiC₄粉末に置換して配合したものを作製した。試料は、表1の配合物を混合、混練の後に、150MPaの一軸加圧によって25×25×120mm形状に成形し、200℃-10hの熱処理を行って作製した。作製した試料の一般物性を表1に示してあるが、Al₄SiC₄配合試料は微粉の平均粒度が小さいため成形時の充填度が低くなり気孔率が4%程度高くなっている。

作製した試料を、炭素含有耐火物の実炉使用時の雰囲気

を想定して炭素粉末中で焼成した。焼成は、図4に示すように黒鉛粉末に埋設した状態で行い、昇温速度を10℃/minとし、所定の温度で保持した後に炉内で放冷する条件で実施した。焼成温度は800～1500℃とし、実炉で長期間使用した場合の反応を推測するために、保持時間を最大20時間まで延長する焼成を行った。焼成前後の重量変化率を測定し、焼成後試料の見掛け気孔率、かさ密度をアルキメデス法で測定した。また焼成後試料の切断面をエポキシ樹脂に埋設して硬化させた後に鏡面研磨し、光学顕微鏡を用いて微構造の観察を行った。

3 結果および考察

図5に、Al₂O₃-C試料を2時間還元焼成したときの重量変化を示す。図は200℃熱処理後を基準とした場合の重量変化率を表示している。炭化物無添加の試料で見られる800℃での重量減少は、バインダーとして使用したフェノール樹脂の熱分解によるものである。Al₄SiC₄多量配合試料ではこの800℃での重量減少が少なくなっており、何らかの原因で重量減少が抑制されている。その後温度の上昇とともに無添加試料では重量が漸減しているが、Al₄SiC₄配合試料では1200℃を超える温度域で顕著な重量増加が見られる。

炭素含有耐火物に添加されたAl₄SiC₄の高温反応は、これまでの研究においても1200℃を超える温度域で認められており、その第一段階の全反応式は、91.3%の重量増加を伴う(1)式で与えられる³⁻⁵⁾。図5に見られる高温域の顕著な重量増加も同様の反応が試料内で進行しているものと推測される。

図6、図7に、2時間焼成後の見掛け気孔率、かさ密度を示す。無添加試料、Al₄SiC₄配合試料ともに、バインダーとして使用したフェノール樹脂の熱分解によって800℃で気孔率が増大している。無添加試料は温度の上昇と共に気孔率が増大し、かさ密度も減少している。一方、Al₄SiC₄

Table 1 Composition and properties of Al₂O₃-C brick samples

No.		1	2
Composition /mass%	Fused alumina -1mm	60	60
	-75μm	25	-
	Flake graphite -150μm	15	15
	Al ₄ SiC ₄ -20μm	-	25
	Phenol resin	ex.4	ex.4
Property	Hexamethylenetetramine	ex.0.4	ex.0.4
	Apparent porosity /%	10.4	14.3
	Bulk density /g·cm ⁻³	3.04	2.72

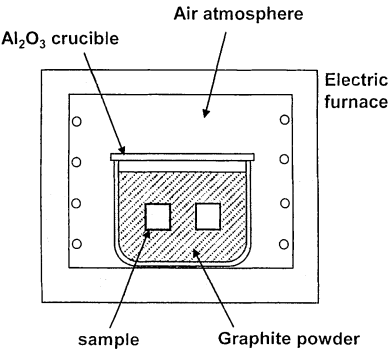


Fig. 4 Schematic diagram of heating test in reducing atmosphere.

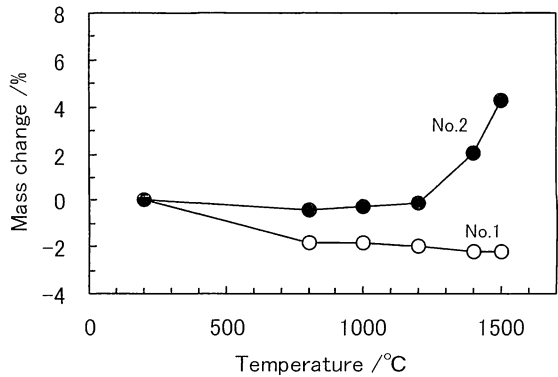


Fig. 5 Mass change of the brick samples during heating in the reducing atmosphere for 2 hours.

配合試料は焼成温度が1200℃以上になると気孔率が著しく低下しており、それに対応してかさ密度も増大している。図5に示したように、同じ温度域で明確な重量増加も観察されており、1200℃以上で Al_4SiC_4 の反応が進行して組織が緻密化されていることがわかる。1500℃では見掛け気孔率が9.7%にまで低下し、800℃よりも約8%低い値を示している。

次に、焼成時間を延長した時の見掛け気孔率の変化を図8に示す。焼成温度が1200℃になると、 Al_4SiC_4 配合試料の見掛け気孔率は時間とともに低下しており、緻密化反応が徐々に進行することがわかる。気孔率の減少は1500℃でより明確になり20h焼成後には3.7%に達している。また、1500℃での焼成時間が6時間以上になると気孔率減少の傾

きが小さくなっており、 Al_4SiC_4 の反応が進行しにくくなっていることが推測される。開口気孔の量を表す見掛け気孔率が5%程度にまで低下してくると、COガスの試料内部への侵入経路も少なくなるため、COガスの供給速度が低下して(1)式の反応が進行しにくくなることは十分考えられる。

図9、10に、1500℃で20時間焼成した後の、光学顕微鏡写真を示す。無添加試料ではアルミナと黒鉛の粒子間に空隙が多く見られる。一方 Al_4SiC_4 配合試料では、数 μm 以下の微小な粒子からなる反応生成物が、組織の空隙をくまなく充填している状況が観察される。これらの微小粒子群は、数 μm 以下の狭い隙間にまで密に充填されている。図3の蒸発凝縮反応(2)～(5)式によって、組織中の気孔

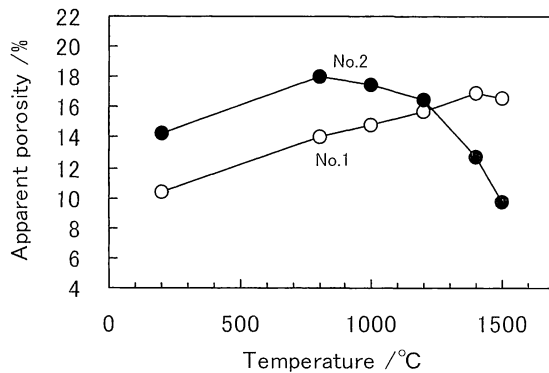


Fig. 6 Apparent porosity of the brick samples after heating in the reducing atmosphere for 2 hours.

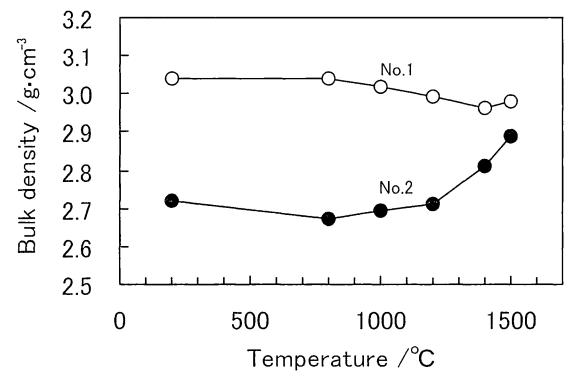


Fig. 7 Bulk density of the brick samples after heating in the reducing atmosphere for 2 hours.

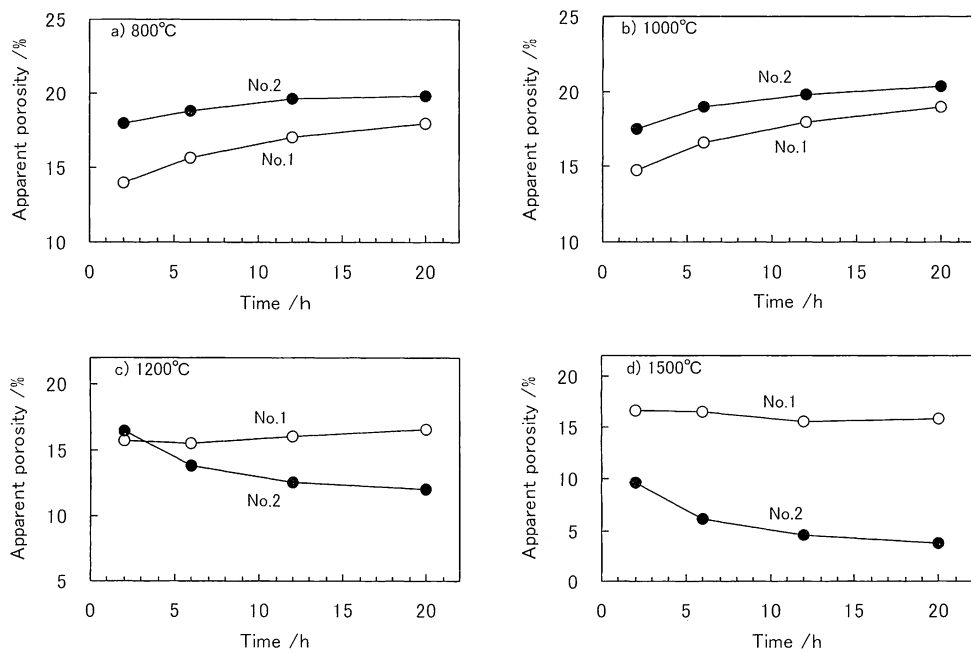


Fig. 8 Apparent porosity of the brick samples after heating in the reducing atmosphere as a function of holding time at several temperatures.

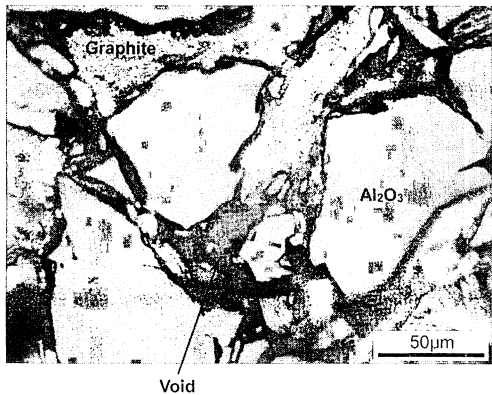


Fig. 9 Microscopic texture of No.1 sample after heating in the reducing atmosphere at 1500°C for 20 hours.

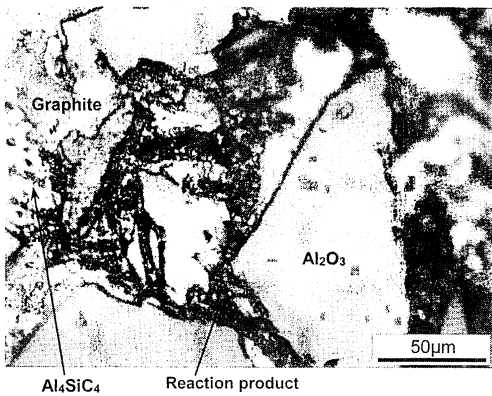


Fig. 10 Microscopic texture of No.2 sample after heating in the reducing atmosphere at 1500°C for 20 hours.

が効率よく充填，緻密化されている様子が認められる。

ここで，実炉で長期間使用した際に形成される組織について推定する。20時間焼成した後の見掛け気孔率を図11にまとめて示す。20時間の焼成ではまだAl₄SiC₄の反応が少しずつ進行している途中段階と思われるが，実炉での現象をおおよそ類推することが可能ではないかと考える。図を見るとAl₄SiC₄配合試料は1000℃から1500℃にかけて直線的に気孔率が低下しており，20%から4%へと気孔率が減少している。通常，炉のライニングに使用される耐火物の場合には，炉の内側（稼働面）から外側（背面）に向かって耐火物内部に温度勾配が生じている。すなわち，図11の横軸が耐火物の稼働面側，背面側に対応しており，高温の1500℃は稼働面に近い領域とみなすことができ，低温の1000℃前後は背面側に近い領域と考えることができる。このように考えると，Al₄SiC₄を多量に配合した炭素含有耐火物は，実炉で長期間使用される間に，高温の稼働面側近傍において非常に緻密な組織が形成されるという特徴を有することがわかる。また図11は，稼働面から背面にかけて

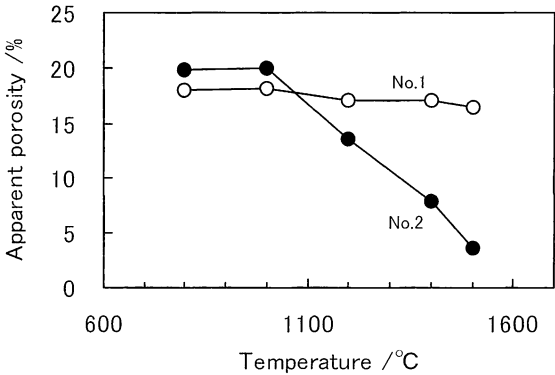


Fig. 11 Apparent porosity of the brick samples after heating in the reducing atmosphere for 20 hours.

気孔率が連続的に大きく変化する材料が形成されることを示しており，自らの内部反応によって傾斜材料が形づくられることも示している。実炉で使用することによって稼働面側が緻密化する自己形成型の緻密質耐火物であって，かつ背面にかけて気孔率が大きく異なる自己形成型の傾斜材料とも言え，これまでにないユニークな材質として位置付けることができる。

4 まとめ

Al₄SiC₄粉末を多量に配合したAl₂O₃-Al₄SiC₄-C質耐火物を作製し，高温下で緻密な耐火物組織を形成させる手法について検討を行った結果，以下のことが明らかとなった。

- (1) 1200℃以上でAl₄SiC₄の緻密化反応が進行して気孔率が低下し，かさ密度が増大した。その傾向は高温になるほど顕著であった。
- (2) 焼成時間とともに緻密化が進行し，1500℃-20h焼成後の見掛け気孔率は3.7%にまで減少した。
- (3) 緻密化が進行した組織では，数µm以下の微小な粒子からなる反応生成物が，組織の空隙をくまなく充填している。
- (4) 実炉を想定した場合，使用中に稼働面側で緻密な組織が形成され，背面側では気孔率の高い組織が形成されると推定される。自己形成型の緻密質耐火物かつ傾斜材料を得ることができる。

文献

1) S.Zhang, A.Yamaguchi: J. Ceram. Soc. Japan, 103 [3] 235-239 (1995).
2) J.Zhao, W.Lin, A.Yamaguchi, J.Ommyoji, J.Sun: J. Ceram. Soc. Japan, 115 [11] 761-766 (2007).
3) 星山泰宏，隠明寺準治，山口明良：耐火物，60 [10] 540-548 (2008).
4) 星山泰宏，隠明寺準治，山口明良：耐火物，61 [6] 290-294 (2009).
5) 星山泰宏，山口明良，隠明寺準治：耐火物，61 [10] 548-555 (2009).